MULTI-SCALE ANALYSIS OF THERMOHALINE STRUCTURES THROUGH

SEISMIC OCEANOGRAPHY, SOUTH ATLANTIC OCEAN

A Dissertation

by

JINGXUAN WEI

Submitted to the Graduate and Professional School of
Texas A&M University
in partial fulfillment of the requirements for the degree of

DOCTOR OF PHILOSOPHY

Chair of Committee,	David W. Sparks
Co-Chair of Committee,	Robert S. Reece
Committee Members,	Mark Everett
	Henry Potter
Head of Department,	Julie Newman

May 2022

Major Subject: Geophysics

ABSTRACT

The South Atlantic Ocean maintains the Atlantic meridional overturning circulation by transporting warm water equatorward and cold water poleward, its variability strongly influences the Earth climate system. Close monitoring of the South Atlantic variability is important in developing accurate circulation and climate models. This dissertation takes the advantage of a legacy multichannel seismic dataset that surveyed the South Atlantic interior along an important transect of the meridional overturning circulation, providing the first fine scale observation of the central South Atlantic that is challenging to study with conventional hydrographic measurements. The method, namely seismic oceanography, is capable of observing thermohaline structures on the order of several meters in both vertical and horizontal directions. Experiencing with this dataset, we develop a seismic processing strategy that enhances the imaging quality of the water column for legacy seismic data. Furthermore, we image the central South Atlantic down to ~1600 m and find numerous mesoscale structures formed by double diffusion and thermohaline intrusion. From the seismic images, we derive a high-resolution map of turbulent diffusivity of the central South Atlantic thermocline and find enhanced mixing caused by rough topography and a storm. We also find the important role of an eddy in promoting shear instabilities and deep propagation of near-inertial energy. Our findings suggest the prevalence of mesoscale processes and heterogeneity of turbulent mixing in the South Atlantic interior, calling for more fine scale observations in the ocean interior in order to build more accurate circulation and climate models.

ACKNOWLEDGEMENTS

I would like to thank my advisor Dr. Bobby Reece, for the opportunity to explore the exciting field of seismic oceanography, and for his guidance and support throughout the course of this research. I have learnt greatly from him, especially on the proposing, understanding and addressing of scientific questions. Bobby created a great environment of research freedom in our group, and provided me with abundant resources to ensure the continuity and productivity of my research. His kindness, optimism, encouragement, and sense of humor had made my Ph.D. life truly memorable.

This dissertation would not have been possible without the supports and instructions from Dr. Kathryn Gunn and Dr. Will Fortin. I learnt from Kathy the methods of deriving diffusivities from hydrographic data, as well as estimating current movement speeds from seismic data. She also provided invaluable insights about the results and discussions from oceanographic perspectives. Her generosity in sharing knowledge and enthusiasm in science have motivated me greatly. I am very grateful to Dr. Will Fortin who kindly provided the code of extracting diffusivities from seismic data. I have learnt many programming skills from his code, which facilitated my other programming tasks throughout the research.

Thanks also to the remainder of my committee for the invaluable help and discussion.

Thanks to all my friends, colleagues and fellow students in the Department of Geology & Geophysics and at Texas A&M as a whole. Special thanks to my great

officemates and dear friends Justin Estep and Kittipong Somchat for being so supportive and making my time at College Station so much fun.

Finally, thanks to my parents for their encouragement, support and love.

CONTRIBUTORS AND FUNDING SOURCES

Contributors

This work was supervised by a dissertation committee consisting of Professor Dr. Bobby Reece (advisor), Dr. David Sparks, and Dr. Mark Everett of the Department of Geology & Geophysics and Professor Dr. Henry Potter of the Department of Oceanography.

The results and discussions in Chapter 3 were aided by Dr. Kathryn Gunn at Centre for Southern Hemisphere Oceans Research.

Funding Sources

TABLE OF CONTENTS

LIST OF FIGURES

1. INTRODUCTION

The South Atlantic Ocean maintains the connection between the North Atlantic, the Pacific and the Indian Ocean by transporting warm water equatorward and cold water poleward, and is a critical component of the meridional overturning circulation that significantly influences the Earth's climate system (Garzoli et al., 2013). Understanding the distribution of water masses and their interactions within the South Atlantic is important for accurate circulation and climate models. However, the South Atlantic is one of the least observed basins in the world (Garzoli and Matano, 2011). Our current understanding of the South Atlantic is limited to low-frequency variability over large scale circulation and mesoscale variability confined to the western and eastern boundaries (Garzoli et al., 2015; Valla et al., 2018; Kersalé et al., 2019). Observations of mesoscale processes in the ocean interior are critically important as foundational input to climate models, which are very sensitive to even modest changes of mesoscale parameterizations (Fox-Kemper et al., 2019). In addition, accurate climate models require the knowledge of spatial distribution of turbulent mixing around the globe (Melet et al., 2013; Melet et al., 2016). However, the uncertainties of turbulent mixing parameterization are still large due to varying topographic conditions, tidal flows, and fast-changing wind forcing, all of which calls for extensive finer scale observations worldwide.

During the past several decades, repeating hydrographic surveys (Sloyan et al., 2019), the Argo ocean observing program (Roemmich et al., 2019), and numerous targeted observations have significantly enriched our understanding of the ocean. However, the

1

challenges in observing finer scale processes still persist. Conventional hydrographic measurements such as probes, floats and towed instruments typically produce high-resolution measurements in only one dimension and are ill-suited for mesoscale and turbulent mixing observations. There is a critical need for a measurement technique that can bridge the observational gaps between large and small scales. Seismic oceanography, emergent in the last two decades, has exhibited a capacity to observe a broad range of spatial and temporal scales by providing two-dimensional images of thermohaline fine structures at consistent horizontal and vertical resolution on the order of a few meters (Nandi et al., 2004), demonstrating its suitability in studying finer scales. Seismic oceanography uses the multichannel seismic profiling method that was originally designed for high-resolution imaging of solid earth subsurface structures (Sheriff and Geldart, 1995). Studies have shown the strength of seismic oceanography by mapping thermohaline fine structures and calculating spatial distributions of temperature, salinity, turbulent mixing and heat fluxes (Biescas et al., 2008; Fortin et al., 2016; Tang et al., 2016; Gunn et al., 2021).

My dissertation uses legacy multichannel seismic data to explore the mesoscale processes and turbulent mixing in the central South Atlantic from the Rio-Grande Rise to the Mid-Atlantic Ridge. The goal of this dissertation is as follows: (1) develop a seismic processing strategy that optimizes seismic imaging quality of legacy seismic data that was originally used for solid earth imaging; (2) provide the first long-distance, high-resolution observation of central South Atlantic thermohaline structures on finer scales, and compare the results with historical records for temporal implications; (3) study the spatial

distribution of turbulent mixing within the South Atlantic interior, extending observational record of basin-wide mixing patterns; (4) explore the drivers of turbulent mixing in the South Atlantic interior, offering new insights for mixing parameterization in the ocean interior.

2. SEISMIC IMAGING OF SOUTH ATLANTIC THERMOHALINE FINE STRUCTURES

2.1. Introduction

South Atlantic ocean circulation plays an important role in the Earth climate system due to its impact on the variability of Atlantic meridional overturning circulation (AMOC). Through the South Atlantic, the southward flow of the cold North Atlantic Deep Water (NADW) is compensated by the northward flow of warm, salty surface and central waters, along with cooler fresher Atlantic Intermediate Water (AAIW) (Broecker, 1991). The connection between the North Atlantic, the Pacific Ocean and the Indian Ocean is maintained by the South Atlantic, and a substantial amount of mass and heat are transported globally (Schmitz Jr, 1995). Observations and models consistently indicate that the South Atlantic influences significantly the water mass structure of the AMOC (Garzoli and Matano, 2011). Thus, it is crucial to monitor the variability of the South Atlantic; however, the South Atlantic is currently one of the least observed basins in the global ocean (Garzoli et al., 2013).

The Global Ocean Ship-Based Hydrographic Investigation Program (GO-SHIP) have carried out full water column hydrographic observations along several transects across the South Atlantic Basin approximately once a decade since the 1970s (Talley et al., 2016; Sloyan et al., 2019). These surveys provide knowledge on low-frequency variability over large scale circulation. However, it is also important to study mesoscale processes for they are essential for quantifying kinetic energy of ocean circulation

(Chelton et al., 2007). The oceanic mesoscale refers to flows with spatial scales of 1-100 km and time scales from days to months (Della Penna and Gaube, 2019). Existing research of mesoscale variability in the South Atlantic is mostly confined to studies of western and eastern boundary currents and more energetic zones like Brazil-Falkland confluence (Olson et al., 1988; Garzoli, 1993; Valla et al., 2018). Research on mesoscale processes in the South Atlantic interior is extremely rare, resulting in poor understanding of the existence, distribution, richness and influences of these processes. The large distance between existing hydrographic measurements and mooring instruments prevents adequately resolving mesoscale processes. Understanding mesoscale processes in the South Atlantic interior will contribute to answering key questions about circulation, diapycnal mixing and transport that affect our climate system.

In recent years, scientists discovered the ability of seismic waves to image oceanic thermohaline structures at unprecedented lateral resolution, namely seismic oceanography (SO), an ideal method to study mesoscale processes (Holbrook et al., 2003). The method utilizes the multichannel seismic (MCS) reflection technique similar to that used in petroleum industry for subsurface imaging. The data acquisition system is comprised of an air-gun array towed behind a vessel to generate acoustic energy, and a linear hydrophone array, or streamer (3-15 km long), to receive the acoustic energy that is transmitted and reflected at thermohaline boundaries in the water column. The final image is a vertical slice through the ocean, providing a high-resolution snapshot of thermohaline features at a specific time. The lateral resolution on the order of tens of meters is a nearly two order of magnitude improvement over conventional hydrographic measurements.

Nandi et al. (2004) demonstrated that the seismic method is able to capture temperature difference as small as 0.03 °C. Sallarès et al. (2009) presented that temperature predominantly affects seismic reflectivity by changing sound speed in the water. SO has contributed to our understanding of important oceanographic phenomena such as internal waves and turbulent mixing (Sheen et al., 2009), mesoscale eddies (Biescas et al., 2008), thermohaline staircases (Buffett et al., 2017), and investigating water dynamics through 3D imaging (Gunn et al., 2020). SO is likely to have a profound impact on our understanding of global oceanic processes from both spatial and temporal perspectives.

In January and February 2016, the Crustal Reflectivity Experiment Southern Transect (CREST) survey collected ~2700 km of 2D seismic data from the east end of the Rio-Grande Rise to the Mid-Atlantic Ridge at 30° S (Estep et al., 2019), providing an opportunity to investigate the mesoscale processes in the wind driven South Atlantic Subtropical Gyre at an important meridional transect (Figure 2.1). The primary goal of the CREST survey was to study the evolution of oceanic crust at 30° S. The reprocessing of this legacy MCS data to focus on the water column images, for the first time, the mesoscale structures in three major water masses in the South Atlantic: South Atlantic Central Water (SACW) that extends from the surface to approximately 730 m; cooler fresher Antarctic Intermediate Water (AAIW) that resides in the 730-1140 m depth range; and the Upper Circumpolar Deep Water (UCDW) from 1140-1560 m (Talley, 2011; Hernández-Guerra et al., 2019). Our primary objective is to image the unknown mesoscale processes in the South Atlantic interior and explore the possible mechanisms that drive them. Since legacy MCS acquisitions were not designed to image the water column, we also addressed

specific techniques in the processing of legacy seismic data for seismic oceanography, laying the foundation for additional use of legacy seismic data to study mesoscale structures in the ocean.
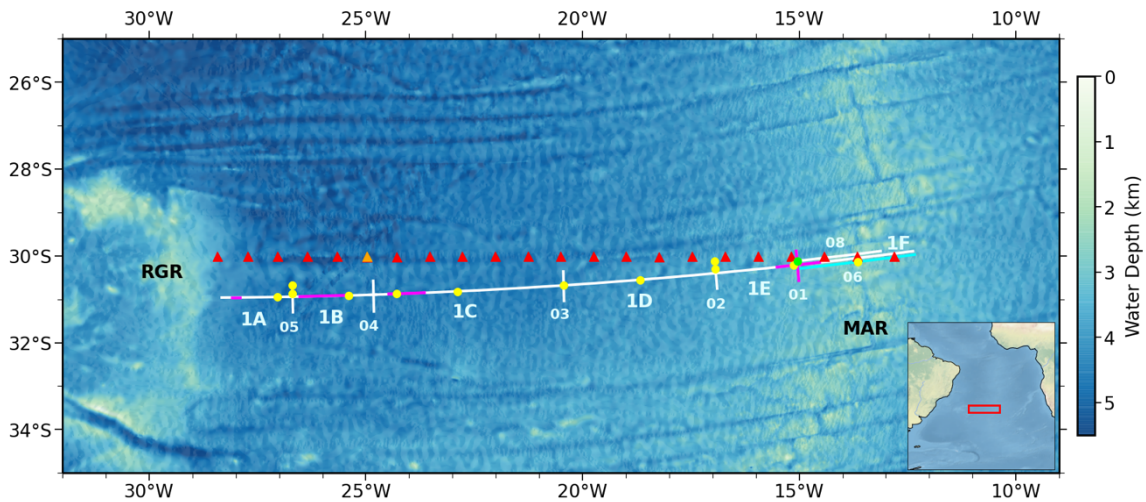
Figure 2.1: Bathymetric map of seismic survey location. Bathymetry from the Global Multi-Resolution Topography Synthesis (Ryan et al., 2009). White lines = seismic profiles collected between January 29th and February 14th 2016, labeled with line numbers (1A-1F, 01-08), line 06 is colored in cyan; purple lines represent segments of seismic images displayed in section 2.3.3; yellow dots = coincident XBT casts, green dot mark the XBT used for temperature calibration (Figure 2.9); red triangles = CTDs from GO-SHIP survey acquired in October 2011 (GO-SHIP 2003 CTDs within 0.5° of 2011 CTDs and are not shown); orange triangle = 2011 CTD station 69 used to produce synthetic seismogram in Figure 2.6; RGR = Rio-Grande Rise, MAR = Mid-Atlantic Ridge. Inset shows regional setting, with red box marking location of the study area.
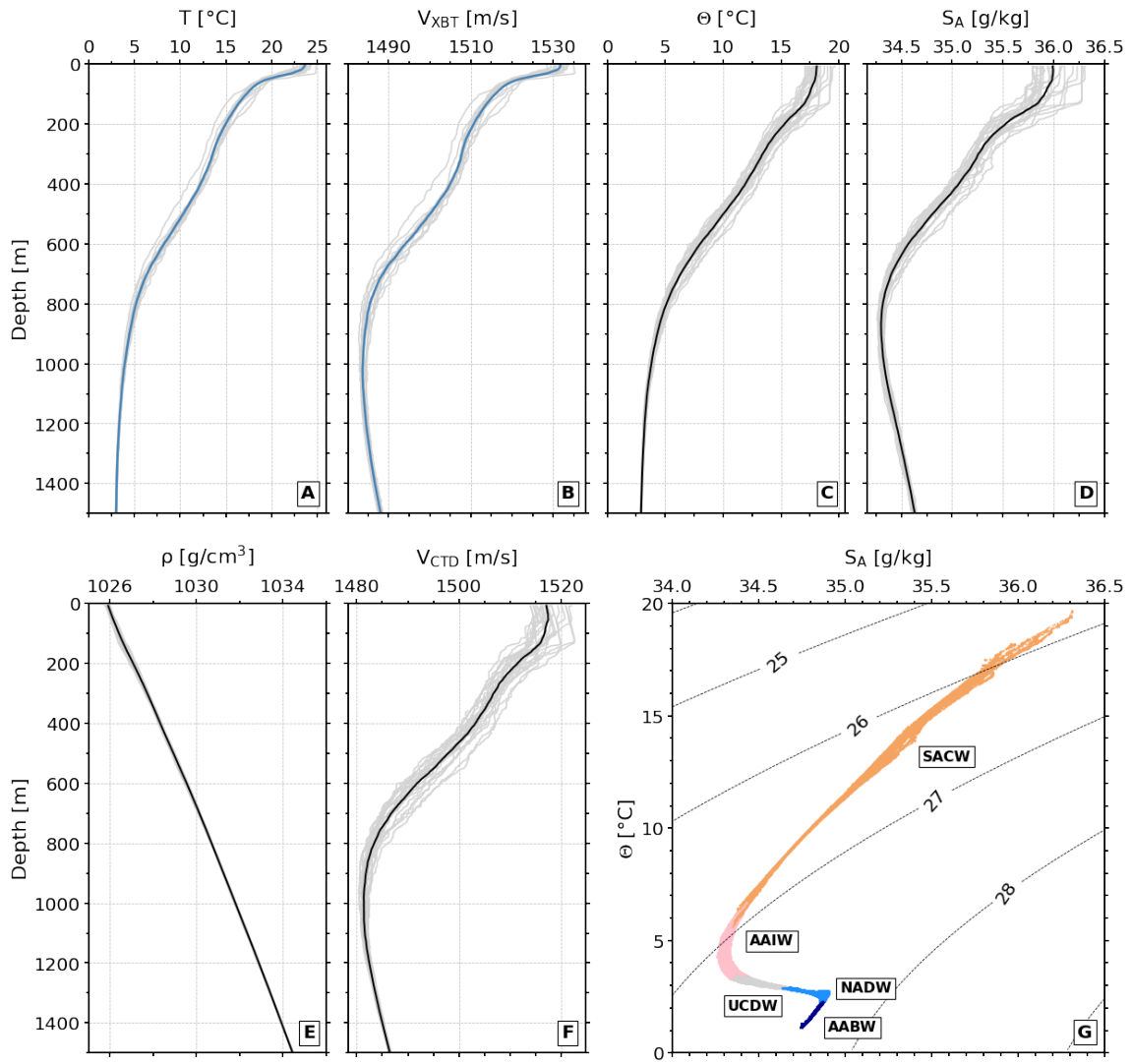
Figure 2.2: Water properties from 13 coincident XBT casts and 22 GO-SHIP 2011 CTD casts (yellow dots and red triangles in Figure 2.1, respectively). (A-B) In situ temperature (T) and Sound speed (V_{XBT}) from XBTs as a function of depth, respectively. Blue line = average profile; grey lines = individual profiles. (C-D) Conservative temperature (Θ) and Absolute salinity (S_A) from CTDs as a function of depth, respectively. Black line = average profile. (E-F) Density (ρ) and sound speed (V_{CTD}) calculated from CTDs as a function of depth, respectively. (G) Conservative temperature (Θ) – Absolute salinity (S_A) diagram. Points colored according to the water mass definition of Hernández-Guerra et al. (2019). Orange dots = South Atlantic Central Water (SACW); pink dots = Antarctic Intermediate water (AAIW); grey dots = Upper Circumpolar Deep Water (UCDW); blue dots = North Atlantic Deep Water (NADW); dark blue dots = Antarctic Bottom Water (AABW). Labeled dotted lines = potential density anomaly surfaces.

2.2. Data and Methods

2.2.1. Seismic Data and Processing

2-D multichannel seismic (MCS) data was acquired aboard R/V Marcus G. Langseth during the CREST survey (Estep et al., 2019). The survey starts from the eastern edge of the Rio-Grande Rise to the Mid-Atlantic Ridge at 30˚S, producing seismic profiles of total length of ~2683 km. The MCS data includes five ridge-parallel profiles, and an east-west 1500 km ridge-normal profile located in the center of the South Atlantic Subtropical Gyre. The data provides an opportunity to study the detail of water mass structures at this important location that covers one of the major pathways of meridional overturning circulation.

During the seismic acquisition, a 36 air-gun array, with a total volume of 6600 in^3, emitted 5-120 Hz signals at regular interval of 37.5 m. Reflected signals were recorded using a 12.6 km streamer that contains 1008 channels with 12.5 m spacing. The survey repeatedly sampled subsurface points with a 6.25 m interval, also known as common mid-points (CMPs). In order to image thermohaline fine structures as deep as possible, while not introducing too much noise, we used 800 near channels during seismic data processing. We imaged the water column of the central South Atlantic down to ~1600 m depth, covering both SACW, AAIW and UCDW. We mainly focus on analyzing water masses below 200 m as the upper ocean is dynamically affected by the interaction between ocean surface and the atmosphere, and the CREST seismic acquisition geometry is not well suited for imaging shallow water structures (Piété et al., 2013)

9

In an effort to achieve optimal imaging of thermohaline structures using legacy seismic data, we process the data using a workflow that is designed for water column reflectivity which is much weaker compared to the solid earth, and is more sensitive to noise contamination. The seismic processing workflow includes: spectral analysis, band-pass filter (20-90 Hz), water bottom muting, median filter, frequency-wavenumber (F-K) filter, amplitude corrections, velocity analysis, normal moveout correction (NMO), stretch muting, stacking, random noise attenuation by machine learning and post-stack time migration (Yilmaz, 2001). Median filter and F-K filter applied to pre-stack shot gathers and are used to enhance the signal-to-noise ratio of the water column seismic reflectivity by removing coherent noise. In addition, with the intention of reliably deriving physical properties and dynamical parameters from seismic images, a supplemental step of noise attenuation by machine learning is applied on the stacked sections before migration to remove random noise. Median filter, F-K filter and random noise attenuation workflows, specifically designed for use with legacy marine MCS data to study the water column, are detailed in the following sections.

2.2.1.1. Direct Wave Removal

Direct waves are high amplitude linear events in the shot gathers that dominate the upper ~2 seconds two-way-traveltime (TWTT) of the water column (Figure 2.3A). They are caused by energy that travels from the source directly to the receivers along the surface of the ocean. They are generally neglected during data processing of the solid earth since the entire water column is muted. However, the removal of direct waves is crucial for seismic oceanography since they overprint the reflections where the sharpest thermohaline

10

gradients exist. A median filter is designed to remove direct waves based on their known linear move-out; the operation is performed on individual shot gathers. First, an optimal sound speed that successively flatten the direct wave through a linear move-out correction is selected from coincident XBT measurements close to the ocean surface (Figure 2.3B). Second, a moving average is applied to enhance the horizontal continuity of the flattened direct wave while decreasing the coherency of non-linear events such as reflections. Third, the smoothed gather is subtracted from the linear move-out corrected input gather (Figure 2.3C), so that the flattened direct wave is removed. Lastly, inverse linear move-out is applied to the input gather to restore reflection signals back to original shape (Figure 2.3D).
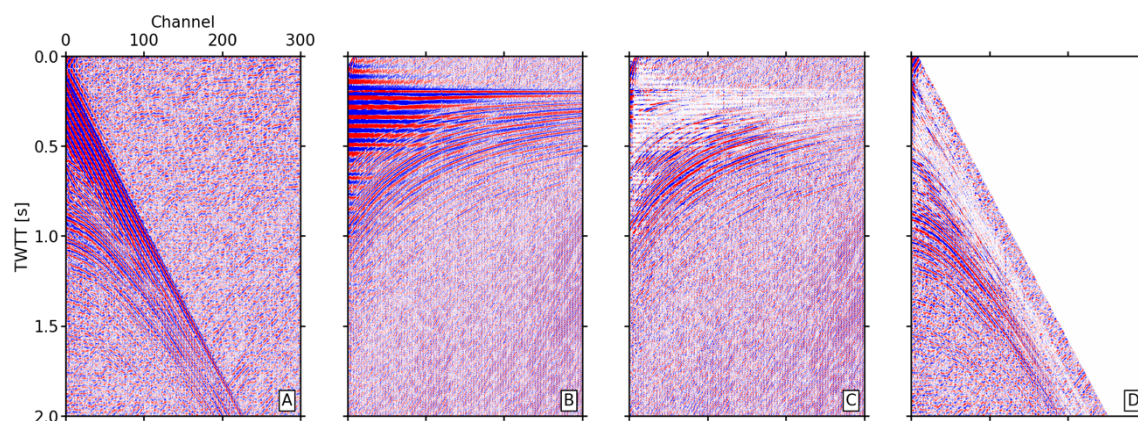
Figure 2.3: Example of direct wave removal. (A) Input shot gather dominated by direct wave. (B) Direct wave is flattened by applying linear move-out correction. (C) Direct wave is subtracted from the input shot gather. (D) Final shot gather after inverse linear move-out applied.

2.2.1.2. Previous Shot Multiple Removal

The shot spacing of 37.5 m was chosen to increase the horizontal sample rate in order to maximize fold, or the number of CMP gathers per stack, to increase the signal-to-noise ratio of the seismic image. However, 37.5 m is small enough to generate strong reverberations between the sea surface and the seafloor. Smaller shot spacing means the signal is emitted more frequently, and that reverberating, or multiple, reflections are still present in the water column when the subsequent shot is fired. This scenario is especially prevalent when the seafloor has a high reflection coefficient, such as from igneous rocks. As a result, high amplitude seafloor multiple reflectors from the previous shot overprint the primary water column reflectors of the current shot. This is not unusual in marine MCS datasets for which the acquisition geometry and recording time were originally designed to image the solid earth. Although the survey contains high fold during stacking, the contamination of strong multiples on the final image cannot be sufficiently addressed. At the same time, simple frequency filtering failed to remove these multiples since they share the same frequency range with primary reflections.

Within this survey, acoustic energy reverberation between the seafloor and ocean surface creates at least two detectable reflections, the primary seafloor reflection, and the first multiple seafloor reflection. In a geometric sense, previous shot multiples reflections in a shot gather of time-distance domain (t-x domain), do not exhibit the same hyperbolic curve shape of a primary reflection, but rather curves with significantly less degree of bending. The recorded wavefield in a shot gather (t-x domain) can be treated as a synthesis of many plane waves with different dips and frequency components, they are separable

12

through two-dimensional Fourier transform in the frequency-wavenumber (F-K) domain (Yilmaz, 2001). Thus, we can separate primary reflections from multiples based on their dip differences (curvature differences). First, two-dimensional Fourier transform is applied to the shot gather so that the data is transformed to F-K domain. Spatially aliased energy is removed by applying a dip filter between -1 and 8 ms/trace (Figure 2.4A, B, E, F). Secondly, after transforming back to the t-x domain, we apply an NMO correction with a constant velocity of 2500 m/s to over-correct multiples so that they dip upward while keeping reflections under-corrected so that they dip downward (Figure 2.4C). Correspondingly, by this means, multiples are mapped onto the negative quadrant in the F-K spectrum while reflections are still in the positive quadrant (Figure 2.4G). After applying a dip filter between -0.35 and 8 ms/trace, multiples are effectively removed. Lastly, an inverse NMO correction with same velocity of 2500 m/s is applied in the t-x domain to return reflections back to hyperbolic shape (Figure 2.4D, H). Normally, NMO correction is applied to CMP gather that contains signals reflected from the same point of the subsurface. The application of NMO to shot gather assumes that the reflectors in the water column do not have sharp dipping angles, and this is usually true as the thermohaline structures rarely dip higher than 10° (Sheen et al., 2011).
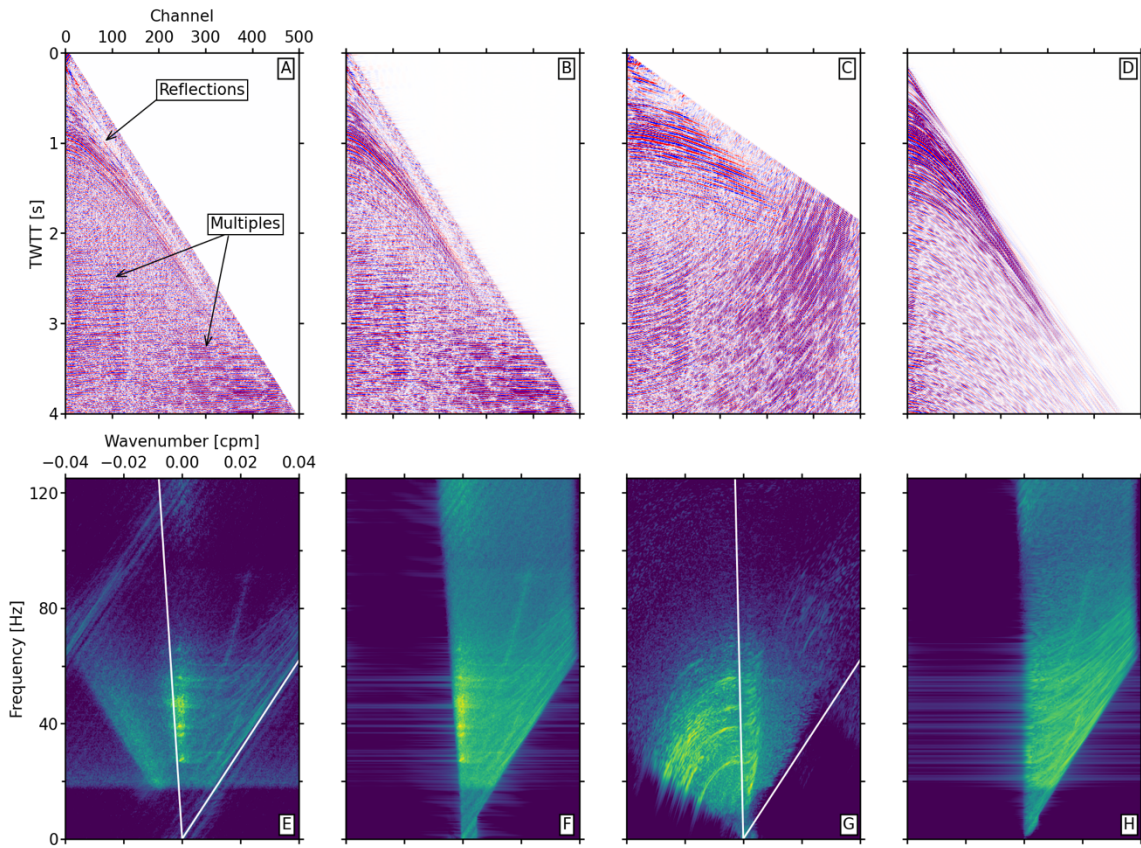
Figure 2.4: Example of multiple removal on the shot gather shown in Figure 2.3D. (A-D) Input shot gather, shot gather with aliased energy removed, shot gather with NMO correction applied, final shot gather with multiples removed. (E-H) Corresponding F-K spectrum of data shown from (A) to (D). White lines in (E) and (G) represent dip filters used to remove spatially aliased energy and multiple energy, respectively.

2.2.1.3. Random Noise Attenuation

The median filter and the F-K filter increased the signal-to-noise ratio significantly by removing major coherent noise in the data, however, random background noise from various sources during seismic acquisition, such as ocean swells and the vessel engine, is still present. The attenuation of random noise is important when extracting physical properties and dynamical parameters from seismic data. For example, Wei et al. (2022)

estimate diapycnal mixing rates from seismic images using the reflector slope spectra method, the shapes of reflector slope spectra are very sensitive to the level of noise contained in the seismic images (Holbrook et al., 2013). Therefore, random noise attenuation is necessary for SO studies. However, considering the low amplitude of water column reflections, traditional random noise attenuation techniques in reflection seismic processing may alter the reflection shapes and introduce artifacts. A noise attenuation method without damaging the reflection characteristics is needed.

More recently, Jun et al. (2020) explored the field of machine learning and developed a random noise attenuation method based on a denoising convolutional neural network (DnCNN) (Zhang et al., 2017). The DnCNN is capable of estimating noise from the seismic image instead of directly analyzing the raw signal, which preserves the original shape of water column reflection. Noise can be estimated during the model training and eventually subtracted from the noisy seismic image. Following Jun et al. (2020), we construct the training dataset by using random noise from CREST post-stack seismic sections and the noise-free Marmousi2 synthetic seismic section (Martin et al., 2006) (Figure 2.5). Marmousi2 synthetic data is used as ground truth. For CREST stack sections, random noise is assumed to have the same acoustic signature from the top to the bottom, therefore regions without reflections are treated as random noise (Figure 2.5A). One patch of training data has size of 50×50 pixels, and is produced by adding ground truth and random noise together after amplitude normalization to balance the amplitudes between the two (Figure 2.5B). Both ground truth and random noise are selected from random locations of seismic images during each iteration. The neural network is designed with

15

recommended parameters of 17 layers and a mini-batch size of 128, the number of iterations within each epoch is 220, resulting in 28160 training data patches in every epoch. After a series of tests, the model converges after 40 epochs and is applied to all the seismic lines.
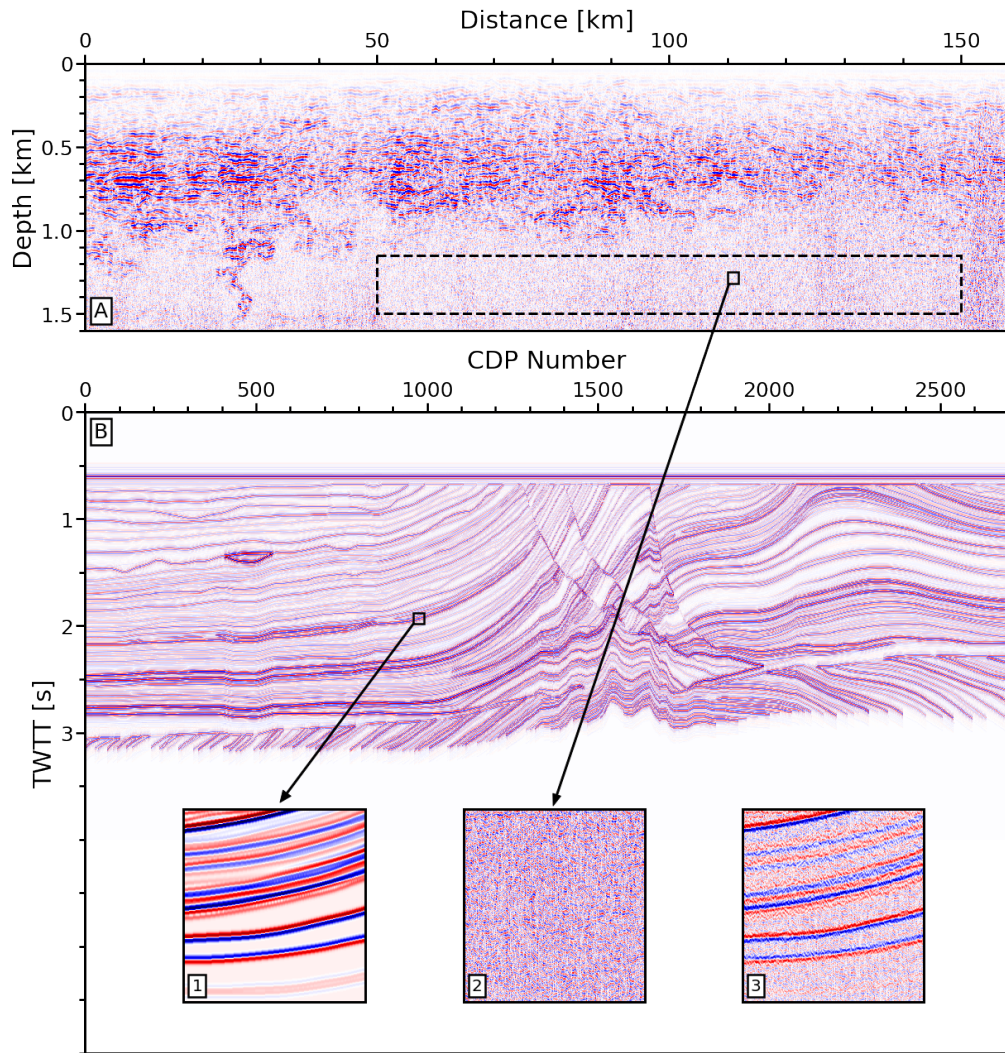
Figure 2.5: Construction of DnCNN training data. (A) Stack seismic section of line1A after direct wave and previous shot multiple removed. Dashed box indicates random noise data used to construct training dataset. Small box marks an example of random noise data patch. (B) Marmousi2 synthetic seismic section. Insets showing (1) random ground truth data patch, (2) random noise data patch, (3) noise-added training data patch.

2.2.2. Hydrographic Data

To provide additional constraints on the physical properties of the ocean and to aid our interpretation of seismically imaged water masses, we complement the CREST seismic data with hydrographic measurements. Coincident XBTs that measure temperature with depth, and have a vertical resolution of ~0.7 m, were collected during the CREST survey, and are used to calibrate seismically imaged thermohaline fine structures (Figure 2.7). Since the seismic images capture thermohaline structures up to 1400 m deep, XBT profiles with lengths shorter than 1400 m are discarded, resulted in 13 profiles (Figure 2.1). In addition, we use co-located legacy CTD data collected in November of 2003 and October of 2011 from repeat GO-SHIP surveys as time mean measurements of the water property at this location (Sloyan et al., 2019). CTDs measures temperature, salinity, and pressure with depth and are the primary hydrographic method used for accurate measurement of seawater properties. Both surveys span from ~17° E to 48° W at 30° S, and include 120 full water column CTD casts with ~30 nautical mile spacing and ~1 m vertical resolution. Large scale zonal water mass distribution of the South Atlantic were determined from these two datasets by previous studies (Talley, 2011; Hernández-Guerra et al., 2019), and is the foundation of our interpretation of seismically imaged water mass. We selected 22 and 23 CTD stations that lie in close proximity to the CREST seismic lines from the 2003 and 2011 survey, respectively (Figure 2.1). From these CTD measurements, we calculated sound speed profiles to support velocity analysis during seismic data processing, and produced synthetic seismograms that can be compared

directly to seismic images. The equations used to calculate the sound speed and density follow the UNESCO International Equation of State for Seawater (Fofonoff and Millard Jr, 1983).

2.2.3. Synthetic Seismogram

Seismic reflection is caused by the convolution of a source wavelet with impedance contrast between water masses, which is a function of sound speed and density. Sound speed and density of seawater is related to temperature and salinity through the empirical equation of state for seawater (Fofonoff and Millard Jr, 1983). By using CTD casts, we can calculate how sound speed and density, and therefore impedance contrast varies with depth. Since seismic data is recorded in two-way travel time (TWTT), CTD data is first converted from depth series to time series and resampled to 2 ms to match the sampling rate of the seismic data. The time series of acoustic impedance and reflection coefficient are subsequently computed and spherical divergence correction applied. Afterward, reflection coefficients are convolved with a Ricker (zero-phase) wavelet of central frequency 40 Hz to generate a zero-offset synthetic seismogram by assuming vertical propagation of wave energy. Ultimately, the seismogram is converted back to depth. The seismogram shows a stronger correlation to the derivatives of temperature and sound speed than salinity and density (Figure 2.6), suggesting temperature and sound speed have more contribution to reflectivity, consistent with the study by Sallarès et al. (2009). Modeling reflection coefficient from legacy CTDs offers a synoptic view of seismic reflectivity at the survey location. Although the legacy CTDs from GO-SHIP

repeating surveys are very sparsely sampled, they can provide a historical trend of reflectivity to help us understand the physical properties of water masses.
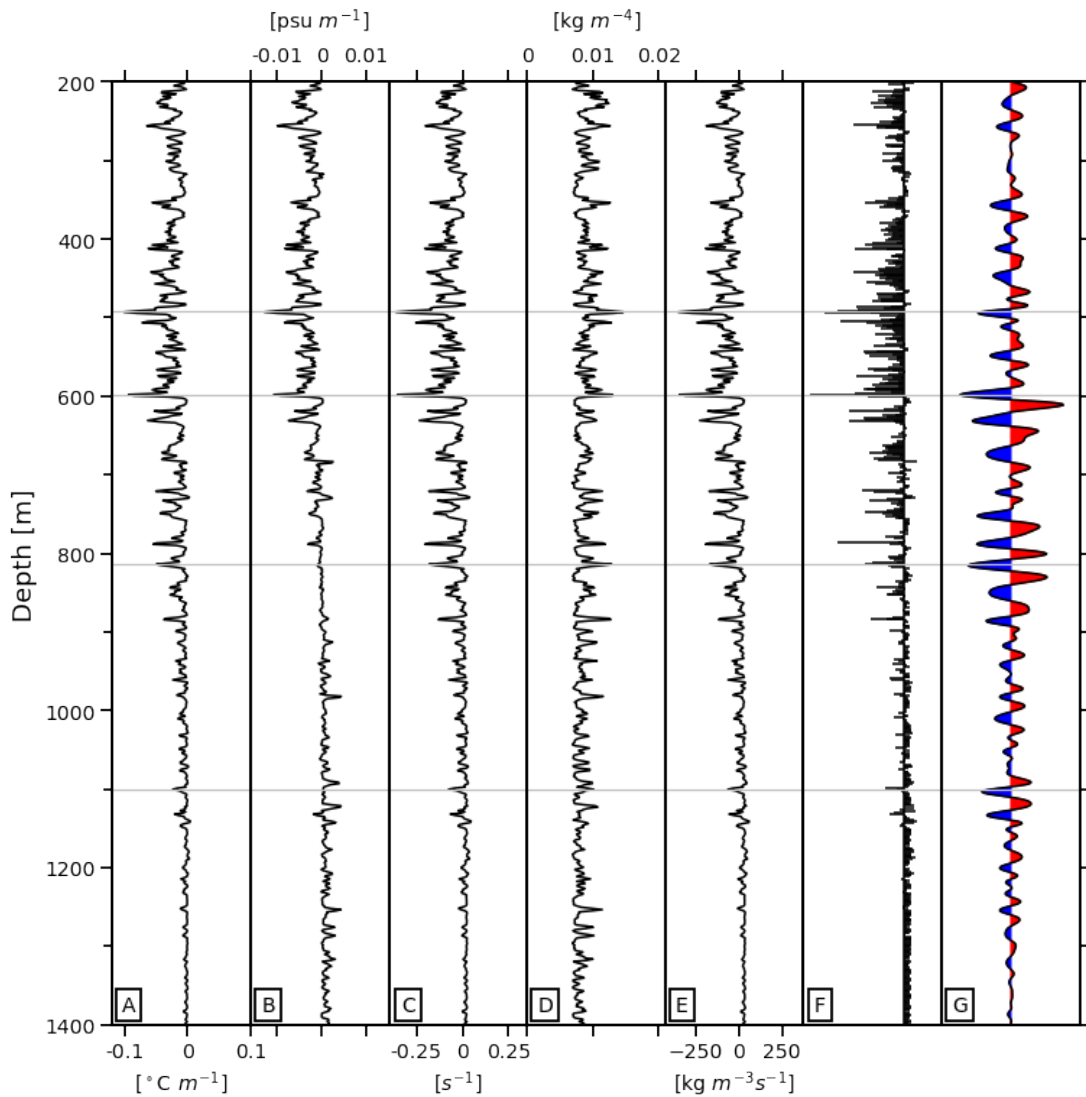
Figure 2.6: Temperature, salinity derivatives and stages in calculating synthetic seismogram. Vertical gradient of (A) potential temperature, (B) absolute salinity, (C) sound speed, (D) density, and (E) impedance, using 2011 GO-SHIP CTD station 69 (Figure 2.1, green triangle), and its corresponding reflection coefficient (F) and synthetic seismogram (G). Grey horizontal lines mark the similarities between peaks in each panel. Red and blue polarities represent positive and negative reflectivity.

2.3. Results

2.3.1. Noise Attenuation

The success of analyzing thermohaline structures using legacy seismic data depends on high signal-to-noise ratio of the final seismic images. As detailed in methods, three additional noise attenuation steps are applied to the CREST data: (1) median filter, (2) F-K filter and (3) DnCNN. The restoration of noise-covered reflections and improvements on reflection shapes and amplitudes are significant with each progressive step (Figure 2.7). Firstly, after median filter, the direct arrivals that overprint the first 300 m are removed (Figure 2.7A, B). Secondly, before the application of F-K filter, previous shot multiples appear as spatially repeating bands of high amplitude vertical noise stripes in the final seismic image, as shown in Figure 2.7B at range 10-55 km, data below 400 m depth are severely contaminated. After F-K filter, this noise is largely removed; a zigzag tail structure at 20-30 km below 1000 m that is unrecognizable before is now clearly imaged (Figure 2.7C). However, coherent noise remains in Figure 2.7C at 50 km, this noise is most likely generated by seismic wave diffraction and out-of-plane energy which cannot be sufficiently removed by the F-K filter. This is particularly true above the igneous seafloor of the Mid-Atlantic Ridge (MAR); strong diffraction and reverberation of seismic waves prevent us from imaging the thermohaline structures below 700 m (Figure 2.10). Finally, the removal of random noise by DnCNN greatly improves the continuity of reflections and increases the signal-to-noise ratio significantly (Figure 2.7D). One drawback of DnCNN application on the CREST dataset is that some weak signals in the deeper parts (800-1200 m) have been removed, this is probably caused by the application

20

of F-K filter that alters the randomness of noise signature. However, the merit outweighs the drawback since the reflections used for estimating mixing rates are strengthened (Wei et al., 2022).
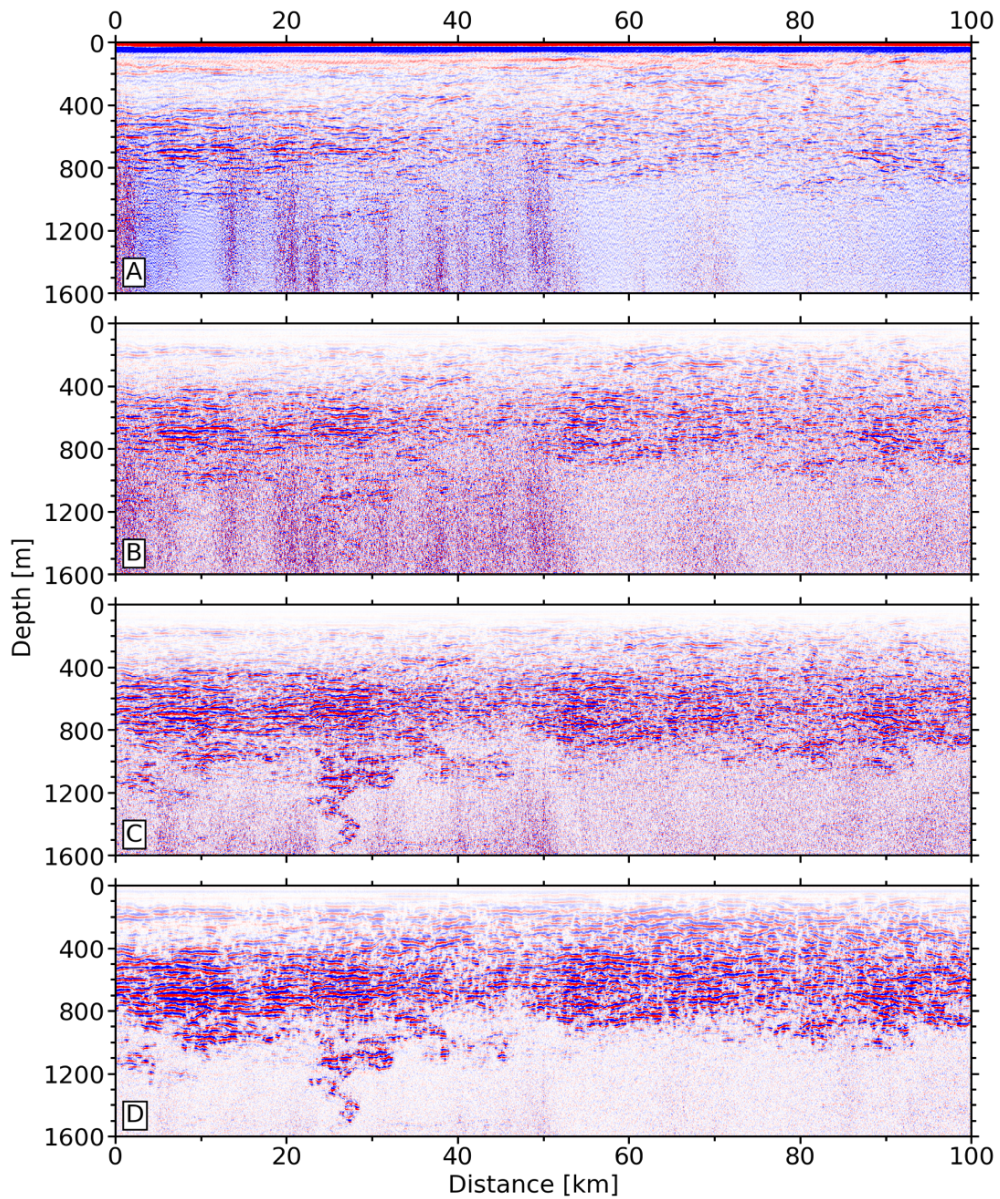
Figure 2.7: Migrated seismic images of the easternmost 100 km of line1A at different stages of denoising process. (A) Zero-phase bandpass filter of 30-90 Hz. (B) Direct waves removed using median filter. (C) Previous shot multiples removed using F-K filter. (D) Random noise attenuation with DnCNN.

2.3.2. Hydrographic Calibration of Seismic Images

Hydrographic measurements in the South Atlantic provide us with synoptic information about the physical properties of seawater on larger spatial scale as well as on longer time scale of more than a decade as they were collected in 2003, 2011, and 2016. Surprisingly, the water properties did not experience significant change below 200 m during this time span. Above 200 m, coincident XBT-measured temperature shows a shallower surface mixed layer compared to the 2011 CTD measurement which shows a mixed layer depth up to 100 m (Figure 2.2A, C); this is because the XBTs were collected in a much warmer season (January and February). Below 200 m, XBT- and CTD-measured temperature exhibit similar signatures; the average temperature of the two is ~15 °C at 200 m and decreases to ~5 °C at 800 m. Both show a higher temperature gradient between ~400-800 m. Similar signatures are also shown in the sound speed profiles (Figure 2.2B, F). Since temperature and sound speed are the dominant contributing factors to seismic reflectivity, the seismic characteristics of the central South Atlantic below 200 m likely changed little between 2011 and 2016. Similarly, from a 2D point of view, vertical sections of water properties changed little between 2003 and 2011 (Figure 2.8). Although spatial fluctuations exist at reference levels of different water masses, the distributions of temperature, salinity, sound speed and density is consistent. Therefore, during the time span of analysis (2003-2016), the physical properties of water at the survey location can represent the mean state and the historical hydrographic measurements of

22

2003 and 2011 can be used to produce synthetic seismograms that characterize the synoptic distribution of seismic reflectivity.

From the 2003 and 2011 CTDs and water samples, Hernández-Guerra et al. (2019) interpreted the vertical water mass distribution in the South Atlantic: South Atlantic Central Water (SACW) that extends from the surface to approximately 730 m, cooler fresher Antarctic Intermediate Water (AAIW) that occupies the 730-1140 m depth range and the Upper Circumpolar Deep Water (UCDW) from 1140-1560 m. Using the same CTDs, we calculated synthetic seismograms and produced vertical sections of seismic reflectivity for both 2003 and 2011 (Figure 2.8E, J). In both sections, there is a band of higher reflectivity between ~400 and ~800 m, corresponds to the lower half of highly stratified SACW. This band of reflectivity is thinner in the west and gradually becomes thicker to the east. Below 800 m, reflectivity diminishes showing less stratified AAIW and UCDW. The boundary between AAIW and UCDW is not clearly shown because of less temperature changes between them (Figure 2.8A, F). There is a similar mesoscale structure in both sections between 27° W and 24° W, we observe reduced reflectivity around 800-900 m and enhanced reflectivity from 1000 m to 1300 m, resulting in an isolated high reflective structure at depth 1000-1300 m. The detail of this structure can be seen from single synthetic seismogram in Figure 2.7G at 1100 m. The synthetic seismic sections suggest similar seismic characteristics of water masses on a broader spatial scale across nearly a decade, and they correspond well with previous oceanographic water mass interpretations (Talley, 2011; Hernández-Guerra et al., 2019). They can serve as time

mean measurements of seismic reflectivity and can be compared with the thermohaline

structures imaged by the CREST survey in 2016.
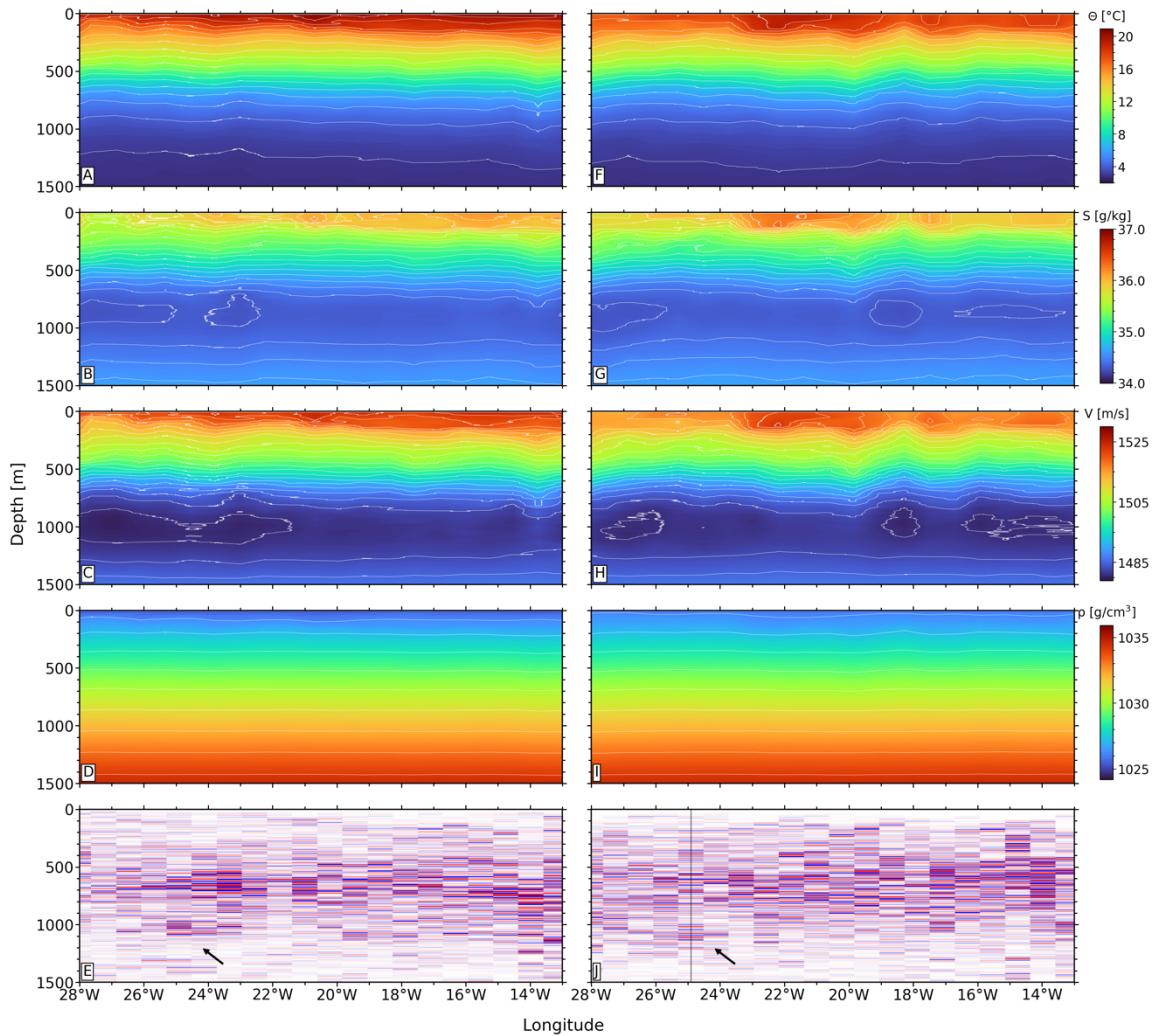
Figure 2.8: Vertical sections (0-1500 m) of physical properties of water masses and synthetic seismograms from GO-SHIP CTD casts. (A-E) Potential temperature, salinity, sound speed, density and synthetic seismogram from 2003 CTD casts. (F-J) Same for 2011 CTD casts. Vertical black line corresponds to the synthetic seismogram shown in Figure 2.7. Black arrows point to a region of isolated reflectivity explained in the text.

To accurately interpret seismically imaged thermohaline structures, it is also important to validate the seismic images against concurrent hydrographic measurements to show whether the seismic method faithfully captures physical changes in the water column. As demonstrated by Ruddick et al. (2009), seismic images are essentially smoothed maps of vertical temperature gradient. Therefore, we calculate temperature gradients from coincident XBT profiles and compare them with seismic imaged fine structures. We followed Nandi et al. (2004) by removing wavelengths greater than the dominant wavelength of the seismic source using a Butterworth high-pass filter. Wavenumbers greater than 1/(35 m), while smaller than the Nyquist wavenumber, are retained. The resulting temperature changes match seismic imaged fine structures remarkably. In the XBT data, for example, temperature changes faster with depth from 200 m to 300 m, and from 450 m to 800 m; correspondingly, the seismic reflections capture these sharp changes with higher amplitude responses, on a scale that equals the dominant wavelength (~30 m) of the seismic source (Figure 2.9). In the CREST survey, temperature changes measured by all selected XBTs match the seismic images near their collecting locations, which proves that the CREST survey reliably captures thermohaline fine structures in the central South Atlantic.
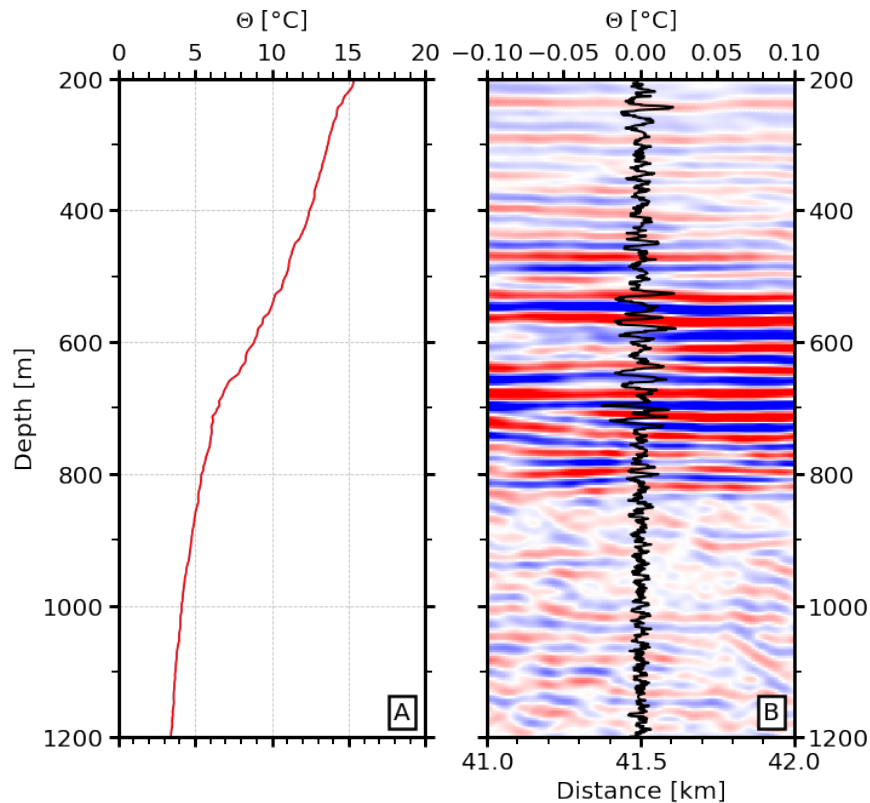
Figure 2.9: Correlation between seismic data and a concurrent XBT marked as green in Figure 2.1. (A) Temperature profile recorded by the XBT. (B) Short-wavelength temperature gradients (black line) of the profile shown in (A) overlie on the seismic section surrounding the collection location of the XBT.

2.3.3. Seismic Images of Thermohaline Fine Structures

The final processed seismic sections show images of the thermohaline structure along a ~1500 km long transect within the South Atlantic Subtropical Gyre (Figure 2.10), which reveals a substantially higher resolution view of thermohaline processes compared to hydrographic measurements (Figure 2.8). Vertically, three main layers with different reflection characteristics are observed. Firstly, an upper layer from the surface down to ~400 shows continuous reflections with weaker amplitude, mostly horizontal except at the end of line1A (120-160 km) and start of line1B (0-40 km), where reflections are dipping

26

toward the east, likely induced by surface dynamics. Secondly, a middle layer from ~400 m to ~800 m is characterized by stronger reflections that are spatially different in continuity, with some regions populated by stronger, continuous reflections (Figure 2.10, red boxes) while other regions are more disrupted (Figure 2.10, blue boxes). Thirdly, a lower layer below 800 m is characterized by stronger reflections at the top while relatively devoid of reflections after 1000 m. The first two seismic layers correspond to previous hydrographic identification of the highly stratified SACW (Hernández-Guerra et al., 2019), and compare well with the seismic characteristic of synthetic seismograms in the upper 800 m (Figure 2.8). The lower layer is more homogeneous and thus acoustically transparent and the depths corresponds to AAIW and UCDW (Talley, 2011). The transition from SACW to AAIW is diffuse, with interleaving strong and weak reflections occupying depths 800-1000 m. The transition layer is exhibited by a fluctuating pattern along the bottom of the middle layer along all the seismic sections, suggesting the depth of transition between the SACW and the AAIW undergoes large lateral variation, potentially caused by various mixing processes. For example, some regions show homogeneous patches within this transition layer (Figure 2.7D, at depths 800-1000 m, range 38-50 km); the patches may represent highly mixed parcels of AAIW entrained within SACW.
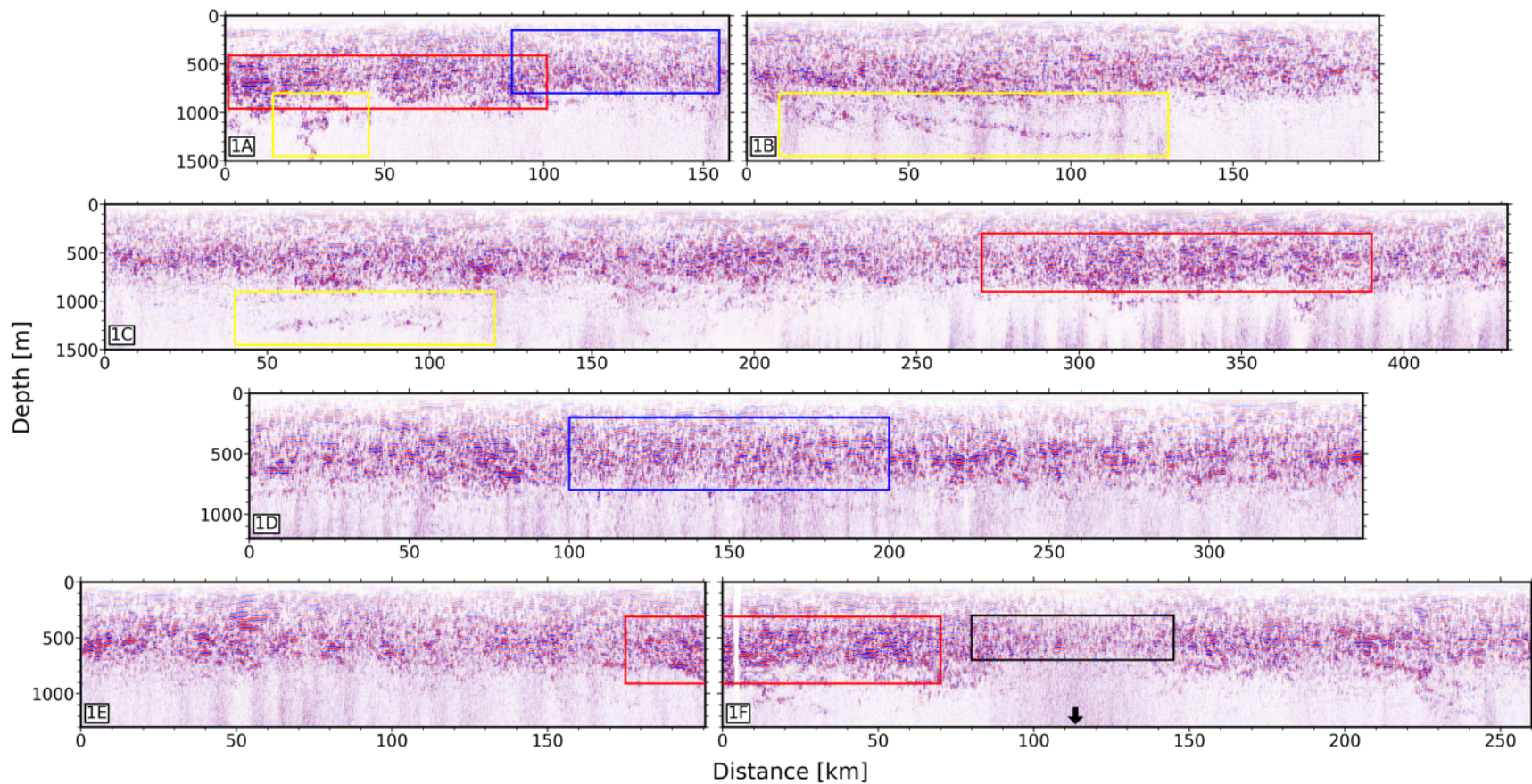
Figure 2.10: Final processed seismic sections from line1A to line1F. Red boxes mark examples of reflections with stronger and continuous amplitude; blue boxes mark examples of discontinuous reflections; yellow boxes mark some distinct mesoscale structures; black box marks weak and discontinuous reflections above the MAR. Black arrow points to the location of the MAR.

28

The seismically imaged thermohaline structures reveal mesoscale processes in the central South Atlantic for the first time. Several prominent mesoscale structures are presented and are summarized as follows:

(1) In line1A at 20-30 km below 1000 m, disrupted dipping reflections depict a zigzag tail structure that crosses AAIW into UCDW (Figure 2.7C, D; Figure 2.10, line1A, yellow box). The horizontal and vertical scale of this structure is about 8 km and 500 m, respectively.

(2) In line1B at 10-130 km around 1000-1200 m, disrupted reflections show an isolated thermohaline structure inclining to the east with acoustically transparent zone above and below the structure (Figure 2.11A). In line1C at a slightly deeper depth around 1200-1300 m at 40-120 km, similar thermohaline structure exists but reflections are more horizontal (Figure 2.11B). The horizontal scale of these two structures are 120 km and 60 km, respectively. Their geographic locations are between 27° W and 24° W, and their depths are between 1000-1400 m, match well with the isolated high reflectivity in the synthetic seismic sections (Figure 2.8E, J). The observation of these structures at the same location across long time period suggests they might be a permanent process at this location.

(3) At the intersection of line1E, 1F and 01, we observe a localized water mass that is characterized by continuous high amplitude reflections surrounded by weaker discontinuous reflections (Figure 2.12). The interaction of this water mass with the surrounding water generates a frontal structure that penetrates to a depth of 1300 m (Figure 2.12B, 10-30 km, 1000-1300 m).

(4) In the vicinity of MAR, seismic reflections are largely disrupted below 400 m, and several mesoscale structures with complex patterns of reflectivity are captured by seismic section of line06 (Figure 2.13), more specifically: (1) at range 40-70 km, between 600-1000 m, we observe a lens-shaped eddy-like structure; (2) from 145-160 km at depths 500-800 m, we observe a high amplitude reflective package with regular spaced layers (Figure 2.13, black box); (3) reflections directly above the MAR at range 110-140 km are much weaker and the thickness of thermohaline structures are much thinner; (4) at range 190-250 km, weaker reflections that form multiple filaments extend to 1500 m depth. These complex reflection patterns imply the water mass above the MAR is undergoing deformation and displacement that enhance mixing.
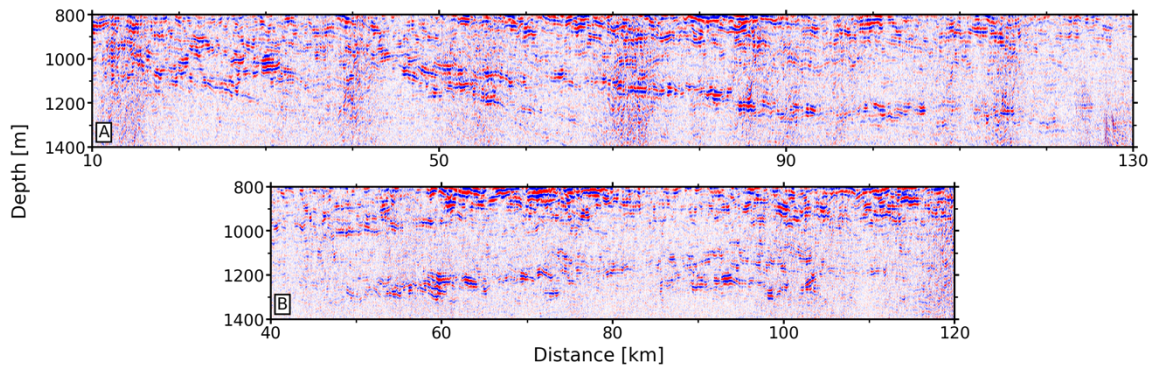
Figure 2.11: Enlarged images of yellow boxes in Figure 2.10 showing two isolated thermohaline boundary structures for (A) line1B and (B) line1C, respectively,. Locations of these two structures are marked by magenta line in Figure 2.1.
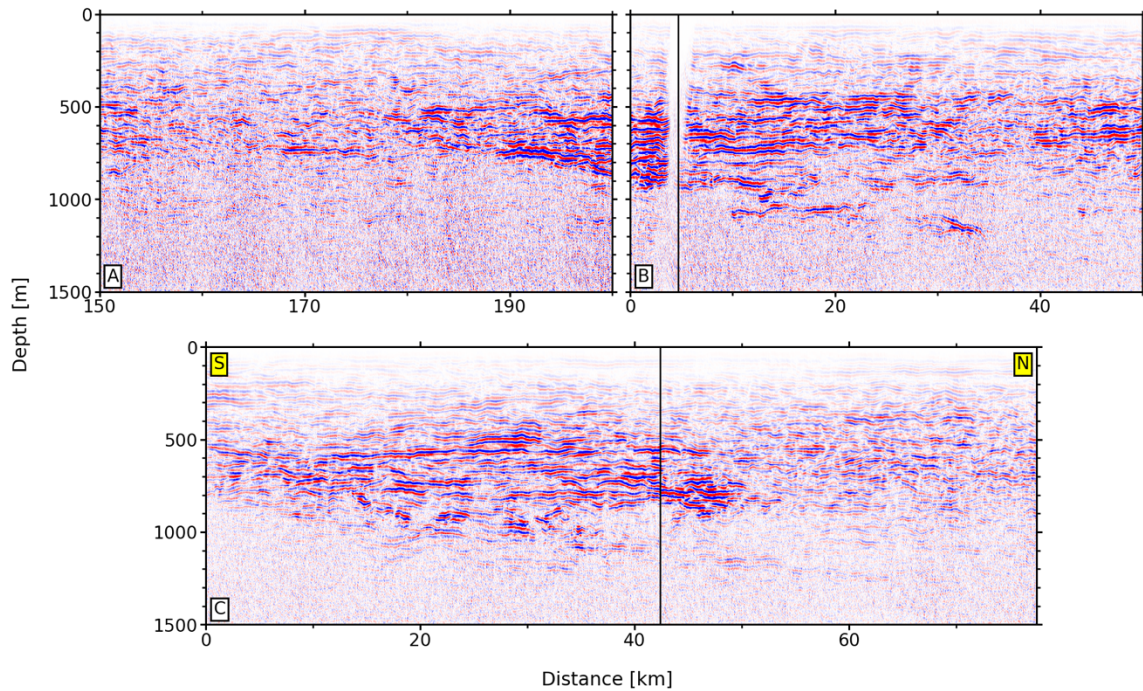
Figure 2.12: Intersection of seismic sections line1E, 1F and 01 showing a high amplitude localized water mass. (A-B) Enlarged images of red boxes in Figure 2.10 for easternmost of line1E (A) and westernmost of line1F (B). (C) Seismic section of line01, the direction is labeled in upper corners. Vertical black lines mark the location of the intersection. In Figure 2.1, the location of this intersection is marked by a magenta crossing.
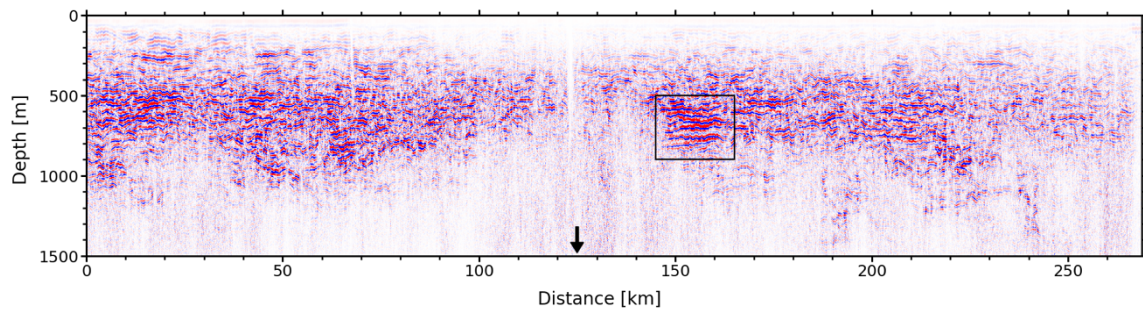
Figure 2.13: Seismic section of line06. The location of this section is colored in cyan in Figure 2.1. Black box marks a package of high amplitude undulating reflections. Black arrow points to the location of the MAR.

2.4. Discussion

Our seismic observation in the quiescent central South Atlantic reveals a large number of mesoscale structures, suggesting the complexity of physical processes in the open ocean. On a general view, most of the reflections undulate vertically, with a displacement ~25 m and horizontal wavelength of hundreds of meters. We also observe vertically-adjacent reflections displaced up and down coherently (e.g., Figure 2.13, black box); these are clear indicators of internal waves (Garrett and Munk, 1975; Holbrook and Fer, 2005). Stronger stratification is created by larger temperature gradient and therefore exhibited by stronger seismic reflections. Across all seismic sections, we see the alternate appearance of clusters of stronger, continuous reflections and clusters of weaker, disrupted reflections, which might imply the presence of sources of disturbance that leads to breaking of internal waves and weakens the stratification, resulting in weaker, disrupted reflections at some locations (Fortin et al., 2016; Dickinson et al., 2017). The presence of stronger and weaker reflections demonstrates the fact that diapycnal mixing, the mechanism that brings denser water upwards to maintain the overturning circulation, is not confined to a fixed rate, but is rather heterogeneous in the open ocean (Sloyan, 2005).

Compared to boundary regions, the open ocean is calmer and more stratified (Garzoli and Matano, 2011). As expected, the seismically-imaged thermohaline structures of the mid-South Atlantic in this study are absent of eddy-like processes, except one eddy observed above the MAR. However, numerous mesoscale and sub-mesoscale structures suggest that dynamical processes are prevalent in the open ocean interior. The largest amount of mesoscale structures, such as interleaving, filaments, and water mass

entrainment, are located at the transition layer between SACW and AAIW. Their formation are likely the result of the layering of warmer, saltier water (SACW) over cooler, fresher water (AAIW), a typical oceanic setting in the subtropical ocean (Talley, 2011), the interactions between the two water masses is dominated by double diffusion and thermohaline intrusion (Ruddick and Richards, 2003). Double diffusion will erode vertical gradients of temperature and salinity over time (Ruddick and Gargett, 2003), characterized by the fading reflections in the seismically imaged transition layer at depth 800-1000 m. Thermohaline intrusions are imaged as quasi-horizontal reflections as the trapping of AAIW water parcels within SACW leads to lateral advection and forms sloping interleaving salt fingers (Ruddick and Richards, 2003). The prevalence of mesoscale structures at the transition layer suggests large mesoscale variability between water masses in the open ocean, although these mesoscale processes are not as energetic as those in the boundaries such as Brizil-Falkland confluence zone (Sheen et al., 2012; Gunn et al., 2020), they affect the transport of heat and energy of the returning limb of the meridional overturning circulation in the central South Atlantic (Garzoli and Matano, 2011). Together with concurrent hydrographic measurements, the seismic method is able to contribute to the quantification of meridional transport in the South Atlantic which is still suffering from large uncertainties (Garzoli et al., 2013; Dong et al., 2014; Dong et al., 2015).

Some prominent mesoscale structures shown in section 2.3.3 are discovered for the first time, however, their formation cannot be well explained without contemporary hydrographic measurements. For example, the tail structure in line1A at range 20-30 km is extraordinarily unexpected in the environment of central South Atlantic (Figures 2.7,

2.10). The shape and horizontal scale of the structure resembles the large horizontal vortex imaged at the Brazil-Falkland confluence zone where the North Atlantic Deep Water converges with Antarctic Circumpolar Water and strong thermohaline intrusion happens (Sheen et al., 2012). The vertical scale is about several hundred meters smaller. However, the central South Atlantic is a much more quiescent region compared to the energetic western boundary. The strong and continuous reflections above this tail structure indicate stable stratification, which means it is unlikely caused by any surface forcing. The structure is most likely caused by strong thermohaline intrusion of convergent flows, however, the water masses on both sides of the structure are both acoustically transparent, suggesting no significant differences in water properties and making the formation of this structure a mystery. Another example is the isolated boundary-like structure shown in both line1B and line1C (Figure 2.10). The comparison between seismic images and CTD-derived synthetic seismic sections indicates the structure has likely existed for more than a decade, suggesting a long-term stability of the influencing processes. We hypothesize that the cause may be the thermohaline intrusion during the recirculation of AAIW within the Brazil Basin (Boebel et al., 1997; Schmid et al., 2000). It is worth noting that the boundary in line1B is tilted toward the east, consistent with the reflections in the shallower depths, indicating that a strong shear event from surface forcing affects the deep ocean, probably accompanied by enhanced mixing. The emergence of the two mesoscale structures discussed above is unexpected as they are unaware to the scientific community, again, demonstrating the importance of studying mesoscale processes in the open ocean.

Mesoscale structures above the MAR are more easily interpreted because the mid-ocean ridges are important topographic features that generate intense diapycnal mixing when internal tides flow over them (Polzin et al., 1997; St Laurent and Thurnherr, 2007). The disrupted reflections and increased mesoscale structures clearly indicate a strong field of internal waves (Figures 2.10, 2.13). Moreover, reflections directly above the MAR are much weaker, likely caused by the large extent of upward penetration of diapycnal mixing (Li and Xu, 2014). Unfortunately, seismic diffractions and strong multiples contaminate signals below 700 m, rendering images unsuitable to study the more intense mixing directly above the MAR. The strong noise above the igneous MAR also provides implications for future SO acquisitions. When planning the survey, it is crucial to consider the hardness of the seafloor and the depth of the water column in order to determine optimized shot spacing and recording time to minimize the influence of multiples and diffractions.

2.5. Conclusion

In this research, we use seismic oceanography to study the mesoscale processes in the central South Atlantic using legacy multichannel seismic data acquired in February 2016, covering a zonal transect of ~1600 km-long from the western edge of the Rio-Grande Rise to the Mid-Atlantic Ridge at 30° S. With the development and implementation of appropriate seismic processing workflow for legacy seismic data, we are able to largely attenuate coherent and random noises that contaminate the weak water column reflections and successfully image the thermohaline fine structures in the Central South Atlantic down to ~1600 m. The resulting seismic reflectivity matches well with

previously identified water mass distribution by hydrographic measurements, covering three major water masses at an important transect of meridional overturning circulation: South Atlantic Central Water, Antarctic Intermediate Water and Upper Circumpolar Deep Water.

Across the entire transect, seismic images are characterized by intermittent appearance of strong and weak seismic reflections, suggesting the stratification in the open ocean interior is not uniform, implying heterogeneity of diapycnal mixing. Seismic images also reveal large mesoscale variability: at the transition zone between South Atlantic Central Water and Antarctic Intermediate Water, the seismic images exhibit numerous mesoscale structures that are associated with internal waves, double diffusions and thermohaline intrusions; in the vicinity of the Mid-Atlantic Ridge, disrupted reflections form complex mesoscale structures suggesting enhanced mixing caused by internal tides flow over rough topography. Two prominent mesoscale structures of mysterious origin that are impossible to discern with conventional oceanographic measurements are discovered for the first time, suggesting the suitability of seismic oceanography in resolving mesoscales and our limited understanding of physical processes in the open ocean interior.

Our study demonstrates the necessity of exploring mesoscale processes in the ocean interior, aided with concurrent hydrographic measurements, seismic oceanography is able to make significant contribution to the understanding of ocean dynamics and circulation. In addition, our study continues the effort of exploring legacy multichannel seismic data as an useful tool for physical oceanography, however, new techniques that

36

can suppress coherent noise such as diffractions without jeopardizing weak water column reflections are needed in order to explore more physical oceanography processes from legacy seismic datasets.

3. MID-OCEAN RIDGE AND STORM ENHANCED MIXING IN THE CENTRAL SOUTH ATLANTIC[*]

3.1. Introduction

Turbulent diapycnal mixing maintains global overturning circulation (Munk and Wunsch, 1998). Diapycnal mixing is primarily caused by breaking of internal waves that transfer energy from large to small scales, ultimately leading to irreversible mixing. Understanding the spatial and temporal distribution of mixing is important in developing ocean circulation and climate models (Harrison and Hallberg, 2008). Analytical modeling suggests that an average diffusivity of $O(10 \times 10^{-5})$ m^2 s^{-1} is required to maintain abyssal stratification (Munk and Wunsch, 1998), whilst $O(1 \times 10^{-5})$ m^2 s^{-1} is required in the main thermocline (Lumpkin and Speer, 2007). However, diapycnal mixing is extremely patchy in the real world and presents a unique observational challenge.

Enhanced mixing is mostly concentrated above rough topography such as ridges (Polzin et al., 1997; Klymak et al., 2006) and seamounts (Kunze and Toole, 1997), and is associated with sustained wind input (Price et al., 1986). Barotropic tidal energy converts to internal tide energy when it flows over topography (Munk, 1966; Munk and Wunsch, 1998; St. Laurent et al., 2001); energy input from wind propagates into the ocean interior by generating near-inertial energy in the upper ocean mixed layer (Gill, 1984;

---

[*] Reprinted with permission from "Mid-Ocean Ridge and Storm Enhanced Mixing in the Central South Atlantic Thermocline" by Wei, J., Gunn, K. L., and Reece, R., 2022. *Frontiers in Marine Science*, 8, 771973, doi: 10.3389/fmars.2021.771973, Copyright 2022 by Wei, Gunn and Reece.

D'Asaro, 1985; D'Asaro et al., 1995; Alford, 2003a). It is clear that external energy supply for the internal wave continuum comes from tides and winds primarily. Less is known about mixing in the ocean interior, away from rough topography and strong coastal winds, in particular in the central South Atlantic thermocline due to an historical lack of observations.

Via a subtropical gyre, the South Atlantic transports surface water equatorward to compensate the southward flow of the North Atlantic Deep Water (Garzoli and Matano, 2011; Cabré et al., 2019). Previous research in the South Atlantic has mostly focused on low-frequency variability of its large scale circulation (Stramma and England, 1999; Dong et al., 2015), or mesoscale variability near boundaries like the Brazil-Falkland confluence (Garzoli, 1993; Valla et al., 2018). The Brazil Basin Tracer Release Experiment (BBTRE) is the only microstructure survey in the mid-ocean of the South Atlantic (Polzin et al., 1997). The BBTRE collected microstructure measurements and discovered heightened mixing throughout much of the water column above the Mid-Atlantic Ridge (MAR). Diffusivities exceeding 100×10^{-5} $m^2 s^{-1}$ were found within 150 m of the sea floor, whilst rates of 1×10^{-5} $m^2 s^{-1}$ are found above smooth plains (Polzin et al., 1997; Ledwell et al., 2000; St. Laurent et al., 2001). Since this experiment in the late 1990s, there has been no further direct observations of diffusivity above the MAR so it is unknown if the observed enhanced mixing rates are representative of the mean state. At basin scales, finescale parameterization applied to Argos and Conductivity-Temperature-Depth (CTD) probes has shown that the distribution of mixing in the South Atlantic interior is spatially patchy and temporally intermittent (Sloyan, 2005; Whalen et al., 2012).

However, these studies mostly focus on the global pattern of mixing; the origin and evolution of the patchy mixing in the quiescent mid-ocean remains unknown.

More recently, studies have shown that storms are an effective method of wind energy injection (Dohan and Davis, 2011). In the wake of storms, diapycnal diffusivity is enhanced by 9×10^{-5} $m^2 s^{-1}$ (Jing et al., 2015). Quantifying the effect of storms on oceanic mixing is especially difficult as they are moving short duration events. Conventional one-dimensional (1D) hydrographic measurements such as CTDs and Vertical Microstructure Profilers (VMPs) are unlikely to capture their effects. In particular, little is known about how storms contribute to mixing in the quiescent ocean interior, especially in basins like the central South Atlantic that are not covered by storm tracking system such as NOAA. In a warming world with increasing storm intensity (Walsh et al., 2019), it is important to develop two-dimensional (2D) tools that can yield a deeper understanding of the effects of storms on ocean mixing.

Seismic oceanography (SO) is a powerful tool that can be used to overcome these observational gaps. SO provides observations of physical processes across horizontal length scale of $\sim O(10^5)$ m to $\sim O(10^2)$ m (Ruddick, 2018). The method utilizes low frequency (e.g., 5-120 Hz) acoustic sources and towed cable(s) containing a dense array of hydrophones to receive acoustic energy that is transmitted and reflected at boundaries created by temperature and salinity differences. Nandi et al. (2004) demonstrated that SO is able to capture temperature difference as small as 0.03 °C. Sallarès et al. (2009) further confirmed that reflectivity has a stronger correlation with temperature than salinity. The frequency bandwidth of the acoustic source is capable of imaging thermohaline fine

structure with lateral and vertical resolutions on the order of 10 m, meaning that the method is capable of mapping mesoscale structures such as fronts, internal waves, eddies that are always missing in conventional hydrographic measurements. This relatively high resolution makes SO an ideal method for turbulence mixing analysis. Studies that calculated turbulent diffusivities from slope spectra of seismic reflections demonstrate the suitability of the method in exploring spatial and temporal changes of mixing (Sheen et al., 2009; Fortin et al., 2016; Mojica et al., 2018; Dickinson et al., 2020; Tang et al., 2020). The instantaneous spatial distribution of mixing derived from seismic data represents a near-full energy cascade from internal waves to turbulence (Ruddick, 2018), implying the potential use of seismic derived parameterization in future ocean models (Tang et al., 2021). When combined with hydrographic data, seismic oceanography studies can be used to overcome significant observational gaps.

Here, we present and analyze a ~1600 km-long 2D seismic transect starting from the eastern edge of the Rio Grande Rise (RGR) to the MAR, covering one of major pathways of the Atlantic meridional overturning circulation (Figure 3.1). We calculate diapycnal diffusivities across the thermocline using the slope spectra method with seismic sections, as well as using finescale parameterization with CTD and Argo data. Our primary objective is to examine the spatial distribution of mixing in the central South Atlantic thermocline and extend its observational record. We also present the most likely hypotheses for drivers of enhanced mixing. Our results extend the observational record of diapycnal mixing in the central South Atlantic thermocline by providing diffusivities in

41

2003, 2011, and 2016, and provide further insights into the drivers of mesoscale mixing variability.
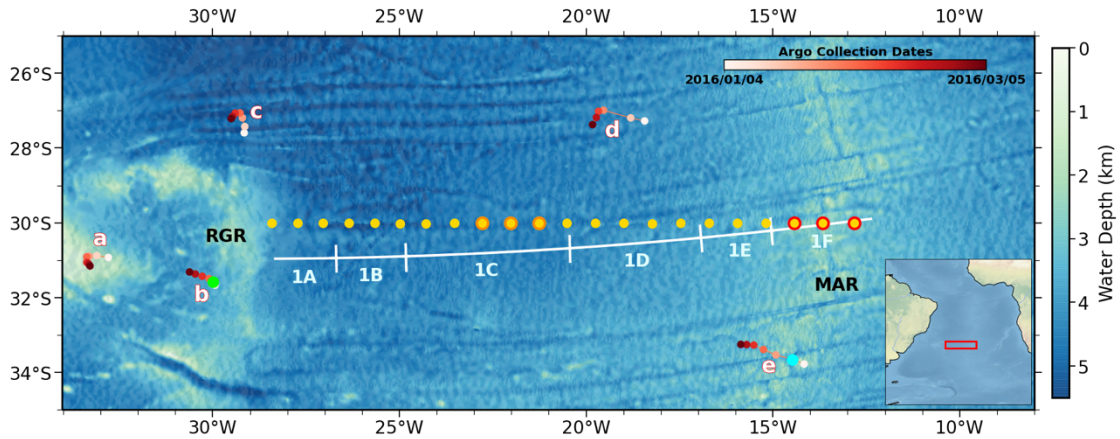
Figure 3.1: Bathymetric map of seismic survey location. Bathymetry from the Global Multi-Resolution Topography Synthesis (Ryan et al., 2009). White lines = seismic profiles collected between January 29th and February 14th 2016, short meridional lines mark the connection point between zonal lines; yellow dots = CTD casts from GO-SHIP survey acquired in October 2011, yellow dots with orange/red edges correspond to orange/red profiles in Figure 3.2 (GO-SHIP 2003 CTDs within 0.5° of 2011 CTDs and are not shown); red dots = Argo float trajectories between January 4 and March 5 2016, labeled a – e; green and cyan dots = Argo floats used for mixing calculation to compare with seismic results in Figure 3.6; RGR = Rio-Grande Rise, MAR = Mid-Atlantic Ridge. Inset shows regional setting, with red box marking location of the study area.
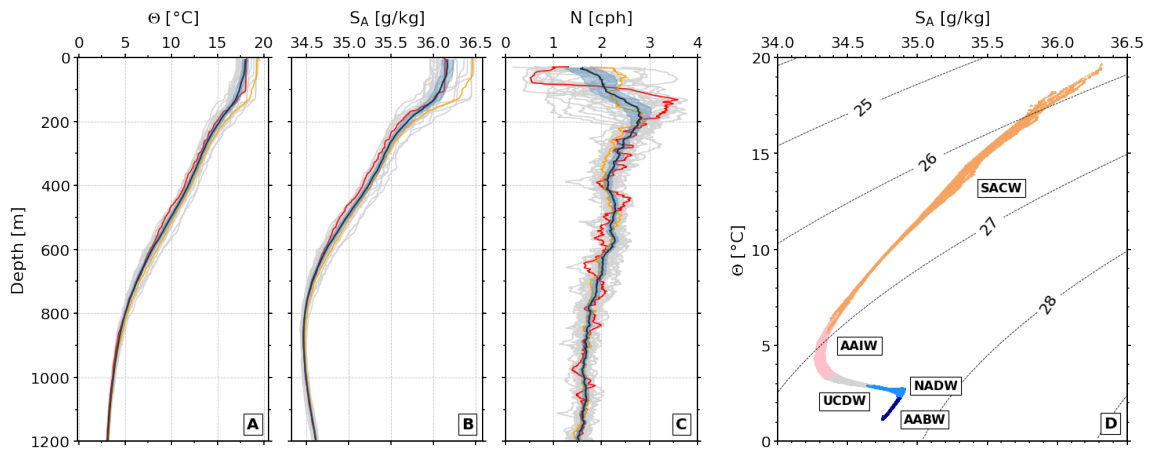
Figure 3.2: Water properties from 22 GO-SHIP 2011 CTD casts. (A) Conservative temperature, Θ , as a function of depth. Black line = average profile; grey lines = individual profiles; blue patch = 95% confidence interval; red/orange lines = average profiles of CTDs with red/orange edges (Figure 3.1). (B) Absolute salinity, S_A, as a function of depth. (C) Buoyancy frequency, N, as a function of depth. [cph = cycles per hour]. (D) Conservative temperature (Θ) – Absolute salinity (S_A) diagram. Points colored according to the water mass definition of Hernández-Guerra et al. (2019). Orange dots = South Atlantic Central Water (SACW); pink dots = Antarctic Intermediate water (AAIW); grey dots = Upper Circumpolar Deep Water (UCDW); blue dots = North Atlantic Deep Water (NADW); dark blue dots = Antarctic Bottom Water (AABW). Labeled dotted lines = potential density anomaly surfaces.

3.2. Data and Methods

3.2.1. Seismic Data and Processing

This research uses seismic reflection data collected during the Crustal Reflectivity Experiment Southern Transect (CREST) experiment aboard the R/V Marcus G. Langseth (Estep et al., 2019). The primary goal of the CREST survey was to investigate the evolution of oceanic crust at 30° S, and it spans the eastern edge of the RGR to the MAR, including a ~1600 km-long continuous east-west data transect. The transect sits at the center of the South Atlantic subtropical gyre, and provides an opportunity to investigate

the change of mesoscale mixing processes along a significant distance in a region that contains the returning limb of the Atlantic meridional overturning circulation (Cabré et al., 2019).

Seismic data were collected between January and February of 2016. The acoustic source was a 36-bolt air-gun array with a total volume of 6600 in^3 and 37.5 m shot spacing. Acoustic records were collected using a 12.6 km acoustically sensitive cable (i.e. streamer). The streamer contained 1008 hydrophones with 12.5 m spacing. This survey design collects repeat reflections from the same subsurface point (i.e. common mid-points, CMPs) every 6.25 m. To ensure the maximum depth of imaging to be more than 1000 m, while maintaining high signal-to-noise ratio for turbulence analysis, we used the first 400 near-source acoustic records.

Seismic data were processed with a standard, but adapted, processing sequence typically used to image the solid earth (Yilmaz, 2001): geometry definition, noise attenuation, CMP sorting, sound speed analysis, stacking, amplitude correction and migration (Fortin and Holbrook, 2009; Hobbs et al., 2009). Particular adaptations were made in the noise attenuation step to produce high quality image of oceanic fine structures. First, an eigenvector filter is applied to remove the direct waves that overprint the first 1s of data. Secondly, the relatively small shot spacing (37.5 m) generates reverberations between the sea surface and seafloor which share the same frequency range with primary signals. We filter out reverberations in the frequency-wavenumber domain based on the curvature differences between these coherent noises and primary signals in shot gathers. Thirdly, to reliably extract turbulent regimes from seismic data, random noise must be

attenuated, we follow the recommendations of Holbrook et al. (2013) by applying a 30-80 Hz band-pass filter. Lastly, shot-generated harmonic noise is suppressed by applying a notch filter centered at harmonic spikes (every 0.0267 cpm, cpm = cycles per meter) in the wavenumber domain (Holbrook et al., 2013). In addition, we implement a denoising convolutional neural network (DnCNN) to suppress random noise after stacking. We use the recommended steps and parameters of 17 layers and a mini-batch size of 128 (Zhang et al., 2017; Jun et al., 2020). We train the DnCNN model for 40 epochs and the number of iterations within each epoch is 220. After a series of noise attenuation, the signal-to-noise ratio of the entire seismic data increases by a factor of 6.

3.2.2. Diffusivity from Seismic Data

3.2.2.1. Background

Based on the assumption that seismic reflections are a reasonable approximation of isopycnal surfaces (Krahmann et al., 2009; Holbrook et al., 2013), studies have shown that turbulent diffusivity can be accurately measured from vertical displacement spectra of tracked reflections from both the internal wave subrange (Sheen et al., 2009; Dickinson et al., 2017) and turbulent subrange (Holbrook et al., 2013; Fortin et al., 2016; Mojica et al., 2018; Tang et al., 2020; Gunn et al., 2021). To clearly recognize the transition from internal wave regimes to turbulent regimes in log-log space, the vertical displacement spectra are multiplied by $(2\pi k_x)^2$ to produce the slope spectra. Here we estimate the turbulent dissipation rate ε through the slope spectra method in the turbulent subrange, φ_ζ^{Turb}, via a model proposed by Klymak and Moum (2007):

$$\varphi_{\zeta_x}^{Turb} = 4\pi \frac{\Gamma \varepsilon}{N^2} [C_T \varepsilon^{-\frac{1}{3}} (2\pi k_x)^{\frac{1}{3}}] \tag{1}$$

where $\Gamma = 0.2$ is the empirical mixing efficiency (Osborn and Cox, 1972), N is the horizontally averaged buoyancy frequency calculated from 22 historical CTD casts within the survey area (Figure 3.2C, black line), $C_T = 0.4$ is the Kolmogorov constant, and k_x is horizontal wavenumber. Equation (1) produces a turbulence subrange with a slope of $+1/3$ in log-log space. Diapycnal diffusivity, K, is then calculated using the Osborn relationship (Osborn, 1980):

$$K = \Gamma\varepsilon/N^2 \tag{2}$$

where ε is spectrally estimated from seismic data and varies as a function of distance along the section and depth.

To generate high-resolution maps of diffusivity across the entire seismic section, two complementary methods are used to calculate K. These methods allow us to extract turbulent information across a range of depths and scales, as they take advantage of both low and high amplitude reflectivity (Fortin et al., 2016).

3.2.2.2. Relative Turbulent Energy from Amplitude Spectra

First, amplitude spectra are calculated following Holbrook et al. (2013) through direct Fourier data transform. These spectra are calculated directly from seismic amplitudes (i.e. no tracking) along depth slices, and are first used to identify whether the turbulent subrange exists. For the CREST data, the turbulent subrange exists between k_x 0.025-0.045 cpm (22.2-40 m) (Figure 3.3B). The advantage of using amplitude spectra is reflected in its preservation of all horizontal wavenumbers, therefore relative turbulent energy from all reflections can be extracted. In other words, amplitude spectra can provide relative levels of turbulence across the entire seismic section. However, amplitude spectra

46

cannot provide absolute diffusivities because they are affected by the variation of seismic amplitudes, it is necessary to scale them with absolute diffusivities calculated from slope spectra of tracked reflections (hereafter, reflector slope spectra).

3.2.2.3. Absolute Diffusivities from Reflector Slope Spectra

Reflector slope spectra are calculated based on vertical displacement of undulating reflections that follows isopycnals, they are independent of seismic amplitude and thus can be used to estimate absolute diffusivity. We calculate reflector slope spectra using Fourier transform lengths of 256 points as recommended by Holbrook et al. (2013), equivalent to a reflection length of 1.6 km. Turbulent dissipation is then estimated by fitting reflector slope spectra to model (1) within the previously identified turbulent subrange (0.025-0.045 cpm) using least square inversion. Diffusivity is then calculated using equation (2) (Figure 3.3C).

Using reflector slope spectra also has its limitations. Tracked reflections, that yield slope spectra, must have high amplitude and good continuity, corresponding to the steepest temperature and salinity gradients (Ruddick et al., 2009). This limitation implies that absolute diffusivities cannot be estimated from weaker and discontinuous reflections that still possess turbulent information. Lower reflection amplitudes represent lower temperature and salinity gradients, corresponding to weaker stratification regions that prone to mixing. Discontinuous reflections could be caused by mixing instabilities such as interleaving, internal wave breaking, turbulence, and double diffusion (Tang et al., 2018). Therefore, a simple spatial smoothing of diffusivities calculated from stronger and continuous reflections over the entire seismic section could result in underestimation of

diffusivities in areas of weaker and discontinuous reflections. As discussed above, because amplitude spectra preserve all horizontal wavenumbers regardless of the strength of the reflections, we can overcome this limitation by joining and applying these two techniques in different window sizes to honor turbulent information in both types of reflections.
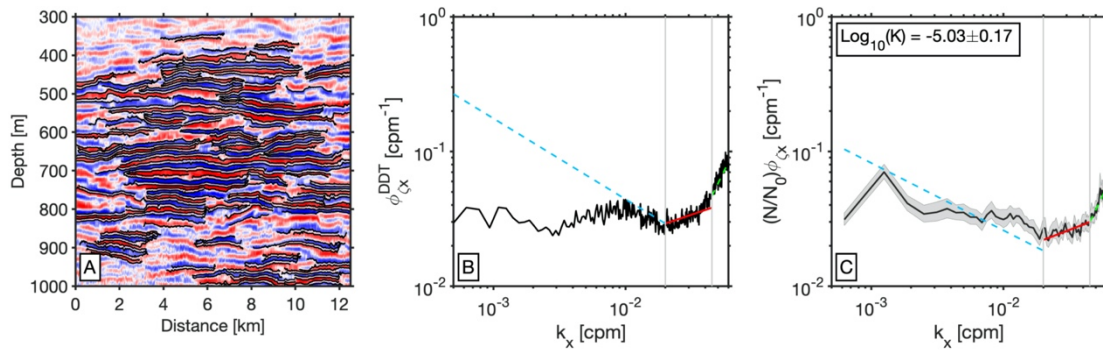
Figure 3.3: Example of spectral analysis from line1A (a rolling window used in section 3.2.2.5). (A) Seismic data overlapped with tracked reflections. Black lines = tracked reflections. (B) Direct data transform (DDT) of seismic data in (A). (C) Average slope spectrum calculated from all the tracked reflections in (A). Shaded gray area = 95% bootstrap confidence intervals. Dashed blue lines ($k^{-1/2}$), solid red lines ($k^{1/3}$) and dashed green lines (k^2) = the internal wave subrange , turbulence subrange and white noise respectively (Garrett and Munk, 1975; Klymak and Moum, 2007; Holbrook et al., 2013). Two vertical gray lines bound the turbulent subrange used to calculate diffusivity. The calculated diffusivity and its uncertainty are shown in the upper left corner.

3.2.2.4. Combining Amplitude and Reflector Slope Spectra

The seismic section is divided into regional windows of size 6.25 km wide and 50 m deep for reflector slope spectra analysis. The size of the window is chosen to include enough reflections to minimize artifacts and provide accurate estimations of absolute

diffusivities. An average reflector slope spectrum is calculated from all the tracked reflections within each regional window, and an absolute diffusivity is estimated for that window (Figure 3.3C). To complement the reflector slope spectra method, we calculate amplitude spectra in a much smaller window size of 400 m wide and 10 m deep. The window width is determined to include at least 10 horizontal wavelengths as calculated from the lower bound of the identified turbulent subrange (Fortin et al., 2017). Then, by integrating amplitude spectra energy over the turbulent subrange within each window, a map of relative turbulent energy across the entire seismic section can be obtained. Finally, relative turbulent energy is scaled by the absolute diffusivities within each regional window to produce the final high-resolution diffusivity map which has horizontal and vertical resolution of 400 m and 10 m, respectively. Fortin et al. (2016, 2017) have shown that this technique can reliably measure turbulent diffusivities from weaker reflections and seismically transparent zones where mixed water resides. Thus, these complementary techniques are able to produce high-resolution 2D maps of diffusivities. To avoid inaccurate estimation of diffusivity, seismic data shallower than 200 m are discarded because of the contamination caused by residual direct wave energy.

3.2.2.5. Depth- and Zonally-averaged Diffusivity

We investigate the distribution of thermocline diffusivities as functions of longitude and depth by taking appropriate means. So that seismic-derived diffusivities are comparable with lower resolution hydrographic data, we calculate depth-averaged, zonally varying diffusivities in rolling half overlapping windows. The window starts at the beginning of line1A to the end of line1F, covering a total length of 1625 km and has a

width of 12.5 km, with overlap of 6.25 km. The depth range of each window is 300 to 1000 m, for which the starting depth is chosen to match Argos and CTDs depth limitations. Within each window, depth-averaged diffusivity is estimated using the average reflector slope spectrum (e.g., Figure 3.3C), rather than the amplitude spectra. The average diffusivity within each window is assigned to the center longitude of that window. Ultimately, we obtain depth-averaged diffusivities that span longitudes 28.3° W to 12.4° W with a sampling interval of 6.25 km (Figure 3.6).

Zonal-averaged, depth-varying diffusivities are calculated based on their topographic setting. Each seismic section is divided vertically into 256 m half-overlapping windows and into regions above smooth and rough topography. Within each window, an average spectrum is calculated to estimate diffusivity. Diffusivities derived from different seismic sections are normalized by the lengths of the sections then horizontally averaged to produce a zonal-averaged, depth-varying diffusivities.

3.2.2.6. Error Analysis

Following Dickinson et al. (2020), we conservatively estimate an uncertainty for seismically-derived diffusivities as ± 0.4 logarithmic units. This value combines sampling and methodological errors. The sampling error mostly derives from the uncertainty in N, which we estimate as 0.28 cph using the standard deviation of CTD data. Methodological errors include the assumption of constant C_T and Γ and the process of fitting a straight-line model to reflector slope spectra. These uncertainties have been quantified by Dickinson et al. (2020), and are 0.25 log units. Combined in quadrature, the total uncertainty is ± 0.4 logarithmic units.

3.2.3. CTD- and Argo-derived Diffusivities

Diffusivities are estimated from CTD and Argo data and can be seen as representative of mean and spot measurements of mixing, respectively. We estimate diffusivities from five nearby Argos and 44 co-located CTDs (Figure 3.1). We use CTD datasets from two repeat surveys occupying GO-SHIP A10 transect in 2003 and 2011 at 30° S (Sloyan et al., 2019). Argos were collected around the same time as the seismic survey (data downloaded from Global Argo Data Repository). All of the Argo profiles used in this study record depths larger than 1000 m, and have vertical resolution less than 10 m. Argos b and e are ideally placed to provide spot measurements of mixing above smooth and rough topography conditions, respectively. Argo b was collected 176 km from the western end of line1A, above the RGR, and only two days before the start of seismic acquisition (Figure 3.1, green dot). Argo e travelled across the MAR during Jan 2016 and is used to compare with seismically-derived and depth-averaged diffusivities across the MAR (Figure 3.1, cyan dot). Although the Argo data are not co-located with the seismic survey, they provide meaningful measurements of the oceanic field above similar geological settings at two key locations.

From these hydrographic profiles, we computed potential density and buoyancy frequency. The selected profiles were then divided into 256 m half-overlapping segments. Following Kunze et al. (2006), the shallowest segment (0-256 m) is discarded due to the presence of sharp pycnoclines. For the remaining segments, we use a strain-based finescale parameterization to estimate ε (Kunze et al., 2006):

$$\varepsilon = \varepsilon_0 \frac{\overline{N^2}}{N_0^2} \frac{\langle \xi_z^2 \rangle^2}{\langle \xi_z^2 \rangle_{GM}^2} H(R_\omega) L(f, N) \tag{3}$$

$\varepsilon_0 = 6.73 \times 10^{-10}$ m^2 s^{-2}, $N_0 = 5.24 \times 10^{-3}$ rad s^{-1}, $\langle \xi_z^2 \rangle$ is the observed strain variance,

$\langle \xi_z^2 \rangle_{GM}^2$ is the strain variance from the Garrett-Munk model spectrum (Garrett and Munk,

1975). $\overline{N^2}$ is the vertically averaged buoyancy frequency for each segment, which is

estimated as linear fits to the specific volume anomaly depth profiles using the adiabatic

leveling method (Bray and Fofonoff, 1981). $H(R_\omega)$ is a function related to the shear-to-

strain ratio R_ω, which is set to 7 in this study (Kunze et al., 2006). $L(f, N)$ is a correction

for the effects of latitude (Gregg et al., 2003). Finally, the diffusivity is given by equation

(2).

3.3. Results

3.3.1. Thermocline Structure

The thermocline is visible as a 1000 m thick band of reflectivity that extends 1600

km across all seismic sections and is consistent with the regional temperature structure

(Figures 3.4 and 3.2A). Between 0 and 800-900 m depth, we observe stronger reflections

and weaker reflectivity at greater depths. This vertical distribution of reflection amplitude

corresponds to highly stratified SACW and weakly stratified AAIW, respectively (Figure

3.2). At 800-900 m depth, weakening reflection amplitude shows zonal variability

indicating that the depth of the SACW/AAIW boundary shoals eastward by 100 m (Figure
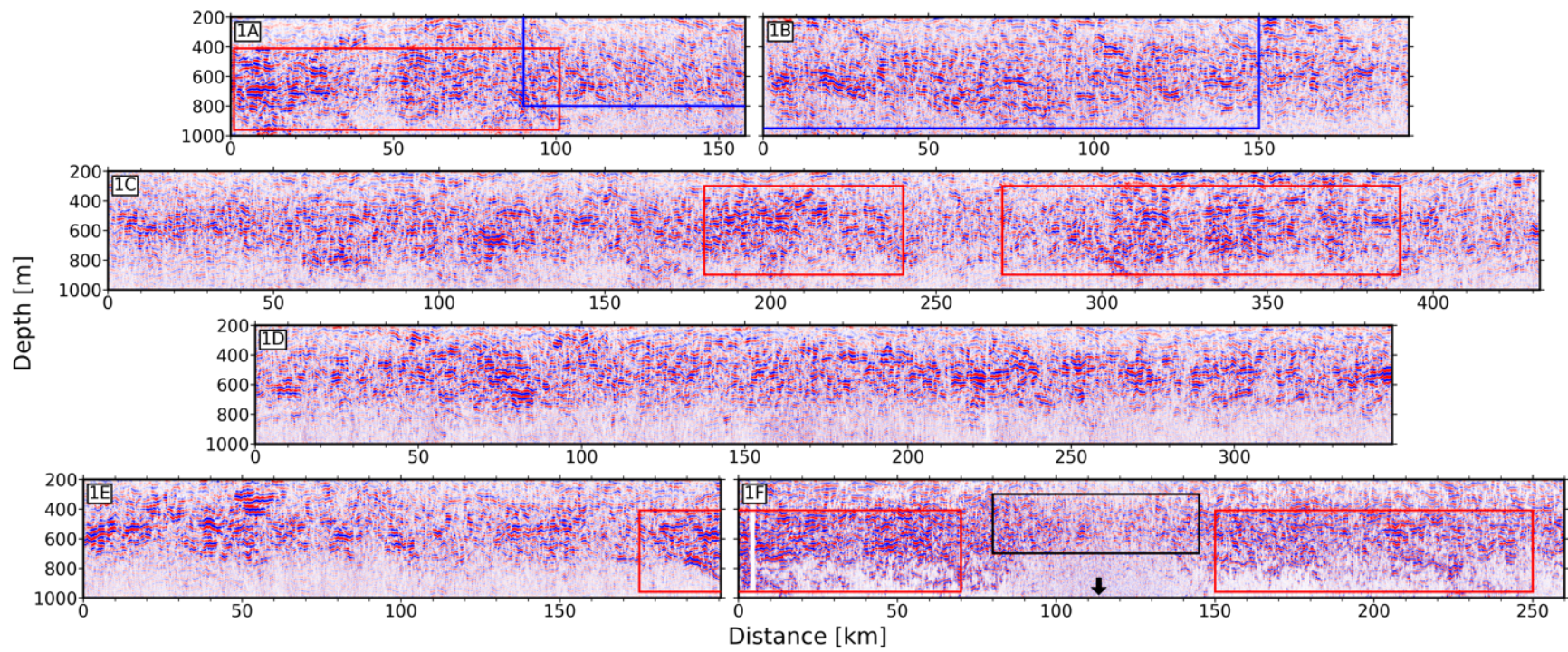
3.4, 1A).

Figure 3.4: Seismic sections from west (line1A) to east (line1F). Red boxes = locations of continuous, high amplitude reflections; blue boxes = an example location of shorter, discontinuous reflections; black box = the water mass above the MAR. Black arrow points at the location of the crest of the MAR.

Within the thermocline, reflectivity vary greatly in the lateral direction, changing from longer, higher amplitude to, shorter, lower amplitude and more disrupted reflectivity. Mesoscale patches of high-amplitude and more continuous reflectivity suggest the presence of eddy-scale processes, these patches extend to depths of 900 m and across 10's of kilometers zonally (Figure 3.4 red boxes). Between 90 km and 150 km (Figure 3.4, blue boxes), a set of shorter, discontinuous reflections dip to the east which we interpret as a shear event typical of the region. We do not observe submesoscale structures here, although these are often found in more energetic ocean environments such as boundary currents.

Above the MAR, reflections are clearly disrupted. In line1F from 80 to 150 km weaker discontinuous reflections can only be seen from the surface down to 700 m (Figure 3.4, black box and arrow). This anomalous patch of low reflectivity extends approximately 30 km either side of the ridge. Data below 700 m are severely contaminated by noise that has been diffracted by the hard igneous seafloor of this mid-ocean ridge and is too complicated to be sufficiently removed using noise attenuation.

3.3.2. Seismically-derived Turbulent Diffusivity Map

Across the 1600 km section of the central South Atlantic thermocline, the mean seismic-derived diffusivity is 3.96×10^{-5} m^2 s^{-1}(Figure 3.5). The value is similar to the microstructure observations made almost 20 years earlier in the Brazil Basin at longitudes of 28° W to 16° W (Polzin et al., 1997). The authors found a mean diffusivity of $1\text{-}5 \times 10^{-5}$ m^2 s^{-1} in the upper 1000 m of the water column. These seismic-derived (2016) and microstructure (1996) values are also consistent with CTD-derived diffusivities, that can

be seen as representative of means for 2003 and 2011. The mean CTD estimates for 2003 and 2011 are 7.45×10^{-5} $m^2\,s^{-1}$ and 4.15×10^{-5} $m^2\,s^{-1}$, respectively. The 2003 estimate is biased high by an anomalously elevated diffusivity around 13.5° W (Figure 3.6, green line). When this point is removed, the mean decreases to 3.57×10^{-5} $m^2\,s^{-1}$ which is remarkably consistent with the 2011 measurement and the mean seismic-derived diffusivity.

The spatial standard deviation of the seismic estimates is of a similar magnitude, 2.9×10^{-5} $m^2\,s^{-1}$, to the mean revealing the heterogeneity of the thermocline diffusivities. Variability is clearly related to variations in the thermocline structure, as we observe a strong correlation between seismic reflection amplitudes (i.e. strength of stratification) and corresponding diffusivity maps. Weaker and discontinuous reflections are found to have an average diffusivity of 4.79×10^{-5} $m^2\,s^{-1}$, a factor of four greater than locations dominated by stronger and more continuous reflections that have a mean value of 1.2×10^{-5} $m^2\,s^{-1}$. This spatial correlation is most apparent in line1A and line1B. From the beginning of line1A to about 90 km (Figure 3.4, 1A red box), where seismic reflections appear to be stronger and laterally continuous, the corresponding diffusivity map shows low diffusivities close to the canonical value of 1×10^{-5} $m^2\,s^{-1}$ (Figure 3.5, 1A red box). However, starting at 100 km and moving eastward into line1B, the strength of seismic reflections diminish as they become discontinuous (Figure 3.4, 1A, 1B blue boxes), whilst diffusivities start to increase to the level of 10×10^{-5} $m^2\,s^{-1}$ from shallower water (~250 m) into deeper water (~900 m). In line1B, at about 120 km, diffusivities start to gradually increase from deeper water (~800 m) to shallower water (~300 m), and eventually form a

bowl-shape region populated by diffusivity hotspots across line1A and 1B (Figure 3.5, 1A, 1B blue boxes). Similar correlation patterns between the seismic images and diffusivity maps can also be observed in all remaining profiles.

Taken as a whole, there are identifiable mesoscale patterns in the diffusivity. In areas that show elevated diffusivities, diffusivity hotspots of 7.5-10 $\times$ 10^{-5} m^2 s^{-1} largely dominate, while scattered higher diffusivities of 20-50 $\times$ 10^{-5} m^2 s^{-1} also exist. These hotspots are mostly located in the upper 600 m, with an exception in line1B from 50 to 100 km where they spread deeper than 800 m. In lower diffusivity regions, we see the canonical background value of 1 $\times$ 10^{-5} m^2 s^{-1} that mostly resides in the mid-depth from 400 to 800 m; diffusivities are slightly higher outside of this depth range.

Above the MAR, we observe the highest diffusivities of 25-50 $\times$ 10^{-5} m^2 s^{-1} that are densely distributed from 80 km to 150 km within the 300 to 700 m depth range (Figure 3.5, 1F). These estimates show that diffusivities are enhanced by an order of magnitude compared with background values. No reflections were tracked below 700 m because of severe noise contamination, which hinders our ability to reliably calculate diffusivities at deeper depths (Figures 3.4 and 3.5, 1F). Nevertheless, the signal-to-noise ratio for the 300-700 m depth range is high enough for diffusivity estimation. Away from the ridge crest, diffusivities rapidly decay to about 1 $\times$ 10^{-5} m^2 s^{-1} within ~30 km.
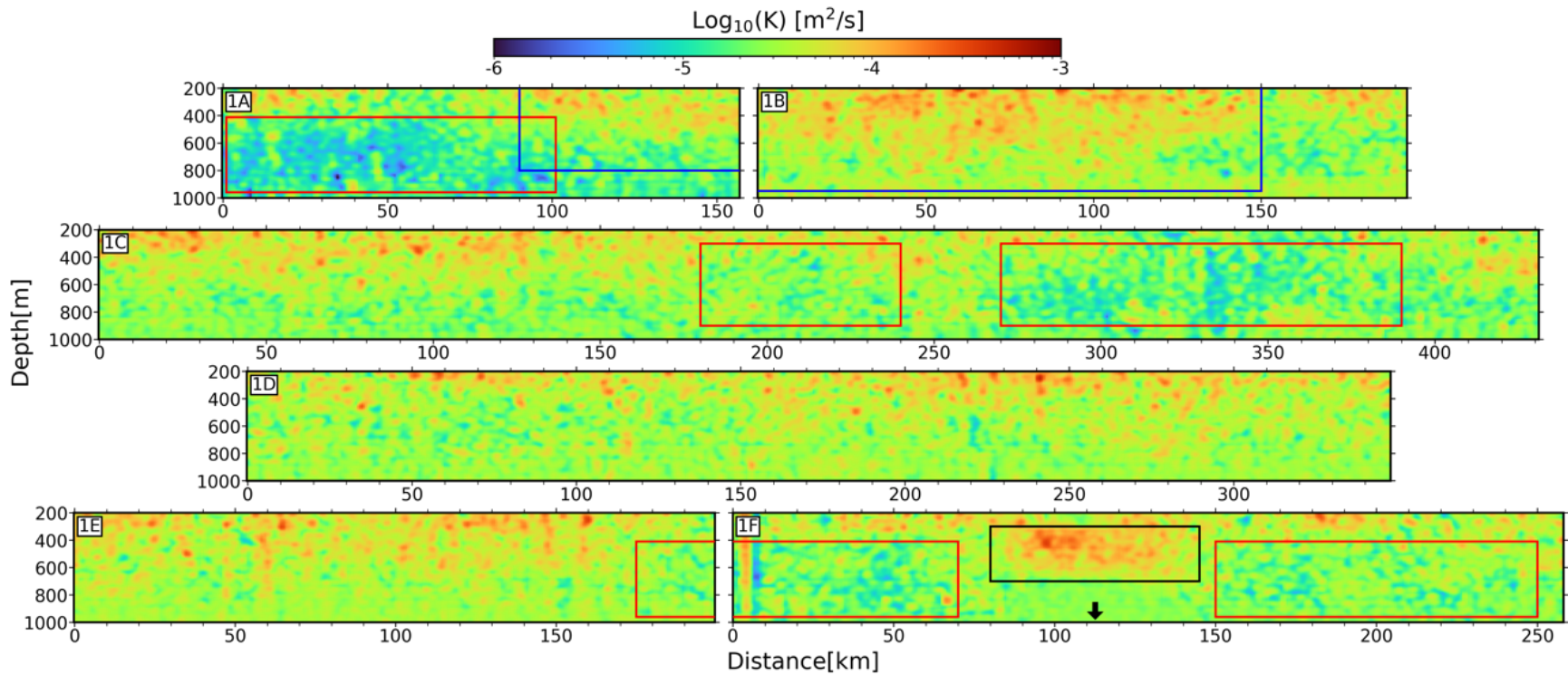
Figure 3.5: Turbulent diffusivity maps derived from seismic sections in Figure 3.4. Red boxes = locations of lower diffusivities; blue boxes = an example location of enhanced mixing; black box = enhanced mixing above the MAR. Black arrow points at the location of the crest of the MAR. Colored boxes same as in Figure 3.4.

3.3.3. Zonal Variability of Diffusivities

Depth-averaged diffusivities reveal zonal variability in thermocline diffusivity, which is heterogenous of mesoscale length scales. Depth-averaged diffusivities vary from 0.9×10^{-5} to 12.6×10^{-5} m^2 s^{-1}, with the highest diffusivity above the MAR. Around 26° W, there is a second region of elevated diffusivity of 6.5×10^{-5} m^2 s^{-1}. Diffusivities are lowest in the west at approximately 1×10^{-5} m^2 s^{-1}. These depth-averaged diffusivities serve as an instantaneous snapshot of mixing during February 2016. They reveal that there is no zonal trend in diffusivities, rather diffusivities are enhanced in localized patches.

We now compare seismic-derived diffusivities to hydrographic-derived and depth-averaged diffusivities. CTD-derived and depth-averaged (mean taken over 300-1000 m) diffusivities that vary with longitude range between 0.6×10^{-5} m^2 s^{-1} and 85×10^{-5} m^2 s^{-1}(GO-SHIP 2003, 2011; Figure 3.6, green and yellow line). The CTD estimates increase by one order of magnitude at the MAR. Two Argo profiles above smooth and rough topographic conditions serve as spot measurements of turbulence tuned to differing bathymetric conditions (Figure 3.6, magenta squares). The diffusivity calculated from Argo b (smooth) is 0.5×10^{-5} m^2 s^{-1}, it has a similar magnitude to the western end of line1A, which has a seismic-derived diffusivity of 0.9×10^{-5} m^2 s^{-1}. Diffusivities above the rough topography of the MAR calculated from Argo e (37×10^{-5} m^2 s^{-1}) and seismic (12×10^{-5} m^2 s^{-1}) are both one order of magnitude higher than over smooth topography and are within error of each other (Figure 3.6).
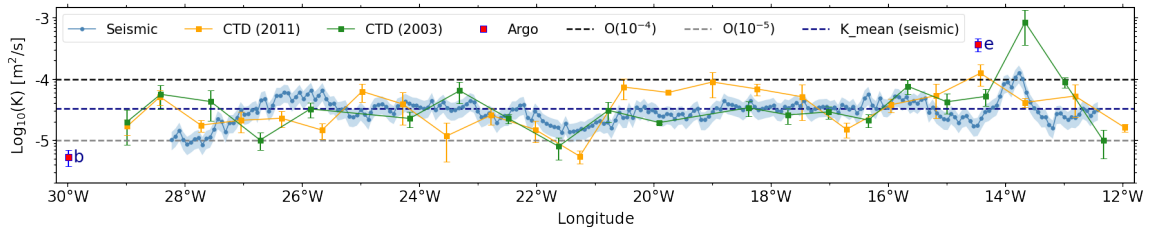
Figure 3.6: Depth-averaged diffusivities derived from seismic and CTDs in the zonal direction, plotted with depth-averaged diffusivities calculated from two Argo profiles (Green and cyan dots in Figure 3.1). Blue shade represents uncertainties of seismic estimates discussed in section 3.2.2.6. Error bars show the standard error of depth-averaged diffusivity of CTD/Argo profiles.

3.3.4. Depth Variability of Diffusivities Over Different Topographic Settings

Zonally-averaged diffusivities reveal the depth response of thermocline diffusivities over smooth (Figure 3.7, A-C) and rough (Figure 3.7, D-F) topographic settings. Above smooth topography, diffusivities are fairly constant with depth and are typically 1×10^{-5} m^2 s^{-1}. There is little difference between the seismic- and CTD-derived diffusivities here. Above rough topography, diffusivities are enhanced everywhere in the upper 700 m, and are 5.5×10^{-5} m^2 s^{-1} for seismic-derived estimates and 2.7×10^{-5} m^2 s^{-1} to 17×10^{-5} m^2 s^{-1} for CTD-derived estimates (Figure 3.7D and E). Below 700 m, seismic data cannot reliably recover diffusivities because of noise contamination and the CTD data are used to fill this gap. The deep CTD-derived estimates show a sharp increase from 600 to 1000 m (Figure 3.7D). We find that, at 30° S in the South Atlantic Ocean, diffusivities across the entire thermocline (up to 1000 m depth) are modified by the presence, or lack of, rough topography (e.g. compare Figure 3.7, C and F).

59
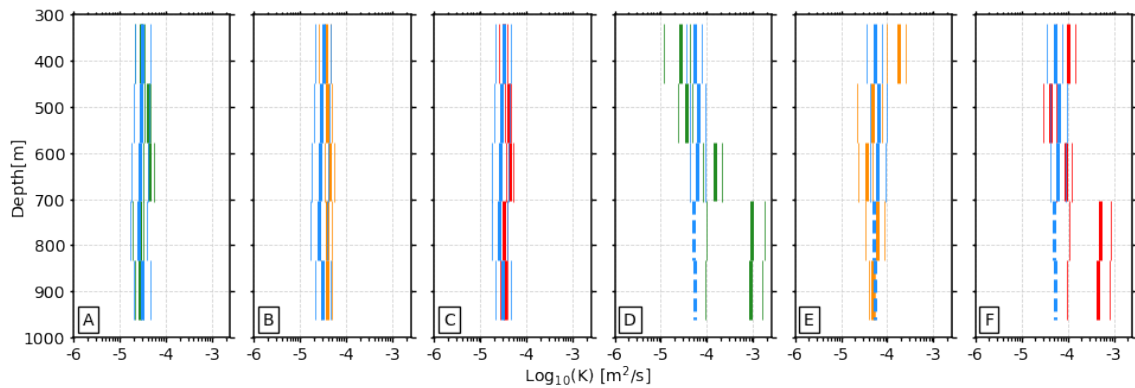
Figure 3.7: Zonally averaged diffusivities from seismic and CTDs above different topographic conditions. (A-C) Averaged vertical profiles of diffusivity above smooth topography (data from seismic line1A-E and CTDs west of 15° W). Thick blue bars, green bars, orange bars = averaged vertical profiles derived from seismic, GO-SHIP CTD 2003, and 2011, respectively. Red bars = averaged vertical profiles derived from both GO-SHIP 2003 and 2011. Thin bars represent standard errors between CTD profiles or seismic sections. (D-F) Same to (A-C) but above the MAR (data from seismic line1F and the three eastern most CTDs from GO-SHIP 2003 and 2011). Dashed blue lines represent unreliable diffusivities calculated from regions contaminated by noise.

3.4. Discussion

Here, we extend the observational record of ocean interior diapycnal mixing in the central South Atlantic, and, for the first time, we resolve diffusivities at mesoscale lengths for this location. High-resolution seismic diffusivity maps provide an unprecedented view of the variability of diapycnal mixing across 1600 km of the thermocline. By combining high-resolution seismic-derived diffusivities with low spatial resolution CTD-derived and low temporal resolution Argo-derived diffusivities, we can assess the likely drivers of mixing in this location.

3.4.1. Temporal and Spatial Variability of South Atlantic Thermocline Diffusivities

At synoptic (~1000 km) and decadal scales, the background diffusivity of the South Atlantic thermocline has changed little at this location. In 1996, direct turbulent diffusivities measurements across the Brazil Basin revealed that the upper 1000 m of the South Atlantic typically had diffusivities of around $1\text{-}4 \times 10^{-5}$ $m^2 s^{-1}$ (Polzin et al., 1997). CTD-derived mixing estimates from 2003 and 2011 also show a mean diffusivity of 3-4 $\times 10^{-5}$ $m^2 s^{-1}$. Whilst, seismic data collected in 2016 show a similar mean diffusivity in the upper 1000 m of 4×10^{-5} $m^2 s^{-1}$. Taken together, these four decadal snapshots (1996, 2003, 2011, and 2016) suggest that there is little variability in the mean diffusivity of the thermocline. Using a global coupled climate model, Hieronymus et al. (2019) found that oceanic background diffusivity has a significant impact on the climate. They found that increased background diffusivity leads to increased meridional heat transport and stronger overturning in the ocean. Our observations suggest that on decadal time-scales the mean

61

thermocline diffusivity has changed little in this location, which implies steady meridional overturning circulation in the South Atlantic thermocline.

Imprinted upon the background diffusivity, we show that diffusivities are heterogeneous and can be enhanced by up to one order of magnitude. Regions of high mixing correspond to seismic transparent zones or disrupted reflections. The correlation between seismic reflectivity and turbulent mixing is typical of seismic oceanography studies (Dickinson et al., 2017; Fortin et al., 2017; Tang et al., 2021) and these observations have shown that higher reflectivity is caused by sharper temperature and salinity gradients, hence stronger stratification, while lower reflectivity represents weaker stratification that facilitates mixing or homogeneous water masses. Weakened reflectivity above the MAR corresponds to enhanced mixing and weaker stratification (Figure 3.4, black box). Seismic-derived, CTD-derived, and Argo-derived diffusivities are all enhanced by an order of magnitude. This result is consistent with lower resolution diffusivity measurements made by Polzin et al. (1997), who showed that diffusivities exceed 1×10^{-5} m^2s^{-1} in the thermocline above the ridge. Whilst, depth-averaged N shows stronger stratification (2.13 cph) above smooth plains compared to weaker stratification (2.01 cph) above the MAR (Figure 3.2C). The high-resolution and depth coverage of the seismic data also reveals that mixing across the entire thermocline (200-1000 m) are enhanced within 30 km of the ridge. Away from the ridge, several other patches of high-diffusivity are observed that also correspond with low amplitude and disrupted reflectivity.

The spatial heterogeneity of mixing suggest that the mid-ocean thermocline is not quiescent. Enhanced mixing in the ocean interior is primarily caused by breaking of

internal waves (Gregg et al., 2003) for which the energy input generally comes from tidal flows impinging upon topography (Munk and Wunsch, 1998) and wind forced near-inertial waves below the mixed layer (D'Asaro, 1985; Alford, 2003b). We discuss the possible drivers of observed enhanced mixing below.

3.4.2. Drivers of Enhanced South Atlantic Thermocline Diffusivities

3.4.2.1. Rough Topography at the Mid-Atlantic Ridge

Enhanced mixing in the thermocline above the MAR are most likely driven by barotropic tides impinging on the rough bathymetry of the ridge. Due to a lack of observations, the effect of the MAR on upper water column (<1000 m) mixing has been less clear than its effect on abyssal water. Here, both seismic-derived and hydrographic-derived estimates of K show that diffusivities across the entire water column are enhanced by at least one order of magnitude compared with background values. These rates are consistent with shallow microstructure observations above mid-ocean ridges (Polzin et al., 1997; Mauritzen et al., 2002; St Laurent and Thurnherr, 2007) and recent work by Li and Xu (2014) who found the influence of rough topography on turbulent mixing can extend 3300 m upward into the ocean interior. Seismic estimates (limited to 700 m) show larger diffusivities at shallow depths (Figure 3.5, 1F), whilst microstructure measurements show that diffusivities increase significantly below 700 m depth, as found by Polzin et al. (1997). Therefore, it is also possible that an upward source or mesoscale oceanic process is ehancing the shallow mixing further and is only capture by the high-resolution siemsic data. Due to the presence of the ridge and consistency of these high diffusivities over time,

we conclude that at 30° S, the MAR enhances diffusivities across the entire water column by at least one order of magnitude.

The rapid decay of diffusivities within ~30 km away from the MAR is shorter than similar decays of ~60 km at the Hawaiian Ridge and the Mariana Ridge (Klymak et al., 2006; Tang et al., 2021). This discrepancy indicates that at the Hawaiian Ridge and the Mariana Ridge, a large portion of tidal energy radiates away, while at the MAR, a significant portion of tidal energy is dissipated locally, which is consistent with previous interpretations (Waterhouse et al., 2014).

3.4.2.2. Storm and Eddy

The causes of enhanced mixing over smooth topography are less clear. Irregular patches of enhanced mixing in these seismic lines could be caused by a variety of mechanisms, such as dissipation of high-mode near-inertial energy, breaking of low-mode tidal or near-inertial waves through wave-wave interactions, and energy dissipation through mesoscale eddy fields (MacKinnon et al., 2013). Numerical studies predict enhanced mixing caused by dissipation of semidiurnal tides near latitudes of 29° N/S (MacKinnon and Winters, 2005; Simmons, 2008).

Of these mechanisms, wind-induced mixing is the most pervasive globally (Alford et al., 2016). Winds inject energy into the ocean through wind stress impulses such as traveling midlatitude storms. These storms can excite frequency response in the near-inertial band and generate near-inertial internal waves (Pollard, 1970; Gill, 1984; Alford et al., 2016). Horizontal convergence and divergence of the ocean's mixed layer water can provide pathways for wind injected energy to propagate downward and eventually

generate near-inertial waves in the stratified water below (D'Asaro, 1985; D'Asaro et al., 1995; Young and Jelloul, 1997). Much of the energy exerted by winds goes into low-mode near-inertial waves that propagate for great distances (D'Asaro et al., 1995; Alford, 2003b), while the remaining portion oscillates as high-mode near-inertial waves that promote mixing because of their potential for higher shear (Alford and Gregg, 2001; Alford, 2010). Thus, in our study, enhanced mixing over smooth topography may reveal the energy cascading process of high-mode near-inertial waves breaking into small scale turbulence during downward propagation. In addition, using Lagrangian observations, Chaigneau et al. (2008) showed that winds inject near-inertial energy into the mixed layer in the subtropical South Atlantic. Given this knowledge and our observations of mixing hotspots are mostly above 600 m depth, we hypothesize that the observed enhanced mixing above smooth topography is wind-induced and modified by mesoscale currents in the mixed layer. We explore this hypothesis by analyzing wind stress data and sea-surface geostrophic currents.

3.4.2.2.1. Spatial and Temporal Variability of Wind Stress

We now assess the likelihood of a storms driving unusually elevated diffusivities in the mid-ocean. Since rays of near-inertial waves propagate horizontally as well as downward, the location of wind energy input may not be the same as enhanced mixing. Theoretical modeling suggests that at 30° S, near-inertial waves travel ~330 km horizontally before reaching the seafloor (Garrett, 2001). Therefore, we evaluate if strong winds were present prior to and within ± 3 degree (in both zonal and meridional directions) of the seismic survey. 6 hourly wind speed data from the NCEP reanalysis 2 (Kanamitsu

et al., 2002) is converted to wind stress using the method of Large and Pond (1981). Wind stress is then averaged within the geographic boundary of 33° W, 9° W, 27° S, 33° S for 60 days before the survey (Figure 3.8). This time span of 60 days is chosen given a near-inertial wave propagating vertically to 800 m depth with a speed of 13 m day^{-1}. The depth limit of 800 m is determined from the maximum depth of enhanced mixing observed in profile line1B (Figure 3.5, 1B). 13 m day^{-1} is chosen to approximate the mean downward propagation speed for near-inertial waves, and is based on a 2-yr record of acoustic Doppler current profilers (Alford et al., 2012). Given these time and space limits, we now investigate the temporal and spatial variability of wind around the seismic survey and its relation to enhanced mixing above smooth topography.

Over the 60-day period before the seismic survey, wind stresses greater than 8 standard deviations from the mean occur about 30 days prior to the survey between January 01 and January 08, 2016 (Figure 3.8A, upper panel). We interpret this high wind stress event as a storm. After linearly interpolate the wind stress on hourly time grid, we use a Butterworth bandpass filter to extract the wind stress in the near-inertial band of $0.8f$-$1.2f$, where f is the Coriolis frequency. Slight changes of lower and upper bounds of the near-inertial band do not significantly affect the results of this analysis. The storm shows substantial increase in strength within the near-inertial band compare to the rest of the 60-day period (Figure 3.8A, lower panel), which indicates the important role of this storm in injecting near-inertial energy into the ocean interior.

We spatially track the storm across the seismic survey location by calculating average wind stress along 30° S with a series of rolling windows. Each window has size

4°×4° and is centered every 2° from 30° W to 12° W (Figure 3.8, B-K). The movement of the storm correlates with the zonal trends of diffusivities. First, higher wind stresses with higher strength in the near-inertial band are shown from 32° W to 14° W during the time of the storm (Figure 3.8, B-I), consistent with the locations of enhanced mixing in seismic derived diffusivity sections (Figure 3.5, 1A-1E). Second, the far eastern end of the seismic survey that is above the MAR (15° W to 12° W) did not experience wind forcing as high as regions further west (Figure 3.8, J-K). Correspondingly, we observe lower diffusivities at this location (Figure 3.5, from the eastern end of line1E to line1F). We note that weaker wind forcing and lower diffusivities at both sides of the MAR provide additional support to our interpretation above - enhanced mixing directly above the MAR is caused by rough topography. The enhanced mixing on lines 1A-1E is likely caused by this storm for three reasons: (i) there were no other wind stress peaks within the relevant time range, (ii) enhanced diffusivities track the movement of the storm, and (iii) this region is away from topographic boundaries.
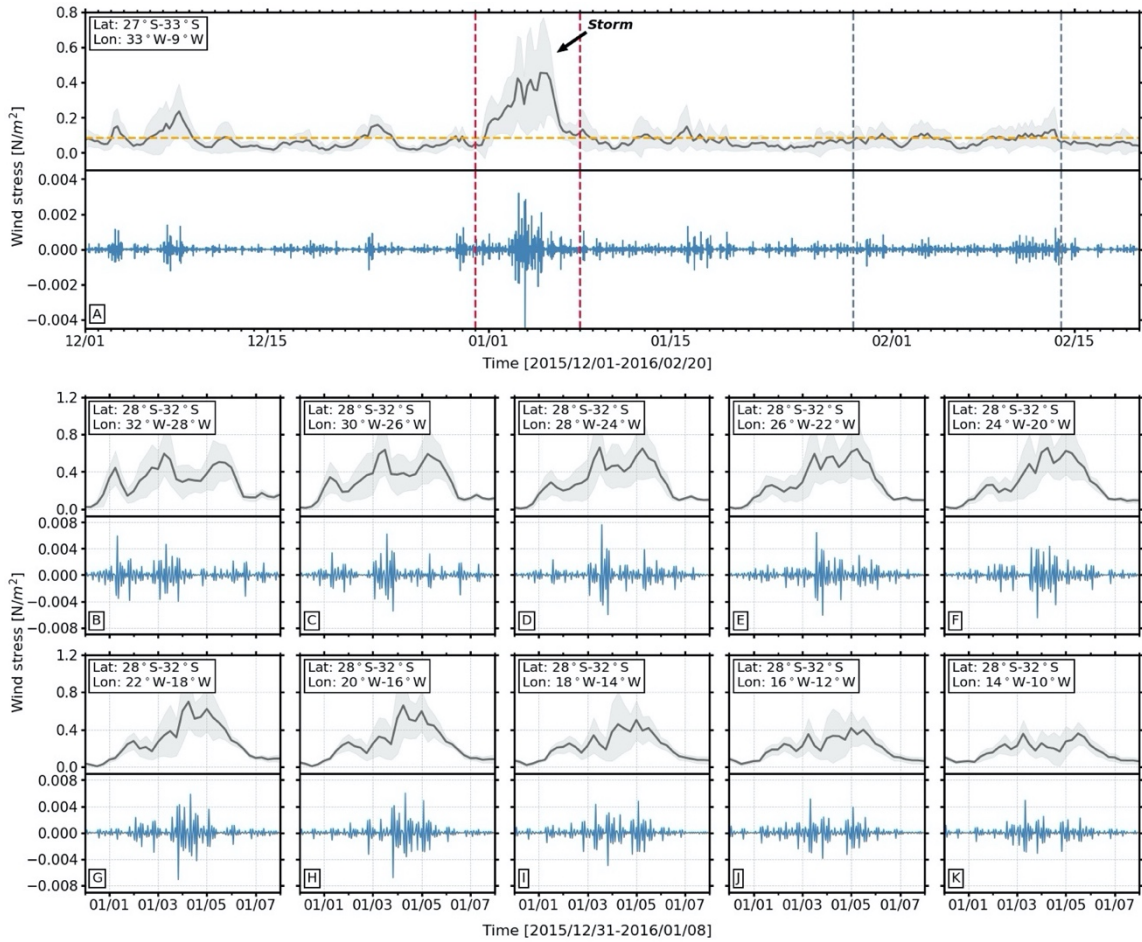
Figure 3.8: Wind stress variability in time and space. (A) Spatially averaged wind stress as a function of time for region 33° W, 9° W, 27° S, 33° S (upper panel) and its corresponding bandpass filtered near-inertial wind stress (lower panel). Black line = averaged wind stress; blue line = near-inertial wind stress; horizontal dash yellow line = average wind stress for the entire time period. Light grey shade represents standard deviation of measurements. Vertical red dashed lines bound the time of high wind stress that are analyzed individually as a function of space from (B) to (K). Vertical grey dashed lines bound the days of the seismic survey. (B-K) Same as (A) but for averaged wind stress during the storm analyzed in a series of spatially overlapping windows described in the text. The region of each window is shown in the box at upper right corner of each figure. The black arrow points to the feature that we interpreted as a storm because its wind stress is greater than 8 standard deviations from the mean. Wind stress data are from NCEP reanalysis 2 (Kanamitsu et al., 2002).

68

Argo-derived diffusivities support our hypothesis of storm induced mixing (Figures 3.1 and 3.9). Argos a, b, c, d were selected because they are within the region of the storm during the time span of the analysis. All Argos show enhanced mixing over depth range of 300-600 m after wind forcing (Figure 3.9, red shading), although the timing and strength of these changes varies substantially. Argo a experienced a relatively high level of mixing throughout the time of our analysis. The reason of higher diffusivity of 8.1 $\times$ 10^{-5} $m^2 s^{-1}$ before the storm is unknown, however, there is a noticeable increase of mixing from 3.9×10^{-5} $m^2 s^{-1}$ to 9.9×10^{-5} $m^2 s^{-1}$ after the storm around Jan-15, then diffusivities maintained above the level of 5.2×10^{-5} $m^2 s^{-1}$. Argo b shows enhanced mixing during and after the storm, diffusivities increased significantly from 2.4×10^{-5} $m^2 s^{-1}$ to 23×10^{-5} m^2 s^{-1} in the time of Dec-26 to Jan-15. Argo c and d show enhanced mixing during the storm but diffusivities decrease immediately afterwards. We also notice significant increase of diffusivities in Argo a, b and c about 50, 60, and 30 days after the storm, respectively, while there was no apparent increase in wind stress during these periods of times (Figure 3.8A). There are two possible reasons for the differences. The first is out of plane effects and the second is local mesoscale flows. Whilst we analyze the diffusivities as a function of time, Argo floats change their spatial location. All floats traveled about 100 km during the time span of analysis (Figure 3.10). Their Lagrangian behavior means that the diffusivities in Figure 3.9 do not reflect changes in time at a fixed location. Therefore, other oceanic processes may affect the recovered diffusivities. For example, energy from other events such as wave-wave interactions and near-inertial waves propagating in from elsewhere can have effects on the observed mixing pattern (Plueddemann and Farrar,

2006), which might also explain the spatial discrepancies between the mixing pattern and wind stress. However, it is beyond the scope of this contribution to account for out of plane influences.

On the other hand, local mesoscale processes may cause differences between the distribution of ocean mixing and the presence of wind stress at the sea-surface. For example, the presence, or lack thereof, of mesoscale eddies has been shown to play an important role in controlling downward propagation of near-inertial energy (Zhai et al., 2005), resulting in different speeds of downward propagation at different times and locations. From the seismic data, we use the different depths of enhanced mixing (Figure 3.5) and a period of 30 days to calculate the downward propagation speeds of near-inertial energy and find a large range of 17 to 27 m/day. Furthermore, mismatches between the patterns of wind stress and diffusivities suggest that local mesoscale flows are playing a role in distributing near-inertial energy. For example, the western end of the seismic survey (line1A) shows the lowest diffusivities while the wind stress was high (Figure 3.8B). Similarly, we observe diffusivities slightly higher than the background level between 22° W to 20° W (Figure 3.6), but the wind stress around this region shows sharp spikes in the near-inertial band (Figure 3.8, G-H). Since this region hosts an energetic eddy field, we now consider the possible impact of mesoscale eddies in the mixed layer on propagation of wind-induced near-inertial energy.
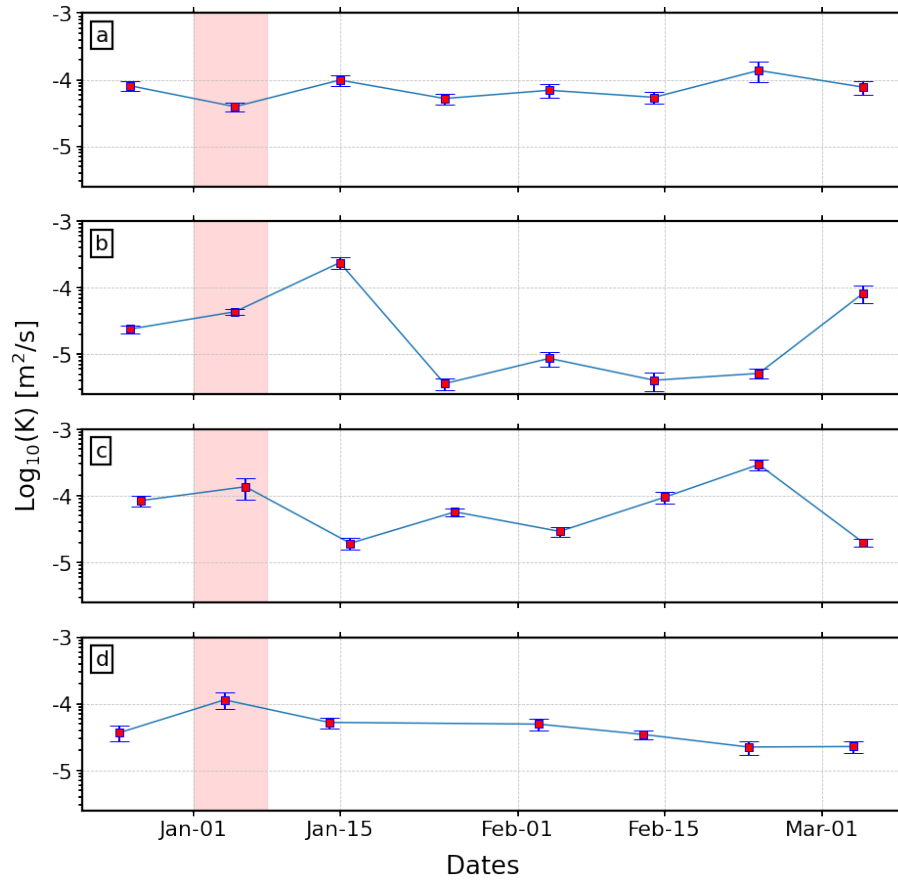
Figure 3.9: Depth (300-600 m) averaged diffusivity from Argo floats (a, b, c, d) as a function of time during and after the storm. Vertical red bands mark the time of the storm. Error bars represent standard errors.

3.4.2.2.2. Possible Contribution of Eddies

We use satellite observations of sea surface geostrophic current velocities to investigate mesoscale eddies in the mixed layer during the time of the storm. Figure 3.10 shows the evolution of sea surface geostrophic current velocities from January 03 2016 to February 14 2016, covering the time period from the start of the storm to the end of the seismic survey (each plot is separated by two weeks). An anticyclonic eddy, centered around 30° W, 31° S and identified by high velocities of ~0.35 m s^{-1}, is present during the

71

storm. The intensity of the eddy weakens as time goes by (Figure 3.10A-D). The eastern and western portions of seismic line1A and line1B, respectively, cross the easterly side of the eddy. Here, we observe enhanced mixing that propagates to depths greater than ~800 m in line1B (Figure 3.5, 1B). The convergence of high velocity currents at this location suggests more complex structures of mesoscale flows compared to other locations (Figure 3.10A), which could be an explanation for the deeper penetration of enhanced mixing in line1B. If we consider the eastern edge of the eddy as the input location of deep propagating energy, the location of the deepest penetration is at 50-100 km in line1B, implying near-inertial energy propagates both vertically and laterally. These findings are consistent with limited previous observations (Jing et al., 2011; Whalen et al., 2018) and numerical studies (Danioux et al., 2008) that reveal the importance of mesoscale eddies in draining energy to great depths. Taken together, these observations suggest that mesoscale eddies enhance the depth-penetration of wind-induced mixing from 600 to 800 meters.

To summarize, we hypothesize that wind generated near-inertial energy is a likely candidate for the enhanced mixing away from rough topography, with surface mesoscale flows playing an important role. The enhanced diffusivities we observe are higher than the background level by an order of magnitude in some cases. If our hypothesis of wind induced mixing holds true, given that the seismic survey was conducted in a non-stormy season, our results demonstrate that wind induced mixing plays an important role in the central South Atlantic thermocline mixing.

72
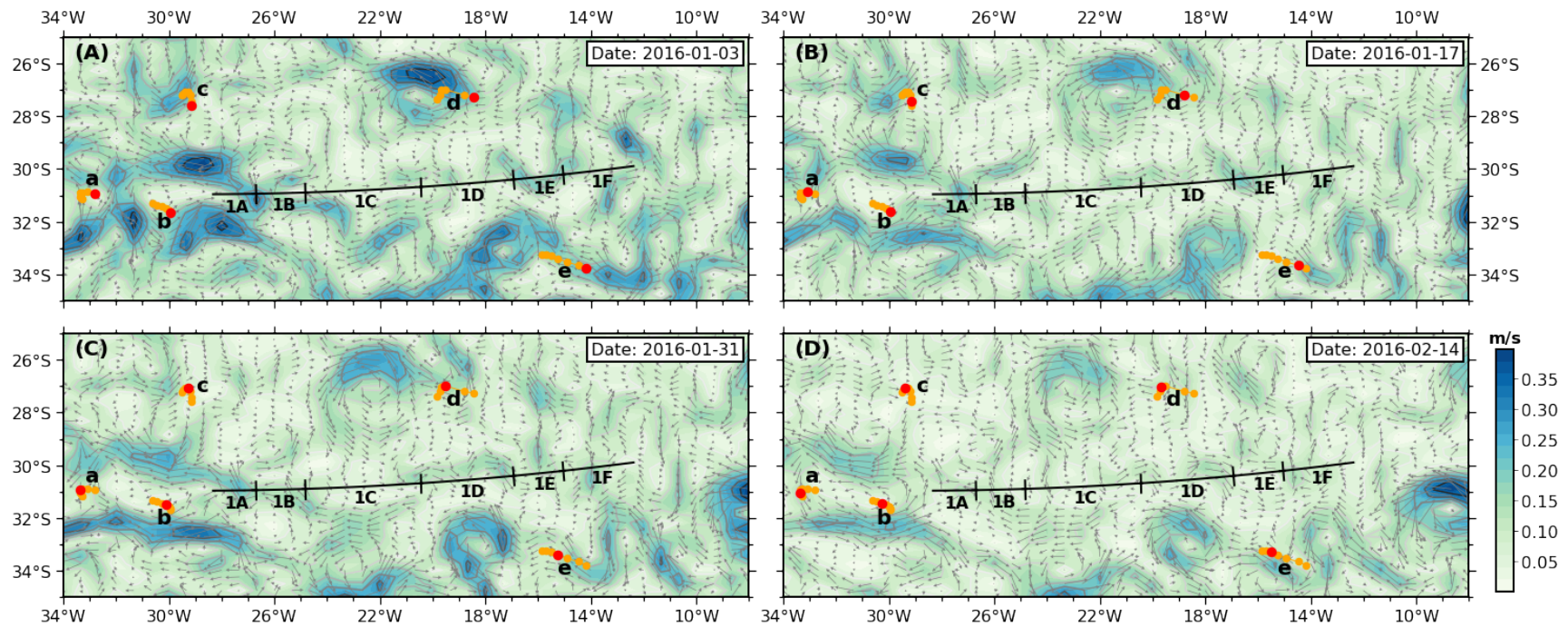
Figure 3.10: Maps of sea surface geostrophic current velocities. (A) Sea surface geostrophic current velocities calculated for 5 days composite centered on 2016/01/03 from Ocean Surface Current Analyses Real-time (OSCAR) satellite measurements. Black lines = seismic survey lines. Orange dots = the trajectory of the Argo floats shown in Figure 3.1. Red dots = the positions of the Argo floats closest to the date of the satellite measurements. (B-D) Same as (A) but separated two weeks apart following (A).

73

3.5. Conclusions

We map vertical diffusivities across 1600 km of the central South Atlantic thermocline using six seismic reflectivity sections, CTD, and Argo data. Seismic reflectivity yields continuous high-resolution diapycnal diffusivity maps of the thermocline during February 2016. These data help to overcome observational limitations since they yield full-thermocline vertical sections that have a horizontal extent of 1600 km length, vertical and horizontal resolution of $O(10)$ m, and that span a period of 4 weeks. Meanwhile, CTD data from 2003 and 2011 provide low spatial resolution diffusivity estimates that can be seen as representative of the time mean. Argo data provide spot measurements and Lagrangian tracers of mixing over different topographic settings and at different times. Together, these data extend the observational record of diapycnal mixing in the ocean interior, and provide insights into the variability and drivers of mixing.

The South Atlantic thermocline is seismically imaged as an 800-900 m band of reflectivity with no clear submesoscale patterns within it (Figure 3.4). Seismic-derived and CTD-derived diffusivities show that, in the mean, thermocline diffusivities have remained relatively consistent at close to or less than 1×10^{-5} m^2 s^{-1} since the 1990s (Figures 3.5, 3.6). We find low/high diffusivities over smooth/rough topography, and these values are particularly enhanced over the Mid-Atlantic Ridge (25-50 $\times$ 10^{-5} m^2 s^{-1}). Imprinted upon the synoptic scale mean, mixing is heterogeneous, showing enhanced diffusivities that exceed the background level of 1×10^{-5} m^2 s^{-1} in many regions where reflections are weaker and disrupted (Figures 3.5-3.7).

74

We examined the most likely drivers of mixing variability (Figures 3.8-3.10). Above the Mid-Atlantic Ridge, diffusivities are enhanced by barotropic tides impinging on the rough bathymetry of the ridge. The rapid decay of diffusivities within ~30 km away from the ridge implies local dissipation of tidal energy. Above smooth topography, we hypothesize that with limited hydrographic data, we cannot fully decipher what caused the enhanced mixing above smooth topography, however, our best assessment suggests it is likely caused by localized wind generated near-inertial energy (i.e. a storm). The dissipation of such energy during downward propagation resulted in elevated diffusivities ranging from 3×10^{-5} m^2 s^{-1} to 50×10^{-5} m^2 s^{-1}. The loci and depth of energy propagation varies substantially, possibly affected by the surface wind forcing and mesoscale flows in the mixed layer. The maximum depth of enhanced mixing is about 800 m, taking place close to the edge of an anticyclonic eddy, suggesting mesoscale eddies encourage deeper propagation of near-inertial energy.

The interaction between surface wind, mesoscale flows in the mixed layer, and high mode near-inertial waves is a complex process that remains poorly understood. It is beyond the scope of this study to fully explain the heterogeneity of mixing along the entire seismic survey with limited hydrographic measurements. However, high-resolution seismic observations along with concurrent hydrographic and wind measurements provide an opportunity to untangle these mechanisms. More simultaneous observations are needed in the vicinity of rough topography and strong storm forcing regions to improve our understanding of the global mixing budget and to contribute to more accurate ocean circulation and climate models.

4. DEEP PROPAGATION OF NEAR-INERTIAL ENERGY IN THE VICINITY OF AN ANTICYCLONIC EDDY

4.1. Introduction

The global overturning circulation is largely maintained by diapycnal mixing of shallow, lighter waters with deeper, denser waters through turbulence primarily driven by breaking of internal waves (Munk and Wunsch, 1998). A total amount of 1-2 TW of diapycnal mixing is needed to maintain the observed stratification (Wunsch and Ferrari, 2004). Ocean turbulence is measured by dissipation rate of turbulence kinetic energy, ε, that can be related to vertical eddy diffusivity K (Osborn, 1980). It is widely recognized that a global average K of 10^{-4} m^2s^{-1} is required to maintain the global overturning circulation, while 10^{-5} m^2s^{-1} is observed in the thermocline (Waterhouse et al., 2014). The mismatch suggests mixing hotspots are prevalent in the ocean where tides flow over rough topography (Polzin et al., 1997) and when strong wind forcing is applied to the ocean surface (D'Asaro, 1985). The energy supply into the internal wave continuum is estimated to be 0.7-1.3 TW for tidal flows over topography (Munk and Wunsch, 1998; Garrett and Kunze, 2007) and 0.3-1.5 TW for wind generated near-inertial waves (NIW) (Alford, 2003b; Plueddemann and Farrar, 2006). The uncertainties in quantifying the wind powered mixing is larger because wind forcing is intermittent which makes the observation of NIW more difficult than internal tides, so that remarkably little is known about their generation, evolution, or decay.

76

Existing studies concluded that much of the energy exerted by winds translates low-mode NIW that propagate for great distances (D'Asaro et al., 1995; Alford, 2003b), while the remaining energy oscillates as shear-containing high-modes NIW that provide a more direct pathway to mixing (Alford and Gregg, 2001; Alford, 2010). Mixing by high-mode NIW are likely dissipated locally in the upper ocean at generation sites and has a seasonal cycle coherent with wind forcing (Jing and Wu, 2010; Whalen et al., 2012). Alford and Whitmont (2007) found evidence of deep penetration of NIW that might contribute to abyssal mixing , however, the penetration depths have large uncertainties even for NIW induced by similar wind events, possibly caused by the influence of the mesoscale field (Alford et al., 2012). This leaves the question of how much of the wind work performed at the surface propagates into the ocean interior. The large variation of group velocities of high-mode NIW makes them interact strongly with ambient mesoscale fields (Elipot et al., 2010), however, the observation of this type of process is extremely rare and is limited by restricted sampling. Our limited understanding of NIW calls for more observations in order to better parameterize their influences in ocean circulation models.

The subtropical South Atlantic is a region of active near-inertial processes associated with mid-latitude storm activity (Chaigneau et al., 2008). Using seismic oceanography, Wei et al. (2022) observed enhanced mixing exceeding the background level by one magnitude in the upper 1000 m of the central South Atlantic induced by a storm ~30 days before the seismic data acquisition (Figure 4.1). The authors hypothesized that high-mode NIW play a major role in the observed mixing pattern and that the

mesoscale eddy contributes to deep penetration of enhanced mixing. This study is a follow-up of the contribution by Wei et al. (2022), aiming to provide more evidence for enhanced mixing caused by high-mode NIW and to emphasize the role of mesoscale eddy flow. Using multichannel seismic (MCS) data, we image the thermohaline fine structures in the South Atlantic subtropical gyre down to 1400 m along a zonal transect at 30° S (Figure 4.1), vertically covering three stably stratified westward transporting water masses (Schmid, 2014): South Atlantic Central Water, Antarctic Intermediate Water and Upper Circumpolar Deep Water. We extract high-resolution dynamical parameters of the oceanic volume that are difficult and expensive to obtain with conventional hydrographic measurements. This study extends the observation record of high-mode NIW and their interaction with mesoscale eddy flows by providing observations on unprecedented scales of tens of meters, contributing to the understanding of wind induced mixing in the South Atlantic.
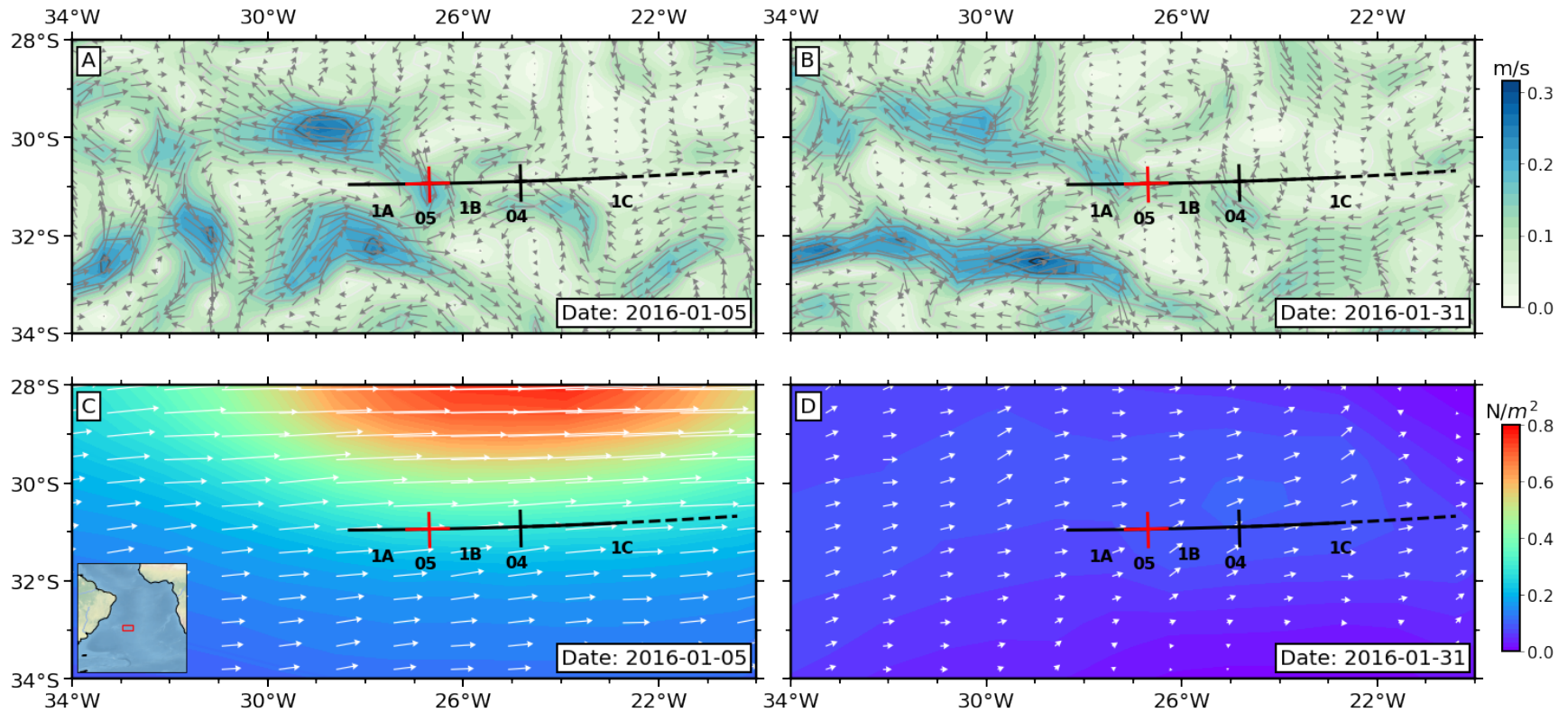
Figure 4.1: Maps of sea surface geostrophic current velocities and wind stress. (A-B) Sea surface geostrophic current velocities calculated for 5 days composite centered on 2016/01/05 and 2016/01/31, respectively, from Ocean Surface Current Analyses Real-time (OSCAR) satellite measurements. Black lines = seismic survey lines. Red crossing = seismic sections displayed in Figure 4.3. Dotted black line = the eastern half of line1C that is omitted in Figure 4.7. (C-D) Wind stress data on date 2016/01/05 and 2016/01/31, respectively, calculated from daily wind speed data from the NCEP reanalysis 2 (Kanamitsu et al., 2002), using method of Large and Pond (1981). Inset shows regional setting, with red box marking location of the study area.

4.2. Data and Method

Our study uses legacy MCS data collected in late January and February of 2016 by the Crustal Reflectivity Experiment Southern Transect (CREST) expedition. Details about data acquisition and processing are described in Chapter 2 and by Wei et al. (2022). The MCS data imaged thermohaline fine structures along a ~1600 km east-west transect in the South Atlantic Subtropical Gyre, revealed mesoscale structures in the open ocean interior down to ~1400 m. This study focuses on the data that imaged the westernmost ~550 km of the transect where enhanced mixing induced by storm forced NIW was observed (Figure 4.1). The storm was documented on January 5, 2016, characterized by strong eastward wind stress (Figure 4.1C), and significant increase of strength within the near-inertial frequency band, suggesting the generation of NIW (Wei et al., 2022). The calculation of high-resolution diapycnal diffusivity maps from seismic data is described in detail by Fortin et al. (2016) and Wei et al. (2022), based on the assumption that seismic reflections are a good proxy for isopycnal surfaces (Holbrook et al., 2013). To extend our understanding of the observed storm-induced mixing, we corroborate the seismic images and high-resolution diffusivity maps with horizontal reflection velocities derived from pre-stack common mid-point (CMP) gathers.

Unlike the solid earth that is stationary during seismic acquisition, water is constantly moving in the ocean; the stacking of seismic traces smooths out water motion over a time period of ~30 minutes (Vsemirnova et al., 2009). Seismic reflections of water structures such as internal waves in the final image were laterally stretched or squeezed depending on how the water was moving with respect to the acquisition vessel. The

redundancy of the seismic acquisition system contains built-in time-space information about the water column; it is therefore possible to deduce spatial and temporal movements of reflections between NMO-corrected CMP gathers. Horizontal reflection velocities derived from seismic data have been used to study eddy transport (Gunn et al., 2018) and internal solitary waves (Tang et al., 2015).

Within a CMP gather, each trace from different shots are assumed to be reflected from the same location in the water column. Since shots points could be converted to time using the ship-log information, and CMP gathers represent changes in locations, for each time slice of 2 ms (~1.5 m) across multiple CMP gathers, reflection amplitudes can be plotted as a function of CMP number (distance) and shot point number (time). Horizontal velocities of reflections in the plane of seismic profile can be obtained by calculating their slopes in the CMP-shot point domain (Fig. 2). By calculating slope measurements across the seismic sections, we can obtain a horizontal velocity field map of imaged reflections. We did not calculate the velocity field for the first 200 m because our seismic acquisition system and processing strategy does not provide sufficient accuracy for shallow structures, as discussed in Chapter 2.
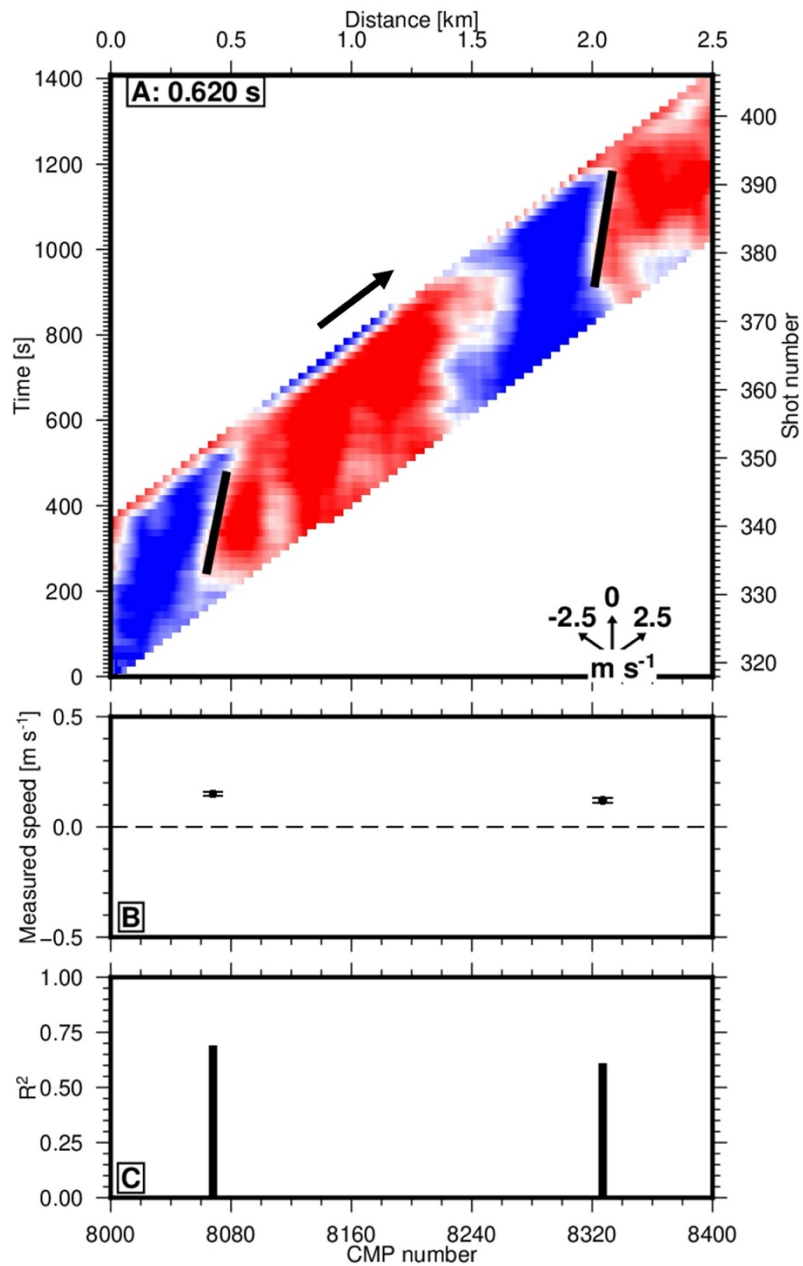
Figure 4.2: Example diagram showing horizontal reflection velocity estimation. (A) Reflection amplitudes of time slice 0.718 s plotted as function of distance (CMP number) and time (shot number). Red/blue = positive/negative amplitudes, respectively. Black arrow = speed of vessel (~2 m s^{-1}). Reflection velocities are identified by measured slopes that marked by tilting black bars, from left to right: 0.15 ± 0.01, 0.12 ± 0.01 m s^{-1}, as shown in (B). (C) Coefficient of determination, R^2, when fitting measured slopes.

4.3. Results

4.3.1. Tilted Reflections

At the eastern edge of the anticyclonic eddy (Figure 4.1A), the crossing of line05 with line1A and 1B offers a 3 dimensional (3D) visualization of thermohaline fine structures (Figure 4.3). It is worth noticing that the seismically imaged structures are presented 30 days after the formation of the eddy and storm forcing, showing structures resultant of the interaction between the storm generated NIW and the mesoscale eddy flows. Generally, reflections at the crossing of line05, 1A and 1B are discontinuous, the amplitudes are lower compared to locations of stronger stratification, such as the first 100 km of line1A (Figure 4.4A, B). Diapycnal mixing is also higher at this location as shown in Wei et al. (2022), which might be caused by breaking of internal waves that dissipates near-inertial energy. Along zonal direction, reflections that dip ~2-4° eastward occur ~120 km in line1A extend into line1B to ~100 km and occupies the water column from 200 m to 800 m (Figures 4.3A, B; 4.4B), largest dipping angle of ~4° is seen at shallower depth from 200 to 400 m, suggesting the tilted reflections are likely caused by a strong surface forcing, e.g., the eastward blowing storm (Figure 4.1C). In contrast, reflections along meridional direction are more horizontal (Figure 4.3C). In a 3D perspective, the interleaving eastward tilted reflections at the crossing forms a wedge shaped structure that remains horizontal in the meridional direction. The wedge shaped structure is unique in all seismic sections of the CREST survey (Wei et al., 2022), to better understand it, it is important to investigate the changes of relative movements of water masses across the edge of the eddy.
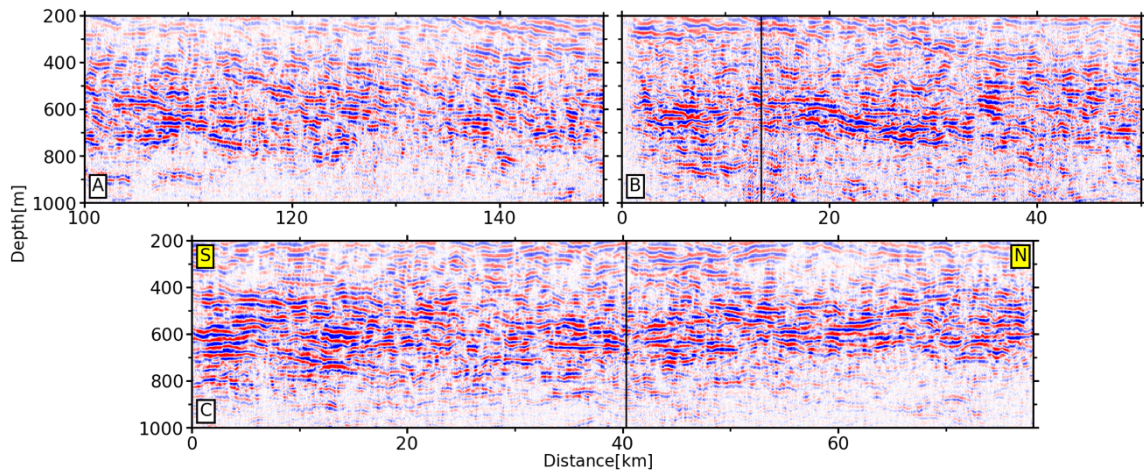
Figure 4.3: Intersection of seismic sections line1A, 1B and 05. (A) Seismic section of the last 50 km of line1A. (B) Seismic section of the first 50 km of line1B. (C) Seismic section of line05, the direction is labeled in upper corners as E (east) and N (north). Vertical black lines mark the location of the intersection. The location of the sections are marked by red crossings in Figure 4.1.

4.3.2. Horizontal Velocity Fields

We calculate horizontal velocities for all the reflections in line1A and 1B. The derived velocities were resampled on a 2 m by 10 m grid and smoothed, resulted in velocity fields in the plane of the seismic sections for both line1A and 1B (Figure 4.4B, E). We observe higher velocity of ~0.25-0.3 m s^{-1} in the upper region of both sections from 200 to 500 m, the direction of velocities in the plane of the seismic section is consistent with the direction of the acquisition vessel and the direction of winds in both early and late January, 2016 (Figure 4.1). Velocities of opposite direction that are lower in magnitude (~0.1 m s^{-1}) are observed mostly below 500 m and are located in line1A at range ~10-100 km, and in line1B at range ~120-190 km. Overall speaking, velocity fields

are mottled on mesoscale. We observe entrainments of patches of lower velocities within higher velocities in both sections. The mottled pattern starts to prevalent from the last 50 km of line1A, consistent with the location where reflections start to dip eastward (Figure 4.4A), and where diapycnal diffusivities start to increase (Figure 4.4C), implying ageostrophic processes that disturb the balance between the Coriolis force and the pressure gradients. Comparisons between seismic images, reflection velocity fields and high-resolution diapycnal diffusivity maps show a remarkable correlation: higher reflection amplitudes that represent stronger stratification are accompanied by lower reflection velocities and lower diffusivities ($\sim$1-3 $\times$ 10^{-5} m^2s^{-1}), while weaker and disrupted reflections that represent weaker stratification correspond to higher reflection velocities and higher diffusivities (5-50 $\times$ 10^{-5} m^2s^{-1}) (Figure 4.4).
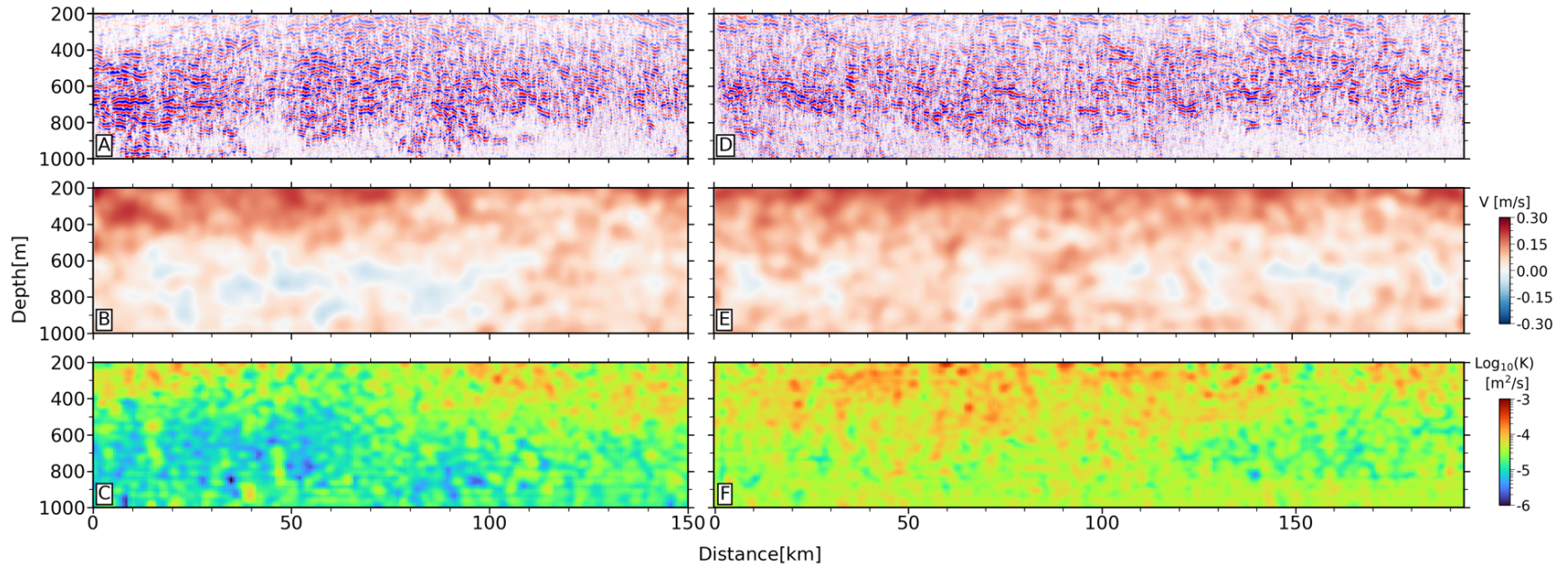
Figure 4.4: Seismic sections and the derived dynamical parameters. (A-C) Seismic section, horizontal reflection velocity field, high-resolution diapycnal diffusivity for line1A. (D-F) Same for line1B. Panel (C) and (F) are reprinted from Wei et al. (2022).

4.4. Discussion

4.4.1. Vertical Shear and Rotation

Following the hypothesis that enhanced mixing along the CREST transect away from topography is caused by dissipation of high-mode near-inertial energy (Wei et al., 2022), we explore the spatial correlation between tilted reflections, horizontal reflection velocities and diffusivities by estimating vertical shear in the water column, as high-mode near-inertial waves promote mixing because their potential for higher shear (Alford, 2003b, 2010). To understand the correlation, we calculate vertical shear of horizontal velocities in 200-1000 m depth range at four regions that have different mixing levels along the transect, the levels of enhanced mixing are calculated by Wei et al. (2022): (1) lowest diffusivity region in line1A at range 0-50 km (Figure 4.4A); (2) the intersection area of line1A, 1B and 05 where diffusivities start to increase, it is also the location of the edge of the eddy (Figure 4.4); (3) highest diffusivity region with the deepest penetration of enhanced mixing in line1B at range 50-100 km (Figure 4.4F); (4) higher diffusivity region with moderate penetration (~600 m) of enhanced mixing in line1C at range 50-100 km (Figure 4.7D). For each scenario, a vertical profile of reflection velocities is produced by horizontally averaged velocities within a time slice of 10 ms for a distance of 50 km. Vertical gradients are then calculated for each vertical profile to reflect the average shear for each region (Figure 4.5).

The average velocity profiles exhibit few differences, all of them are higher at the top and decrease with depth. The highest average horizontal velocity of 0.25 m s^{-1} is found at the crossing region of line1A, 1B and 05 at 200 m (Figure 4.5C), consistent with the

high surface geostrophic current velocity of the eddy (Figure 4.1A). The horizontal velocity is higher at almost all depths compare to other three regions away from the eddy, suggesting the eddy affects the entire water column down to 1000 m. The vertical shears of the average velocity profiles correlate well with the diffusivity levels in each region. The lowest diffusivity region in line1A has the lowest vertical shear (Figure 4.5B). In contrast, the highest diffusivity region in line1B has the highest vertical shear (Figure 4.5F); notably, vertical shear is higher at all depths in this region which might explain the deepest penetration of enhanced mixing. A similar phenomenon is also observed in the Arctic Ocean; Fer (2014) showed that the coherency is large between the dissipation rate, shear and strain in the near-inertial frequency band.

Overall, vertical shears are the lowest (0.011 s^{-1}) at the western end of the seismic transect and increase to a maximum (0.021 s^{-1}) in line1B in the vicinity of the eddy then decrease to a moderate level eastward (0.017 s^{-1}) (Figure 4.5). The zonal trend of vertical shear is consistent with the zonal distribution of diffusivities (Wei et al., 2022), and matches well with the changing of reflection shapes from horizontal to tilted, and horizontal again away from the eddy. We therefore suggest that enhanced mixing is mostly likely caused by the breaking of high-mode near-inertial waves through shear instability that forms tilted isopycnals, imaged as tilted reflections. The transition region of tilted reflections, highest shear, and highest mixing in the vicinity of the eddy highlights the role of eddy stirring along isopycnals (Abernathey et al., 2010) and the importance of mesoscale eddy in modifying near-inertial field (Elipot et al., 2010; Alford et al., 2016). It is worth noticing that the meridional reflections imaged in line05 are mostly horizontal,

implying the force exerted by the storm on the ocean surface have little variations in meridional direction, which is consistent with the eastward wind direction shown in Figure 4.1C.

The intersection of line1A, 1B and 05 at the edge of the eddy enables us to estimate horizontal current velocities on the east-north plane by treating in-plane velocities from zonal and meridional lines as east and north components, respectively. We use in-plane velocities within a 50×50 km window centered at the intersection of line1A, 1B and 05; velocities are vertically binned and averaged every 60 m. Results show a vertically rotating horizontal velocity field from 200 m to 500 m (Figure 4.6), with the highest velocity at the top and gradually decreasing with depth. The rotation of the velocity field is counterclockwise in the upper portion (200-350 m) and clockwise in the lower portion (350-500 m). Considering the NIW counterclockwise polarization in the Southern Hemisphere (Alford et al., 2016), we hypothesize that the observed rotation is likely the propagation of NIW superimposed on background eddy flows, and the eddy relative vorticity field may provide a pathway for NIW to propagate downward (Danioux et al., 2008).
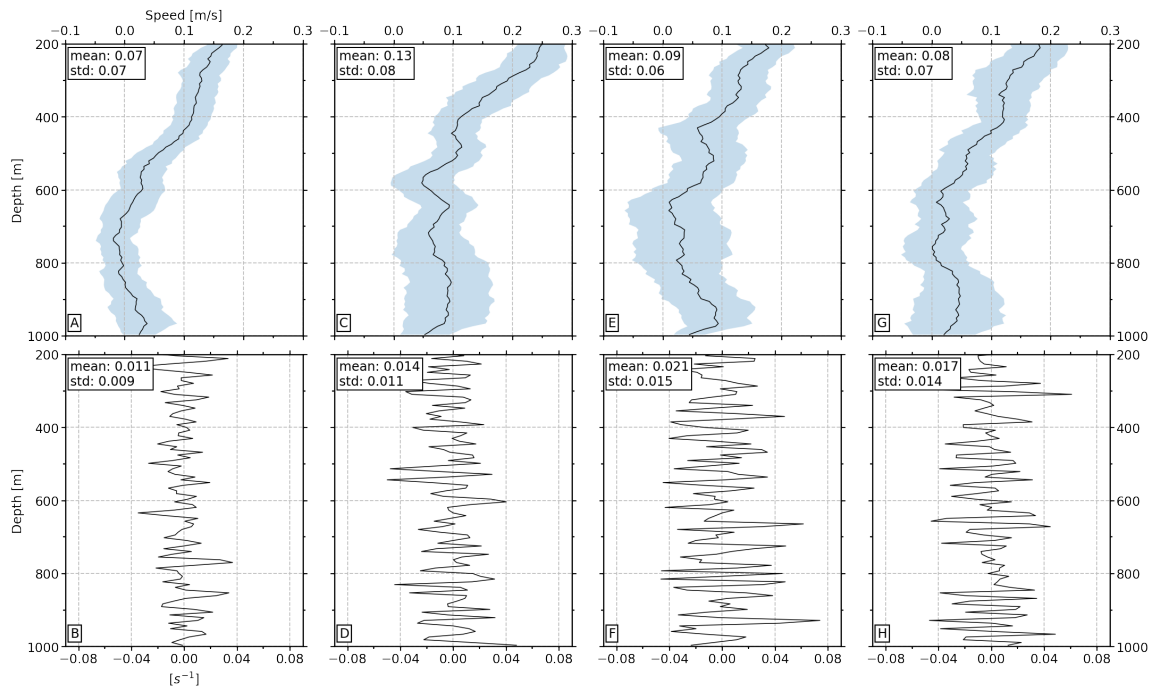
Figure 4.5: Vertical horizontal reflection velocity profiles smoothed by a 100 m moving window and their corresponding vertical shear for (A-B) low diffusivity region in line1A, (C-D) the crossing of line1A, 1B and 05, (E-F) high diffusivity region in line1B and (G-H) high diffusivity region in line1C, respectively. The vertical average and standard deviation for each profile and shear are annotated in the top left corner in each panel. Blue shades represent lateral standard deviation of horizontal reflection velocity for each time slice.
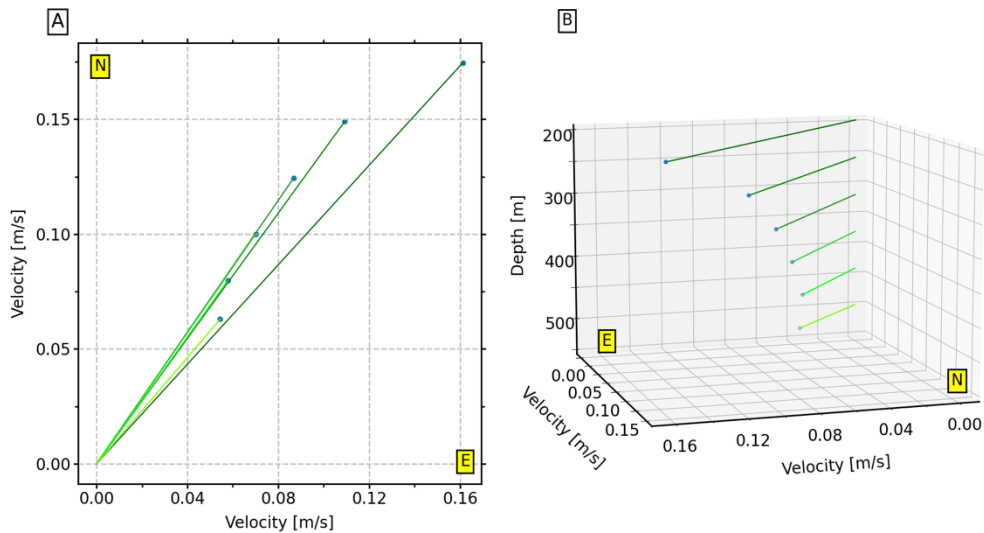
Figure 4.6: Horizontal current velocity estimated on the east-north plane at every 60 m plotted in (A) 2D and (B) 3D view. Green lines from dark to light represent decreasing velocities with depth. Directions of the axis are labeled as E (east) and N (north).

4.4.2. Deep Propagation of Near-Inertial Energy

Seismic image of line1B shows an isolated thermohaline boundary structure around depth 1000-1200 m at range 10-120 km, characterized by acoustically transparent zones above and below the structure (Figure 4.7A). A similarly isolated boundary structure is imaged in line1C at range 50-110 km (Figure 4.7C). As discussed in Chapter 2, with the support of legacy hydrographic data at the same sites, we hypothesized that the boundaries are likely fixed on decadal time scales and are probably generated by similar long-term stable processes such as the recirculation of intermediate water within the Subtropical Gyre (Boebel et al., 1997; Schmid et al., 2000). At the time of the seismic acquisition, the entire boundary in line1B is dipping to the east and is composed of tilted

reflections of ~2°; however, the boundary in line1C remains horizontal (Figure 4.7A, C). The shape and dipping nature of the boundary reflections in line1B resemble the reflections directly above them in depths 200-800 m, suggesting the dipping of the boundary in line1B could also be caused by shear instability.

Calculation of diapycnal diffusivity for both boundaries supports our idea of shear instability. Diffusivities of the boundary in line1B are as high as 4-8 $\times$ 10^{-5} m^{2}s^{-1} (Figure 4.7B), compared to 1-3 $\times$ 10^{-5} m^{2}s^{-1} around background level at the boundary in line1C (Figure 4.7D). Because of the weakness of reflections and strong random noise in the deeper parts of pre-stack CMP gathers, we cannot reliably extract horizontal reflection velocities from deeper reflections, which hinders our ability to estimate vertical shear at the boundaries. However, vertical shear above the boundary in line1B between 200-1000 m is higher than that above the boundary in line1C (Figure 4.5F, H), which might imply stronger shear in the deeper part of line1B. Nevertheless, based on the vertical shear analysis, we suggest that the reflection characteristic and enhanced mixing of the boundary in line1B is a good indicator for shear instability.
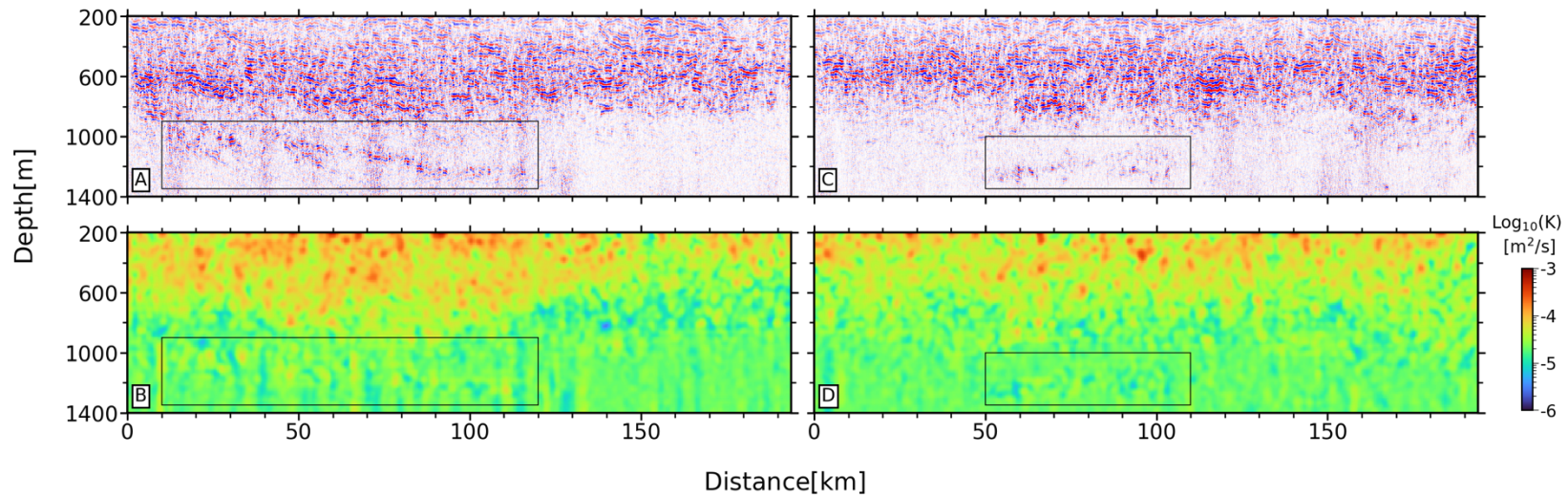
Figure 4.7: Seismic images and corresponding high-resolution diffusivity maps for line1B and 1C. (A-B) Seismic section and diffusivity map of line1B from 200 to 1400 m and . (C-D) Seismic section and diffusivity map of the first half of line1C from 200 to 1400 m (Figure 4.1). Black boxes mark the location of deep boundary structures.

The differences between the boundaries in line1B and 1C can be attributed to the influence of the mesoscale eddy field. Due to the presence of the eddy at the west of line1B, enhanced mixing several factors higher than the background level penetrates as deep as 1200 m, suggesting deep propagation of near-inertial energy much deeper than previously thought (Wei et al., 2022). In contrast, the deepest penetration of enhanced mixing in line1C is limited to 600-800 m. Our observations at deep water boundaries highlight the role of eddy in draining energy into the ocean interior, consistent with previous large scale observations (Jing et al., 2011; Whalen et al., 2018) and numerical models (Zhai et al., 2007; Danioux et al., 2008).

4.5. Conclusion

This study uses legacy multichannel seismic data to investigate enhanced mixing caused by storm generated high-mode near-inertial waves in the central South Atlantic. We image the thermohaline fine structures down to 1400 m and extract high-resolution dynamical parameters such as horizontal velocity and diapycnal diffusivity from seismic images. We observe strong coherency between reflection shapes, horizontal velocity and diapycnal diffusivity which could be explained by the degree of vertical shear in the water column: higher vertical shear leads to tilted isopycnal surfaces that are weaker in stratification and eventually resulted in higher diffusivities. We conclude that the local dissipation of high-mode near-inertial energy is the most likely candidate for the observed enhanced mixing. The tilted reflections, highest vertical shear and diffusivities in the vicinity of the eddy suggests the important role of the mesoscale eddy in dissipating near-inertial energy. In addition, comparison of reflection shapes and diapycnal diffusivities

between two deep boundary structures of similar origin provides evidence of deep penetration of near-inertial energy to 1200 m in the vicinity of the eddy, suggesting the mesoscale eddy field provides pathways for deep propagation of near-inertial energy. In summary, this study extends the observation record of high-mode NIW and their interaction with mesoscale eddies by using seismic oceanography, demonstrating the spatial sampling advantage of seismic oceanography in mapping oceanic dynamical processes, contributing to the understanding of diapycnal mixing in the South Atlantic.

5. SUMMARY

This dissertation advances our understanding of open ocean processes by providing the first fine scale observation of the South Atlantic interior at an important transect of the Atlantic meridional overturning circulation using legacy multichannel seismic data.

In Chapter 2 we develop an adapted seismic processing strategy for legacy multichannel seismic data to better image the thermohaline fine structures of the water column that have much weaker reflectivity compared to the solid earth. We use this strategy to image the water column of the central South Atlantic down to ~1600 m. The resulting seismic images reveal the prevalence of mesoscale processes in the ocean interior mostly caused by double diffusion and thermohaline intrusion. We also observe two structures with unknown origin that are currently unaware to the scientific community.

In Chapter 3 we calculate the first high-resolution turbulent mixing map of the central South Atlantic thermocline. The results show that turbulent mixing in the South Atlantic thermocline is heterogeneous, with enhanced mixing exceeding the background value by more than a magnitude above different topographic settings. With the support of bathymetry, Argo data, wind stress and satellite data, we conclude that the enhanced mixing above the Mid-Atlantic Ridge is caused by the rough topography and hypothesize that storm enhances mixing away from the Mid-Atlantic Ridge. We compare the down-sampled results with mixing values calculated from discreate legacy hydrographic measurements and find minor changes of turbulent mixing on decadal time scales.

In Chapter 4 we focus on seismically-imaged tilted isopycnal surfaces in the vicinity of an anticyclonic eddy. Around this region, we explore the hypothesis of storm enhances mixing made in Chapter 3. We estimate current velocity fields from the seismic data and calculate vertical shear for locations with different levels of mixing. Results show that enhanced mixing is primarily driven by wind induced instabilities of sheared flow. Close to the eddy, shear enhances mixing in the deeper water column (~1200 m), which supports the interpretation of the eddy promoting deep propagation of wind injected energy.

REFERENCES

Abernathey, R., Marshall, J., Mazloff, M., & Shuckburgh, E. (2010). Enhancement of mesoscale eddy stirring at steering levels in the Southern Ocean. *Journal of Physical Oceanography, 40*(1), 170-184.

Alford, M. H. (2003a). Improved global maps and 54‑year history of wind‑work on ocean inertial motions. *Geophysical Research Letters, 30*(8).

Alford, M. H. (2003b). Redistribution of energy available for ocean mixing by long-range propagation of internal waves. *Nature, 423*(6936), 159-162.

Alford, M. H. (2010). Sustained, full-water-column observations of internal waves and mixing near Mendocino Escarpment. *Journal of Physical Oceanography, 40*(12), 2643-2660.

Alford, M. H., Cronin, M. F., & Klymak, J. M. (2012). Annual cycle and depth penetration of wind-generated near-inertial internal waves at Ocean Station Papa in the northeast Pacific. *Journal of Physical Oceanography, 42*(6), 889-909.

Alford, M. H., & Gregg, M. C. (2001). Near‑inertial mixing: Modulation of shear, strain and microstructure at low latitude. *Journal of Geophysical Research: Oceans, 106*(C8), 16947-16968.

Alford, M. H., MacKinnon, J. A., Simmons, H. L., & Nash, J. D. (2016). Near-inertial internal gravity waves in the ocean. *Annual review of marine science, 8*, 95-123.

Alford, M. H., & Whitmont, M. (2007). Seasonal and spatial variability of near-inertial kinetic energy from historical moored velocity records. *Journal of Physical Oceanography, 37*(8), 2022-2037.

Biescas, B., Sallarès, V., Pelegrí, J. L., Machín, F., Carbonell, R., Buffett, G., . . . Calahorrano, A. (2008). Imaging meddy finestructure using multichannel seismic reflection data. *Geophysical Research Letters, 35*(11).

Boebel, O., Schmid, C., & Zenk, W. (1997). Flow and recirculation of Antarctic intermediate water across the Rio Grande rise. *Journal of Geophysical Research: Oceans, 102*(C9), 20967-20986.

Bray, N. A., & Fofonoff, N. (1981). Available potential energy for MODE eddies. *Journal of Physical Oceanography, 11*(1), 30-47.

Broecker, W. S. (1991). The great ocean conveyor. *Oceanography, 4*(2), 79-89.

Buffett, G. G., Krahmann, G., Klaeschen, D., Schroeder, K., Sallares, V., Papenberg, C., . . . Zitellini, N. (2017). Seismic oceanography in the Tyrrhenian Sea: Thermohaline staircases, eddies, and internal waves. *Journal of Geophysical Research: Oceans, 122*(11), 8503-8523.

Cabré, A., Pelegrí, J., & Vallès‐Casanova, I. (2019). Subtropical‐tropical transfer in the South Atlantic Ocean. *Journal of Geophysical Research: Oceans, 124*(7), 4820-4837.

Chaigneau, A., Pizarro, O., & Rojas, W. (2008). Global climatology of near‐inertial current characteristics from Lagrangian observations. *Geophysical Research Letters, 35*(13).

Chelton, D. B., Schlax, M. G., Samelson, R. M., & de Szoeke, R. A. (2007). Global observations of large oceanic eddies. *Geophysical Research Letters, 34*(15).

D'Asaro, E. A. (1985). The energy flux from the wind to near-inertial motions in the surface mixed layer. *Journal of Physical Oceanography, 15*(8), 1043-1059.

D'Asaro, E. A., Eriksen, C. C., Levine, M. D., Niiler, P., & Van Meurs, P. (1995). Upper-ocean inertial currents forced by a strong storm. Part I: Data and comparisons with linear theory. *Journal of Physical Oceanography, 25*(11), 2909-2936.

Danioux, E., Klein, P., & Rivière, P. (2008). Propagation of wind energy into the deep ocean through a fully turbulent mesoscale eddy field. *Journal of Physical Oceanography, 38*(10), 2224-2241.

Della Penna, A., & Gaube, P. (2019). Overview of (sub) mesoscale ocean dynamics for the NAAMES field program. *Frontiers in Marine Science, 6*, 384.

Dickinson, A., White, N., & Caulfield, C. (2017). Spatial variation of diapycnal diffusivity estimated from seismic imaging of internal wave field, Gulf of Mexico. *Journal of Geophysical Research: Oceans, 122*(12), 9827-9854.

Dickinson, A., White, N., & Caulfield, C. (2020). Time‐Lapse Acoustic Imaging of Mesoscale and Fine‐Scale Variability within the Faroe‐Shetland Channel. *Journal of Geophysical Research: Oceans, 125*(8), e2019JC015861.

Dohan, K., & Davis, R. E. (2011). Mixing in the transition layer during two storm events. *Journal of Physical Oceanography, 41*(1), 42-66.

Dong, S., Baringer, M. O., Goni, G. J., Meinen, C. S., & Garzoli, S. L. (2014). Seasonal variations in the South Atlantic Meridional Overturning Circulation from observations and numerical models. *Geophysical Research Letters, 41*(13), 4611-4618.

Dong, S., Goni, G., & Bringas, F. (2015). Temporal variability of the South Atlantic meridional overturning circulation between 20 S and 35 S. *Geophysical Research Letters, 42*(18), 7655-7662.

Elipot, S., Lumpkin, R., & Prieto, G. (2010). Modification of inertial oscillations by the mesoscale eddy field. *Journal of Geophysical Research: Oceans, 115*(C9).

Estep, J., Reece, R., Kardell, D. A., Christeson, G. L., & Carlson, R. L. (2019). Seismic Layer 2A: Evolution and Thickness From 0‐to 70‐Ma Crust in the Slow‐Intermediate Spreading South Atlantic. *Journal of Geophysical Research: Solid Earth, 124*(8), 7633-7651.

Fer, I. (2014). Near-inertial mixing in the central Arctic Ocean. *Journal of Physical Oceanography, 44*(8), 2031-2049.

Fofonoff, N. P., & Millard Jr, R. (1983). Algorithms for the computation of fundamental properties of seawater.

Fortin, W. F., & Holbrook, W. S. (2009). Sound speed requirements for optimal imaging of seismic oceanography data. *Geophysical Research Letters, 36*(24).

Fortin, W. F., Holbrook, W. S., & Schmitt, R. W. (2016). Mapping turbulent diffusivity associated with oceanic internal lee waves offshore Costa Rica. *Ocean Science, 12*(2), 601-612.

Fortin, W. F., Holbrook, W. S., & Schmitt, R. W. (2017). Seismic estimates of turbulent diffusivity and evidence of nonlinear internal wave forcing by geometric resonance in the South China Sea. *Journal of Geophysical Research: Oceans, 122*(10), 8063-8078.

Fox-Kemper, B., Adcroft, A., Böning, C. W., Chassignet, E. P., Curchitser, E., Danabasoglu, G., . . . Greatbatch, R. J. (2019). Challenges and prospects in ocean circulation models. *Frontiers in Marine Science, 6*, 65.

Garrett, C. (2001). What is the "near-inertial" band and why is it different from the rest of the internal wave spectrum? *Journal of Physical Oceanography, 31*(4), 962-971.

Garrett, C., & Kunze, E. (2007). Internal tide generation in the deep ocean. *Annu. Rev. Fluid Mech., 39*, 57-87.

Garrett, C., & Munk, W. (1975). Space‐time scales of internal waves: A progress report. *Journal of Geophysical Research, 80*(3), 291-297.

Garzoli, S. L. (1993). Geostrophic velocity and transport variability in the Brazil-Malvinas Confluence. *Deep Sea Research Part I: Oceanographic Research Papers, 40*(7), 1379-1403.

Garzoli, S. L., Baringer, M. O., Dong, S., Perez, R. C., & Yao, Q. (2013). South Atlantic meridional fluxes. *Deep Sea Research Part I: Oceanographic Research Papers, 71*, 21-32.

Garzoli, S. L., Dong, S., Fine, R., Meinen, C. S., Perez, R. C., Schmid, C., . . . Yao, Q. (2015). The fate of the deep western boundary current in the South Atlantic. *Deep Sea Research Part I: Oceanographic Research Papers, 103*, 125-136.

Garzoli, S. L., & Matano, R. (2011). The South Atlantic and the Atlantic meridional overturning circulation. *Deep Sea Research Part II: Topical Studies in Oceanography, 58*(17), 1837-1847.

Gill, A. (1984). On the behavior of internal waves in the wakes of storms. *Journal of Physical Oceanography, 14*(7), 1129-1151.

Gregg, M. C., Sanford, T. B., & Winkel, D. P. (2003). Reduced mixing from the breaking of internal waves in equatorial waters. *Nature, 422*(6931), 513-515.

Gunn, K. L., Dickinson, A., White, N., & Caulfield, C.-C. P. (2021). Vertical Mixing and Heat Fluxes Conditioned by a Seismically Imaged Oceanic Front. *Frontiers in Marine Science, 8*, 697179.

Gunn, K. L., White, N., & Caulfield, C. c. P. (2020). Time‐Lapse Seismic Imaging of Oceanic Fronts and Transient Lenses Within South Atlantic Ocean. *Journal of Geophysical Research: Oceans, 125*(7), e2020JC016293.

Gunn, K. L., White, N. J., Larter, R. D., & Caulfield, C.-c. P. (2018). Calibrated Seismic Imaging of Eddy‐Dominated Warm‐Water Transport Across the Bellingshausen Sea, Southern Ocean. *Journal of Geophysical Research: Oceans, 123*(4), 3072-3099.

Harrison, M., & Hallberg, R. (2008). Pacific subtropical cell response to reduced equatorial dissipation. *Journal of Physical Oceanography, 38*(9), 1894-1912.

Hernández-Guerra, A., Talley, L. D., Pelegrí, J. L., Vélez-Belchí, P., Baringer, M. O., Macdonald, A. M., & McDonagh, E. L. (2019). The upper, deep, abyssal and overturning circulation in the Atlantic Ocean at 30° S in 2003 and 2011. *Progress in oceanography, 176*, 102136.

Hieronymus, M., Nycander, J., Nilsson, J., Döös, K., & Hallberg, R. (2019). Oceanic overturning and heat transport: The role of background diffusivity. *Journal of Climate, 32*(3), 701-716.

Hobbs, R. W., Klaeschen, D., Sallarès, V., Vsemirnova, E., & Papenberg, C. (2009). Effect of seismic source bandwidth on reflection sections to image water structure. *Geophysical Research Letters, 36*(24).

Holbrook, W. S., & Fer, I. (2005). Ocean internal wave spectra inferred from seismic reflection transects. *Geophysical Research Letters, 32*(15).

Holbrook, W. S., Fer, I., Schmitt, R. W., Lizarralde, D., Klymak, J. M., Helfrich, L. C., & Kubichek, R. (2013). Estimating oceanic turbulence dissipation from seismic images. *Journal of Atmospheric and Oceanic Technology, 30*(8), 1767-1788.

Holbrook, W. S., Páramo, P., Pearse, S., & Schmitt, R. W. (2003). Thermohaline fine structure in an oceanographic front from seismic reflection profiling. *Science, 301*(5634), 821-824.

Jing, Z., Chang, P., DiMarco, S. F., & Wu, L. (2015). Role of near-inertial internal waves in subthermocline diapycnal mixing in the northern Gulf of Mexico. *Journal of Physical Oceanography, 45*(12), 3137-3154.

Jing, Z., & Wu, L. (2010). Seasonal variation of turbulent diapycnal mixing in the northwestern Pacific stirred by wind stress. *Geophysical Research Letters, 37*(23).

Jing, Z., Wu, L., Li, L., Liu, C., Liang, X., Chen, Z., . . . Liu, Q. (2011). Turbulent diapycnal mixing in the subtropical northwestern Pacific: Spatial‐seasonal variations and role of eddies. *Journal of Geophysical Research: Oceans, 116*(C10).

Jun, H., Jou, H.-T., Kim, C.-H., Lee, S. H., & Kim, H.-J. (2020). Random noise attenuation of sparker seismic oceanography data with machine learning. *Ocean Science, 16*(6), 1367-1383.

Kanamitsu, M., Ebisuzaki, W., Woollen, J., Yang, S.-K., Hnilo, J., Fiorino, M., & Potter, G. (2002). Ncep–doe amip-ii reanalysis (r-2). *Bulletin of the American Meteorological Society, 83*(11), 1631-1644.

Kersalé, M., Perez, R. C., Speich, S., Meinen, C. S., Lamont, T., Le Hénaff, M., . . . Dong, S. (2019). Shallow and Deep Eastern Boundary Currents in the South Atlantic at 34.5° S: Mean Structure and Variability. *Journal of Geophysical Research: Oceans, 124*(3), 1634-1659.

Klymak, J. M., & Moum, J. N. (2007). Oceanic isopycnal slope spectra. Part II: Turbulence. *Journal of Physical Oceanography, 37*(5), 1232-1245.

Klymak, J. M., Moum, J. N., Nash, J. D., Kunze, E., Girton, J. B., Carter, G. S., . . . Gregg, M. C. (2006). An estimate of tidal energy lost to turbulence at the Hawaiian Ridge. *Journal of Physical Oceanography, 36*(6), 1148-1164.

Krahmann, G., Papenberg, C., Brandt, P., & Vogt, M. (2009). Evaluation of seismic reflector slopes with a Yoyo‐CTD. *Geophysical Research Letters, 36*(24).

Kunze, E., Firing, E., Hummon, J. M., Chereskin, T. K., & Thurnherr, A. M. (2006). Global abyssal mixing inferred from lowered ADCP shear and CTD strain profiles. *Journal of Physical Oceanography, 36*(8), 1553-1576.

Kunze, E., & Toole, J. M. (1997). Tidally driven vorticity, diurnal shear, and turbulence atop Fieberling Seamount. *Journal of Physical Oceanography, 27*(12), 2663-2693.

Large, W., & Pond, S. (1981). Open ocean momentum flux measurements in moderate to strong winds. *Journal of Physical Oceanography, 11*(3), 324-336.

Ledwell, J., Montgomery, E., Polzin, K., Laurent, L. S., Schmitt, R., & Toole, J. (2000). Evidence for enhanced mixing over rough topography in the abyssal ocean. *Nature, 403*(6766), 179.

Li, Y., & Xu, Y. (2014). Penetration depth of diapycnal mixing generated by wind stress and flow over topography in the northwestern P acific. *Journal of Geophysical Research: Oceans, 119*(8), 5501-5514.

Lumpkin, R., & Speer, K. (2007). Global ocean meridional overturning. *Journal of Physical Oceanography, 37*(10), 2550-2562.

MacKinnon, J., St Laurent, L., & Garabato, A. C. N. (2013). Diapycnal mixing processes in the ocean interior. In *International Geophysics* (Vol. 103, pp. 159-183): Elsevier.

MacKinnon, J., & Winters, K. (2005). Subtropical catastrophe: Significant loss of low‐mode tidal energy at 28.9°. *Geophysical Research Letters, 32*(15).

Martin, G. S., Wiley, R., & Marfurt, K. J. (2006). Marmousi2: An elastic upgrade for Marmousi. *The leading edge, 25*(2), 156-166.

Mauritzen, C., Polzin, K., McCartney, M., Millard, R., & West‐Mack, D. (2002). Evidence in hydrography and density fine structure for enhanced vertical mixing over the Mid‐Atlantic Ridge in the western Atlantic. *Journal of Geophysical Research: Oceans, 107*(C10), 11-11-11-19.

Melet, A., Hallberg, R., Legg, S., & Polzin, K. (2013). Sensitivity of the ocean state to the vertical distribution of internal-tide-driven mixing. *Journal of Physical Oceanography, 43*(3), 602-615.

Melet, A., Legg, S., & Hallberg, R. (2016). Climatic impacts of parameterized local and remote tidal mixing. *Journal of Climate, 29*(10), 3473-3500.

Mojica, J. F., Sallarès, V., & Biescas, B. (2018). High-resolution diapycnal mixing map of the Alboran Sea thermocline from seismic reflection images. *Ocean Science, 14*(3), 403-415.

Munk, W., & Wunsch, C. (1998). Abyssal recipes II: Energetics of tidal and wind mixing. *Deep Sea Research Part I: Oceanographic Research Papers, 45*(12), 1977-2010.

Munk, W. H. (1966). *Abyssal recipes.* Paper presented at the Deep Sea Research and Oceanographic Abstracts.

Nandi, P., Holbrook, W. S., Pearse, S., Páramo, P., & Schmitt, R. W. (2004). Seismic reflection imaging of water mass boundaries in the Norwegian Sea. *Geophysical Research Letters, 31*(23).

Olson, D. B., Podestá, G. P., Evans, R. H., & Brown, O. B. (1988). Temporal variations in the separation of Brazil and Malvinas Currents. *Deep Sea Research Part A. Oceanographic Research Papers, 35*(12), 1971-1990.

Osborn, T. (1980). Estimates of the local rate of vertical diffusion from dissipation measurements. *Journal of Physical Oceanography, 10*(1), 83-89.

Osborn, T. R., & Cox, C. S. (1972). Oceanic fine structure. *Geophysical Fluid Dynamics, 3*(4), 321-345.

Piété, H., Marié, L., Marsset, B., Thomas, Y., & Gutscher, M. A. (2013). Seismic reflection imaging of shallow oceanographic structures. *Journal of Geophysical Research: Oceans, 118*(5), 2329-2344.

Plueddemann, A., & Farrar, J. (2006). Observations and models of the energy flux from the wind to mixed-layer inertial currents. *Deep Sea Research Part II: Topical Studies in Oceanography, 53*(1-2), 5-30.

Pollard, R. T. (1970). *On the generation by winds of inertial waves in the ocean.* Paper presented at the Deep Sea Research and Oceanographic Abstracts.

Polzin, K., Toole, J., Ledwell, J., & Schmitt, R. (1997). Spatial variability of turbulent mixing in the abyssal ocean. *Science, 276*(5309), 93-96.

Price, J. F., Weller, R. A., & Pinkel, R. (1986). Diurnal cycling: Observations and models of the upper ocean response to diurnal heating, cooling, and wind mixing. *Journal of Geophysical Research: Oceans, 91*(C7), 8411-8427.

Roemmich, D., Alford, M. H., Claustre, H., Johnson, K., King, B., Moum, J., . . . Purkey, S. (2019). On the future of Argo: A global, full-depth, multi-disciplinary array. *Frontiers in Marine Science, 6*, 439.

Ruddick, B. (2018). Seismic Oceanography's Failure to Flourish: A Possible Solution. *Journal of Geophysical Research: Oceans, 123*(1), 4-7.

Ruddick, B., & Gargett, A. E. (2003). Oceanic double-infusion: Introduction. *Progress in oceanography, 56*(3-4), 381-393.

Ruddick, B., & Richards, K. (2003). Oceanic thermohaline intrusions: observations. *Progress in oceanography, 56*(3-4), 499-527.

Ruddick, B., SoNg, H., Dong, C., & Pinheiro, L. (2009). Water column seismic images as maps of temperature gradient. *Oceanography, 22*(1), 192-205.

Ryan, W. B., Carbotte, S. M., Coplan, J. O., O'Hara, S., Melkonian, A., Arko, R., . . . Nitsche, F. (2009). Global multi‐resolution topography synthesis. *Geochemistry, Geophysics, Geosystems, 10*(3).

Sallarès, V., Biescas, B., Buffett, G., Carbonell, R., Dañobeitia, J. J., & Pelegrí, J. L. (2009). Relative contribution of temperature and salinity to ocean acoustic reflectivity. *Geophysical Research Letters, 36*(24).

Schmid, C. (2014). Mean vertical and horizontal structure of the subtropical circulation in the South Atlantic from three-dimensional observed velocity fields. *Deep Sea Research Part I: Oceanographic Research Papers, 91*, 50-71.

Schmid, C., Siedler, G., & Zenk, W. (2000). Dynamics of intermediate water circulation in the subtropical South Atlantic. *Journal of Physical Oceanography, 30*(12), 3191-3211.

Schmitz Jr, W. J. (1995). On the interbasin‐scale thermohaline circulation. *Reviews of Geophysics, 33*(2), 151-173.

Sheen, K., White, N., Caulfield, C., & Hobbs, R. (2012). Seismic imaging of a large horizontal vortex at abyssal depths beneath the Sub-Antarctic Front. *Nature Geoscience, 5*(8), 542.

Sheen, K., White, N., & Hobbs, R. (2009). Estimating mixing rates from seismic images of oceanic structure. *Geophysical Research Letters, 36*(24).

105

Sheen, K. L., White, N., Caulfield, C. P., & Hobbs, R. W. (2011). Estimating geostrophic shear from seismic images of oceanic structure. *Journal of Atmospheric and Oceanic Technology, 28*(9), 1149-1154.

Sheriff, R. E., & Geldart, L. P. (1995). *Exploration seismology*: Cambridge university press.

Simmons, H. L. (2008). Spectral modification and geographic redistribution of the semi-diurnal internal tide. *Ocean Modelling, 21*(3-4), 126-138.

Sloyan, B. M. (2005). Spatial variability of mixing in the Southern Ocean. *Geophysical Research Letters, 32*(18).

Sloyan, B. M., Wanninkhof, R., Kramp, M., Johnson, G. C., Talley, L. D., Tanhua, T., . . . McGovern, E. (2019). The global ocean ship-based hydrographic investigations program (GO-SHIP): a platform for integrated multidisciplinary ocean science. *Frontiers in Marine Science, 6*, 445.

St Laurent, L. C., & Thurnherr, A. M. (2007). Intense mixing of lower thermocline water on the crest of the Mid-Atlantic Ridge. *Nature, 448*(7154), 680.

St. Laurent, L. C., Toole, J. M., & Schmitt, R. W. (2001). Buoyancy forcing by turbulence above rough topography in the abyssal Brazil Basin. *Journal of Physical Oceanography, 31*(12), 3476-3495.

Stramma, L., & England, M. (1999). On the water masses and mean circulation of the South Atlantic Ocean. *Journal of Geophysical Research: Oceans, 104*(C9), 20863-20883.

Talley, L. D. (2011). *Descriptive physical oceanography: an introduction*: Academic press.

Talley, L. D., Feely, R. A., Sloyan, B. M., Wanninkhof, R., Baringer, M. O., Bullister, J. L., . . . Firing, E. (2016). Changes in ocean heat, carbon content, and ventilation: A review of the first decade of GO-SHIP global repeat hydrography. *Annual review of marine science, 8*, 185-215.

Tang, Q., Gulick, S. P., Sun, J., Sun, L., & Jing, Z. (2020). Submesoscale features and turbulent mixing of an oblique anticyclonic eddy in the Gulf of Alaska investigated by marine seismic survey data. *Journal of Geophysical Research: Oceans, 125*(1), e2019JC015393.

Tang, Q., Hobbs, R., Wang, D., Sun, L., Zheng, C., Li, J., & Dong, C. (2015). Marine seismic observation of internal solitary wave packets in the northeast S outh C hina S ea. *Journal of Geophysical Research: Oceans, 120*(12), 8487-8503.

Tang, Q., Hobbs, R., Zheng, C., Biescas, B., & Caiado, C. (2016). Markov Chain Monte Carlo inversion of temperature and salinity structure of an internal solitary wave packet from marine seismic data. *Journal of Geophysical Research: Oceans, 121*(6), 3692-3709.

Tang, Q., Jing, Z., Lin, J., & Sun, J. (2021). Diapycnal Mixing in the Subthermocline of the Mariana Ridge from High-Resolution Seismic Images. *Journal of Physical Oceanography, 51*(4), 1283-1300.

Tang, Q., Xu, M., Zheng, C., Xu, X., & Xu, J. (2018). A Locally Generated High‐Mode Nonlinear Internal Wave Detected on the Shelf of the Northern South China Sea From Marine Seismic Observations. *Journal of Geophysical Research: Oceans, 123*(2), 1142-1155.

Valla, D., Piola, A. R., Meinen, C. S., & Campos, E. (2018). Strong mixing and recirculation in the northwestern Argentine Basin. *Journal of Geophysical Research: Oceans, 123*(7), 4624-4648.

Vsemirnova, E., Hobbs, R., Serra, N., Klaeschen, D., & Quentel, E. (2009). Estimating internal wave spectra using constrained models of the dynamic ocean. *Geophysical Research Letters, 36*(24).

Walsh, K. J., Camargo, S. J., Knutson, T. R., Kossin, J., Lee, T.-C., Murakami, H., & Patricola, C. (2019). Tropical cyclones and climate change. *Tropical Cyclone Research and Review, 8*(4), 240-250.

Waterhouse, A. F., MacKinnon, J. A., Nash, J. D., Alford, M. H., Kunze, E., Simmons, H. L., . . . Pinkel, R. (2014). Global patterns of diapycnal mixing from measurements of the turbulent dissipation rate. *Journal of Physical Oceanography, 44*(7), 1854-1872.

Wei, J., Gunn, K. L., & Reece, R. (2022). Mid-Ocean Ridge and Storm Enhanced Mixing in the Central South Atlantic Thermocline. *Frontiers in Marine Science, 8*, 771973.

Whalen, C., Talley, L., & MacKinnon, J. (2012). Spatial and temporal variability of global ocean mixing inferred from Argo profiles. *Geophysical Research Letters, 39*(18).

Whalen, C. B., MacKinnon, J. A., & Talley, L. D. (2018). Large-scale impacts of the mesoscale environment on mixing from wind-driven internal waves. *Nature Geoscience, 11*(11), 842-847.

Wunsch, C., & Ferrari, R. (2004). Vertical mixing, energy, and the general circulation of the oceans. *Annu. Rev. Fluid Mech., 36*, 281-314.

Yilmaz, Ö. (2001). *Seismic data analysis: Processing, inversion, and interpretation of seismic data*: Society of exploration geophysicists.

Young, W., & Jelloul, M. B. (1997). Propagation of near-inertial oscillations through a geostrophic flow. *Journal of Marine Research, 55*(4), 735-766.

Zhai, X., Greatbatch, R. J., & Eden, C. (2007). Spreading of near‐inertial energy in a 1/12° model of the North Atlantic Ocean. *Geophysical Research Letters, 34*(10).

Zhai, X., Greatbatch, R. J., & Zhao, J. (2005). Enhanced vertical propagation of storm‐induced near‐inertial energy in an eddying ocean channel model. *Geophysical Research Letters, 32*(18).

Zhang, K., Zuo, W., Chen, Y., Meng, D., & Zhang, L. (2017). Beyond a gaussian denoiser: Residual learning of deep cnn for image denoising. *IEEE Transactions on Image Processing, 26*(7), 3142-3155.